Design, Synthesis and Investigation of in vitro Therapeutic Effects of Silicon-Substituted Xanthene Based Phototheranostic Agents

by

Sultan Çetin

A Dissertation Submitted to the

Graduate School of Sciences and Engineering

in Partial Fulfillment of the Requirements for

the Degree of

Master of Science

in

Chemistry

KOÇ
ÜNİVERSİTESİ

July 7, 2021

Design, Synthesis and Investigation of in vitro Therapeutic Effects of Silicon-Substituted Xanthene Based Phototheranostic Agents

Koç University

Graduate School of Sciences and Engineering

This is to certify that I have examined this copy of a master's thesis by

Sultan Çetin

and have found that it is complete and satisfactory in all respects,
and that any and all revisions required by the final
examining committee have been made.

Committee Members:

Asst. Prof. Dr. Safacan Kölemen (Advisor)

Prof. Funda Acar Yağcı

Assoc. Prof. Görkem Günbaş

Date: 07.07.2021

To my lovely family

ABSTRACT

Design, Synthesis and Investigation of in vitro Therapeutic Effects of Silicon-Substituted Xanthene Based Phototheranostic Agents

Sultan Çetin

Master of Science in Chemistry

July 7, 2021

Cancer remains to be major public health problem and leading cause of mortality worldwide despite extensive efforts to develop effective cancer therapeutic methods. Tumor heterogeneity, metastasis and therapy resistance are among the major problems limiting therapeutic efficacy. The combination of therapeutic action with diagnostic imaging known as theranostic action is a developing modality to address these challenges. So far photodynamic therapy (PDT) has been accepted as highly promising methods as it offers non-invasive treatment, low systemic toxicity, negligible drug resistance and immune system activation against the tumor. PDT involves the generation of cytotoxic reactive oxygen species (ROS) through the interaction of a photosensitizer (PS), light and molecular oxygen ($^3O_2$). However, there are some obstacles of PDT including limited penetration depth of incident light through tissues hindering the widespread application in clinical studies. Therefore, the development of PSs to address current challenges is in great importance. Herein, this thesis put emphasis on development of new phototheranostic agents with improved properties.

In the first part, **SF-I**, iodinated derivative of silicon fluorescein **(SF)**, was introduced as the first example of **SF** based PDT agent, which holds great promise as a small molecule-based theranostic agent. Photophysical properties and singlet oxygen generation of **SF-I** in aqueous solutions was evaluated and found to be promising in phototheranostic applications with red shifted absorption and high singlet oxygen quantum yield up to 45%. Cytotoxicity and fluorescent imaging potential of **SF-I** *in vitro* was evaluated in two different (MDA MB-231, HCT-116) cancer cell lines. Novel designs based on **SF-I** to increase selectivity towards cancer cells are easy to apply by substitution through phenolic groups in the structure.

In the second part, our aim was to design an activatable phototheranostic agent. In this direction, another silicon-xanthene core Tokyo Magenta **(TM)** was converted into theranostic agent by modifying structure with iodine and a H_2S cleavable cage group. High singlet oxygen quantum yield (34%) and fluorescence quantum yield (34%) of **TM-I-H_2S** after activation with H_2S makes it a great candidate for theranostic applications. Phototheranostic efficacy of **TM-I-H_2S** was studied in colorectal cancer cells (HCT116) and triple-negative breast cancer (MDA MB-231). It was concluded that, **TM-I-H_2S** can induce singlet oxygen production in cancer cells with high H_2S level and allows fluorescent imaging at the same time.

ÖZETÇE

Silisyum-Ksanten Tabanlı Fototeranostik Ajanlarının Tasarımı, Sentezi ve Terapötik Etkilerinin İncelenmesi

Sultan Çetin

Kimya, Yüksek Lisans

7 Temmuz 2021

Etkili kanser tedavisi araştırmaları için sarf edilen büyük çabaya rağmen, kanser dünya çapında en çok ölüme sebep olan önemli bir sağlık problemi olmaya devam etmektedir. Tümör heterojenliği, metastaz ve tedaviye direnç, kanser tedavisinin terapötik etkinliği sınırlayan başlıca problemler arasındadır. Terapötik etkinin gerçek zamanlı görüntüleme ile birleştirildiği teranostik yöntem, bu zorlukları azaltmak için gelişen bir modalitedir. Teranostik etki için kullanılan yöntemlerden biri fotodinamik terapinin (FDT) floresan görüntüleme ile kombinasyonudur. Günümüzde, FDT invaziv olmayan tedavi, düşük sistematik toksisite, ihmal edilebilir ilaç direnci ve tümöre karşı bağışıklık sistemi aktivasyonu sundukları için son derece umut verici bir yöntem olarak kabul edilmiştir. FDT aktivitesi, fotoduyarlaştırıcı ajan, ışık ve moleküler oksijen ($^3O_2$) ile etkileşimi sonucunda sitotoksik reaktif oksijen türlerinin (ROS) üretilmesini içerir. Sadece ışık varlığında terapötik etkinin açığa çıkması yönteme seçicilik kazandırması açısından önemlidir. Fakat, kullanılan ışığın penetrasyon derinliğinin dokulara ulaşmada yetersiz oluşu bu yöntemin kinikte yaygın bir şekilde kullanılmasını engelleyen sebepler arasındadır. Bu nedenle, mevcut zorlukları ortadan kaldırabilecek fotoduyarlaştırıcıların geliştirilmesi büyük önem taşımaktadır. Bu çalışmada gelişmiş özelliklere sahip yeni fototeranostik ajanların geliştirilmesi üzerinde durulmuştur.

Bu çalışmanın ilk bölümünde, silikon yerleştirmeli floresein (SF) iyot ile modifiye edilerek elde edilen **SF-I** ilk SF tabanlı ve umut verici fototeranostik özelliklere sahip fotoduyarlaştırıcı molekül olarak literatüre kazandırılmıştır. İlk olarak, SF-I ajanının fotofiziksel özellikleri araştırılmış olup kızıl bölgeye kayan absorpsiyon ve yüksek singlet oksijen kuantum verimi (%45'e kadar) elde edilmiştir. Sonrasında, ilgili ajanın sitotoksik ve floresans görüntüleme etkinliği MDA-MB-231 ve HCT116 kanser hücre hatlarında *in vitro* çalışılmış ve fototeranostik etkisi gösterilmiştir. Fenol grubunun kimyasal modifikasyonu ile **SF-I** ajanının kanser seçiciliği sağlayabilecek ajnların eldesi mümkün görünmektedir.

Çalışmanın ikinci kısmında, kanser seçiciliği yüksek bir fototeranostik ajan elde etmek amaçlanmıştır. Bunun için, silikon yerleştirmeli ksanten iskeleti olan Tokyo Magenta (TM) yapısı iyot ve H_2S (hidrojen sülfür) seçici grubun eklenmesiyle kanser seçici bir fototeranostik ajan haline getirilmiştir (**TM-I-H_2S**). Ajanın, H_2S ile aktifleşmesinden sonra yüksek singlet oksijen (%34) ve floresans kuantum verimlerine (%34) sahip olduğu ispatlanmıştır. Bunun üzerine, ilgili ajanın fototeranostik etkinliği HCT116 kanser ve MDA-MB-231 sağlıklı hücre hattında çalışılmıştır. **TM-I-H_2S**'in H_2S varlığında singlet oksijen oluşumunu indüklediği ve eş zamanlı olarak floresan görüntüleme imkanı sağladığı gösterilmiştir.

AKNOWLEDGEMENTS

First and foremost, I would like to thank my advisor, Dr. Safacan Kölemen, for breaking the record of the most indulgent person I have ever met and changing my understanding of kindness. Graduate school requires hard work and Dr. Kölemen could make you work harder with great enthusiasm owing to his parental guidance, motivational speeches, and positivity. I am very grateful for all the hard work, insights, guidance and support he provides. Thank you so much for being always there when I need to consult, supporting me on my decisions and sharing your experience generously.

I would also like to extend my appreciation to Assoc. Prof. Görkem Günbaş for sharing his expertise with me and giving me the opportunity to do research in his lab. Somehow, I always feel like you are angry with me but still I know I can consult you anytime I need, and you will not withhold your guidance from me. Before him, I would like to thank you Günbaş lab members for their collaboration on my work. To Zübeyir Elmazoğlu for cell studies, Osman Karaman for his helps in the synthesis of TM and Gizem Atakan for any kind of help. Additionally, Figen Varlıoğlu Yaylalı is special for me as she is the best mentor I can ever get. I cannot forget anything she teach me because she made her point with logic every time and she is also great as a person. She can make everything look nice with her positive energy. Also, I want to thank to Dilay Kepil for her friendship and support. Thanks a lot, I am happy to have you.

I am sincerely grateful to Prof. Funda Acar Yağcı for joining my defense as a jury member and contributing my thesis.

I would like to express my appreciations to Assoc. Prof. Önder Metin for being supportive and helpful. Before him I would like to thank all Metinlab members for being great and giving neighbors. They never turn us down when we ask for help. Thanks especially Buse Sündü and Zafer Eroğlu for their help in my reaction and to Melek Sermin Özer and Merve Aksoy.

I would like to extend my appretiations to Dr. Erbay Kalay for his collaboration.

I want to express my special thanks to Dr. Hande Gündüz for her warming and friendly attitude throughout the time we work together. She was always supportive and understanding towards me even the times I am unbearable. I have had some ups and downs and I can never forget you are with me in most difficult time. Thank you so much being there for me when I needed.

Another great person I have met here is Dr. Sibel Eken Korkut. I want her to be in my life as a guide, as someone in family I can consult anything and trust everything coming out of her mouth.

I would like to thank to Zeynep Sena Kulaksız, Merve Ercan, Can Ayra and Hüseyin Küçükkeçeci for their great friendship, advice and for always being considerate about me. Hüseyin is at last for a reason because I want a drama quin.

Cannot forget my great home support Işık Sena Akgün. We have great times together and cannot deny there is no better flatmate than you. Thank you for all your friendship, support and fortune telling.

I would like to express my special thanks to Ahsen Sare Yalın and Aylin Kınık for their sincerity and friendship.

There should be lifelong friends in a person's life and for me it is Bekir Anıl Pala. I thank to him for being always there for me and giving me support in any decision I make without any judgement. Knowing to have you is the best thing I know.

Here comes the dramatic part. Even if I do not write any name here, they would know I am talking about them. I do not know how to leave you and live with different people. Let us start with Çağrı Özsan. You are a person who I can never get along with, but love is bigger. Actually, you are a nut and damn pretty good one. I hope I can find another good nut like you otherwise It would be hard to overcome your absence. Do not expect a thanks here as it would not be enough to express your support. Please be in my life till the end.

We have our little mama Büşra Arslan. Having you around is always comforting as I know someone is handling the things. Your gentle little heart is always on good things not for only yourself but also for everyone even more for others. You are always sincere, caring, and supportive for me even if I hurt you (unconditionally of course). Again, no thanks are enough for you.

Oh, my got Eda Kılıç arrived the lab. Naturally laughed at this part do not know why. May be because of your natural ability to cheer up. Another great support I can always reach, trust and share. No thanks to you just tell me how I can find another person to perform just dance now in the lab.

Ops. We got Musa Dırak. Cannot explain how but I like this person too. You made great impact in my life in a short time and hope to have you longer. What I love about you is you are always honest even if it hurts which is in great conflict with Eda. I hope I am always surrounded by people like you.

There are also other members of the lab I love working with. Thanks to Alperen Acarı, Berkan Bozkurt, Eda Erbil and Zeynep Kılcan for their helps.

There is also Toghrul Almammadov. I would like to thank to him making my life in the lab harder.

I would like to thank to all my bad experiences as well. if they don't happen, I will not be the person I am now. I feel stronger and more resilient thanks to them. All my weaknesses get stronger with these experiences, I guess.

I have a natural ability to find a family environment everywhere I go. The Güler family is my family in Ankara. I love so much all the members of this family and want to have them throughout my life. Thank you so much for all your support Gülten Güler, Esin Güler, Ersin Güler and Efe Güler.

The family I find in İstanbul is the Kılıç family. They are also supportive and great family, and it was great to spend time with them. Thank you so much Serpil Kılıç, Mahmut Kılıç and Eyüp Okay. Of course, additional special thanks to Serpil Kılıç for her great foods.

On top of all, I have a great supportive family make me feel free of doing rights and wrongs. Giving me opportunity to find my own way and feel their support on my way. Thanks is not enough for my mom Fatma Çetin and my dad Ömer Çetin. Instead, I promise you I am always gonna make you proud. I may sometimes complain about my siblings, but I am always happy to have them. So, thanks to Mehmet Çetin, Hamit Çetin, Emirhan Çetin and Zehra Çetin. Special thanks to my sister Kudret Çetin who I grow up with, have fun with and fight with. Also, thanks to her for giving me my little nephew Ömer Enes Uzun who bring cuteness in my life. I love you all.

I would like to thank TUBITAK for financial support for the project with project no:117Z901.

TABLE OF CONTENTS

LIST OF TABLES

LIST OF FIGURES

ABBREVIATIONS

QD	Quantum Dot
PDT	Photodynamic Therapy
ROS	Reactive Oxygen Species
TPE	Tetraphenylethylene
AEI	Aggregation Induced Emission
HOMO	Highest Occupied Molecular Orbital
DFT	Density Functional Theory
CIEEL	Chemically Initiated Electron Exchange
HIF	Hypoxia Inducible Factor
EWG	Electron-withdrawing Group
GSH	Glutathione
LOD	Limit of Detection
ECM	Extracellular Matrix
GGT	Gamma-glutamyl Transferase
NQO1	NAD(P)H Quinone Oxidoreductase
FAD	Flavin Adenine Dinucleotide
PBS	Penicillin-binding Protein
LAP	Leucine Aminopeptidase
EPR	Permeability and Retention
EGF	Epidermal Growth Factor
PMA	Phorbol 12-myristate 13-acetate
DOX	Doxorubicin
CPT	Camptothecin
DSP	Succinimidyl Propionate
FR	Folate Receptor
PNT	Peroxynitrite
TMS	Tetramethyl silane
EDTA	Ethylenediaminetetraacetic acid
DCC	N, N'-Dicyclohexylcarbodiimide

PS	Photosensitizer
SF	Silicon fluorescein
TM	Tokyo Magenta
WHO	World Health Organization
NIR	Near-IR Region
MOF	Metal-Organic Framework
TCPP	Tetrakis(4-carboxyphenyl)porphyrin)
ISC	Inter-System Crossing
SOC	Spin Orbital Coupling
Bpy	Bipyridine
PTT	Photothermal Theraphy
NTR	Nitroreductase
HPT	Hematoporphyrin
PeT	Photo-Induced Electron Transfer
DNBS	Dinitrobensensulfonate
BODIPY	Boron-dipyrromethene
MAO	Monoamine oxidase
Ppm	Parts per Million
s	Singlet
d	Doublet
t	Triplet
m	Multiplet
RPMI 1640	Rosswell Park Memorial Institute
DMEM	Dulbecco's Modified Eagle Medium
MEM	Minimum Essential Medium
FBS	Fetal bovine serum
MTT	Thiazolyl blue tetrazolium bromide
TLC	Thin Layer Chromatography
THF	Tetrahydrofuran
DCM	Dichloromethane
DIEA	N,N-Diisopropylethylamine
n-BuLi	n-Butyllithium
EtOAc	Ethyl Acetate

DMF	Dimethylformamide
t-BuLi	tert-Butyllithium
TFA	Trifluoroacetic Acid
MeCN	Acetonitrile
sec-BuLi	sec-Butyllithium
EtOH	Ethanol
PMT	Photomultiplier
PTFE	Polytetrafluoroethylene
DMSO	Dimethyl sulfoxide
QY	Quantum Yield
ADMDA	2,2'-(anthracene-9,10-diyl)bis(methylene)dimalonic acid
MB	Methylene Blue
SOSG	Singlet Oxygen Sensor Green
MeOH	Methanol
OD	Absorbance at Excitation intensity
DCFH-DA	2′,7′-dichlorodihydrofluororescein diacetate
PI	Propidium Iodide
NBS	N-Bromosuccinimide
TNBC	Triple Negative Breast Cancer
$DCFH_2$-DA	2',7'-dichlorofluorescein diacetate
MeCN	Acetonitrile
CT	Computed Tomography
MRI	Magnetic Resonance Imaging
SPECT	Single Photon Emission Computed Tomography
ATP	Adenosine Triphosphate
FAAH	Fatty Acid Amide Hydrolase
CRET	Chemiluminescence Energy Transfer
QD	Quantum Dot
PDT	Photodynamic Therapy
OPV	Oligo (*p*-Phenylene Vinylene)
ROS	Reactive Oxygen Species
TPE	Tetraphenylethylene
AIE	Aggregation Induced Emission

TSH	Thyroid Stimulating Hormone
HOMO	Highest Occupied Molecular Orbital
DFT	Density Functional Theory
BeT	Back Electron Transfer
HIF	Hypoxia Inducible Factor
EWG	Electron-withdrawing Group
GSH	Glutathione
LOD	Limit of Detection
EMT	Epithelial to Mesenchymal Transition
Cbz	N-carboxylbenzyl
ECM	Extracellular Matrix
NQO1	NAD(P)H Quinone Oxidoreductase
FAD	Flavin Adenine Dinucleotide
PBS	Penicillin-binding Protein
NCMA	Non-metallo Carbapenemases of Class A
RT-PCR	Reverse Transcriptase Polymerase Chain Reaction
MALDI-TOF	Matrix Assisted Laser Desorption Ionization Time of Flight
LAP	Leucine Aminopeptidase
PI-LAP	Puromycin-insensitive Leucine Aminopeptidase
CES2	Carboxylesterase 2
CDKs	Cyclin-dependent Kinases
ATM	Kinases Ataxia-Telangiectasia Mutated
ATR	Ataxia-Telangiectasia and Rad3-related Protein
NHEJ	Non-homologous End-joining
HR	Homologous Recombination
EPR	Permeability and Retention
PGA	Penicillin-G-amidase
PDGF	Platelet-derived Growth Factor
EGF	Epidermal Growth Factor
PMA	Phorbol 12-myristate 13-acetate
DOX	Doxorubicin
CPT	Camptothecin
DSP	Succinimidyl Propionate

FR	Folate Receptor
LPS	Bacterial Lipopolysaccharides
NK	Natural Killer
GMC	Gemcitabine
CBL	Chlorambucil
PNT	Peroxynitrite
NSAID	Non-steroidal Anti-inflammatory Drug
MMAE	Monomethyl Auristine E
TMS	Tetramethyl silane
EDTA	Ethylenediaminetetraacetic acid
ACN	Acetonitrile
Hex	Hexane

Chapter 1:
INTRODUCTION

1.1 Cancer

Cancer can be defined as complex sequence of disease conditions with stepwise progression initiated by molecular alterations and result in a region with uncontrolled growth.[1] Proliferation of cancerous cells cannot be controlled as they are able to escape from natural mechanism of cell death owing to alterations like abnormalities in nucleotide sequences and chromosomes ultimately cause tumors or neoplasm.[2,3] Cancer is a genetic disorder with various somatic mutations and can also result from recurrent exposure to carcinogens including tobacco smoke, ultraviolet light, insistent tissue injury.[4–6] Additionally, some viral infections may cause genetic and epigenetic changes, eventually lead to the initiation, progression, and metastasis of this disease.[5]

Despite all technological improvements and extensive research on cancer treatment, recent cancer statistics show death rate related with cancer is predicted to increase more and more.[7,8] High mortality rate of cancer is mostly related with recurrence of disease, consequences of treatment and metastasis of disease especially distance metastasis.[9] Metastasis is defined as complex process that cancer cells spread specific organs including lung, brain, liver, and bone.[3,10,11] Conventional therapies like chemo and radiation treatment or surgical removal of metastatic lesions are unsuccessful as metastasis is usually multiple and resistant to these therapies.[5] There is clear need for deeper understanding of tumor microenvironment and metastasis to design more effective therapies for cancer so there is an immense interest in cancer research.[4,12,13] Additionally, according to cancer statistics of World Health Organization (WHO) there is an urgent need for cancer therapeutic strategies with less side effects and higher therapeutic efficiency.[7]

1.2 Traditional Cancer Therapy Modalities

The development of cancer can be originated from dysregulation of regulatory proteins in microenvironment of benign tumor.[5] Resulting cancer is a versatile disorder with complex modifications in the genome which is affected by the interplay between

host and environment. Multifactorial nature of cancer challenges treatment and requires customized therapeutic modality.[5] After the recognition of the malignancy, immense effort has been made to understand every aspect of disease and discover the treatment for cancer. Until 1950, surgery that is simply the removal of malignant tissue was the only choice of treatment.[5,14,15] Then, radiation therapy was emerged and effectively used to control local disease.[16] It is based on high energy radiations enabling the use of electrons, protons, and various ions to kill the cancerous cells. High energy radiations damage genetic material of cells to stop cell division and proliferation.[16] Additionally, combination of surgery and radiation was employed and reported as more successful than individual treatment.[15,17] Radiation therapy can be performed before surgery to shrink the tumor or after to destruct the remained tumor cells and reduce the risk of recurrence. [17,18]As both modalities act in a localized manner, another method is required for systemic cancers.

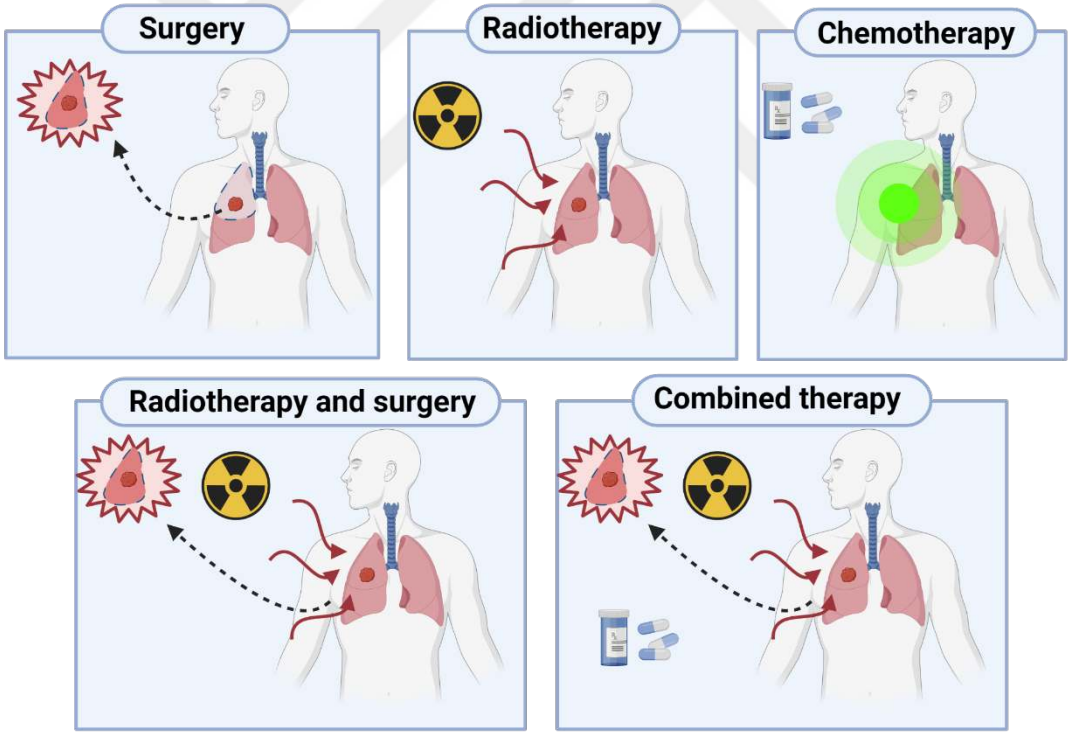

Figure 1.1 Representation of traditional cancer treatment modalities.

Chemotherapy was emerged during the study of therapeutic effect of nitrogen mustard on lymphoma which is the cancer of the lymph nodes during World War II.[19] This modality is based on the DNA damage of rapidly growing cancer cells as a result

cell death.[19] This study was pioneer for a long series of similar but more effective agents called alkylating agents. Short after, aminopterin was introduced by Sidney Farber as an agent that inhibits a critical chemical reaction for DNA replication.[19] This agent is precursor of chemotherapy drug, methotrexate, that is used commonly today.[19] Thenceforth, several chemotherapy drugs that inhibit different functions in cell growth and replication were discovered. Nowadays, surgery, radiotherapy, chemotherapy, and combination of two or all of them become the traditional and mostly employed methods in cancer treatment.[15,17,19] So far, chemotherapy has been considered as the most effective and most employed method covering the treatment of different types of cancers. Clinically employed chemotherapy drugs destroy tumor cells by the means of genotoxicity but also damage healthy cells leading diverse dose-dependent side effects fatigue, nausea, hair loss, and vomiting or even death in extreme cases.[20] There are studies to improve selectivity of chemotherapy drugs, yet structural modification of these drugs is not easy or impossible for some.[11,12,14,21]

Nowadays, surgery, radiotherapy, chemotherapy, and combination of two or all of them become the traditional and mostly employed methods in cancer treatment. Side effects associated with traditional methods of cancer treatment highlights the scope of novel cancer treatment methods. Some of the modern modalities include hormone-based therapy, anti-angiogenic modalities, stem cell therapies, immunotherapy, and dendritic cell-based immunotherapy.[5,21] Current studies on cancer treatment are mostly based on development of targeted drugs, biological molecules, and therapies activating immune system rather than suppressing.[12,22–24]

1.3 Photodynamic Therapy

Photodynamic therapy (PDT) shows great potential for cancer treatment, as it offers non-invasive treatment, low systemic toxicity, negligible drug resistance and immune system activation against the tumor.[25] One of the advantages of PDT, toxicity is activated within pathological tissues with light irradiation.[26] That is, the method is inherently selective with light activation. Also, PDT is a painless and simple method requiring less time for recovery compared to traditionally employed methods. PDT can also be applied in combination with these traditional therapies to enhance the therapeutic effect, such as chemotherapy and radiotherapy through synergistic effect.[5,24,25,27]

There are currently seven approved PDT drugs available for application in the clinic globally,[28] although the first clinical applications were initiated more than a century ago by von Tappeiner.[29] Almost all clinically approved PDT agents are porphyrin derivatives. For instance, two well-known PDT drugs Photfrin (porfimer sodium, the first approved PDT drug) and Foscan (Temoporfin). However, when these two drugs were tested under hypoxic conditions it was shown that their photocytotoxicity were almost completely inhibited.[30] Additional obstacles for both include limited penetration depth of incident light through tissues hindering their widespread application of PDT.

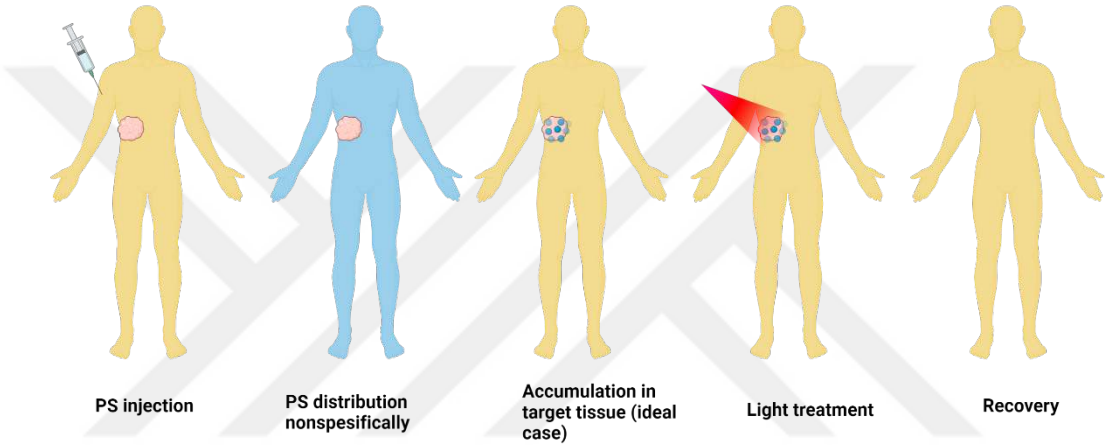

Figure 1.2 Schematic illustration of the application of Photodynamic therapy (PDT).

Despite effective use of PDT in clinic for certain cancers such as liver malignancies, its utility is hampered for several reasons.[24] First, sensitivity of some PSs may be questionable due to greater absorption in normal tissues than malignant tumors.[31] Penetration depth of incident light through tissues is another issue hampers the treatment of deeper tissue. It is known that light in the red/NIR region of the spectrum penetrates deeper as biological chromophores have less interference in that region.[26,32,33] Therefore, one of the major requirements of a PDT agent is the strong absorption band at red or near-IR (NIR) region of the electromagnetic spectrum where auto-fluorescence and interference of biological chromophores is eliminated resulting in deep tissue penetration of light.

Another issue is the oxygen need of PDT. The most common feature of solid tumors is the generation of hypoxic microenvironment as a consequence of rapid cell proliferation as well as insufficient and distorted vasculatures around the tumour region.[34]

The cancerous cells adapt hypoxic environment owing to upregulation of hypoxia-inducible transcription factors (HIFs) and related overexpression of P-glycoprotein (P-gp).[35] HIFs are also reducing the efficacy of conventional therapies because they maintain survival of cancer cells under hypoxic conditions and becoming more resistant to chemotherapy drugs.[36] Yet, this problem is more pronounced in the case of PDT as singlet oxygen generation is highly dependent on oxygen. Several innovative approaches were proposed to overcome the limitations of tissue hypoxia. Studies include hyperbaric oxygen therapy and the use of oxygen carriers like perfluorocarbons or artificial red blood cells and oxygen-self supplying agents (catalase, MnO_2 and CaO_2).[37–39] However, these studies end up with significant side effects such as barotrauma and hyperoxic coma. Another highly attractive approach is to localize PDT drugs to the mitochondria where most of the oxygen is present in a cell.[40–44] Mitochondria has great importance in cell respiration, oxygen metabolism and apoptosis signaling.[45,46] mitochondrial accumulation and retention is achieved by cationic agents due to negative transmembrane potential of it.[47–50] Accordingly, mitochondria-targeted PDT agents exhibit improved cytotoxicity even under hypoxic conditions as a result of high mitochondrial oxygen content and the resultant mitochondria-induced apoptosis.[49,51–53]

In recent years, there is a growing interest towards designing new generation photosensitizers that can address the chronic problems of PDT.[54,55] In attempt to tackle the light penetration issue, most popular method is to design PSs with red/NIR absorption where intrinsic absorption of biomolecules and scattering is less.

1.3.1 Mechanism of PDT

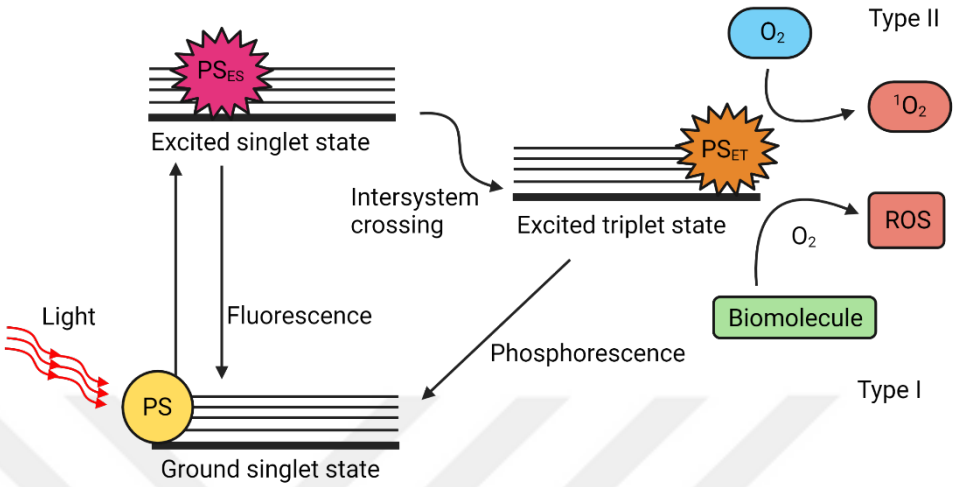

Figure 1.3 Modified Jablonski energy level diagram for PDT action.

PDT involves the generation of cytotoxic reactive oxygen species (ROS) through the interaction of a photosensitizer (PS), light and molecular oxygen ($^3O_2$). In a typical PDT action, PS irradiated with light excited to singlet excited states from its ground state. At that state, PS may relax back to ground state by emitting light, called fluorescence or can undergo inter-system crossing (ISC) to form long-lived triplet excited state (Figure 1.3). These two relaxation pathways are competing pathways so a PS with high triplet quantum yield will lose its fluorescence property. After ISC, triplet excited state energy can be released either by phosphorescence with relaxation to ground state or can be transferred to the dissolved molecular oxygen in its ground state (triplet oxygen) yielding highly reactive oxygen species (ROS).[56] In type I PDT, hydroxy radical and super oxide are formed, while singlet oxygen ($^1O_2$) is produced in type 2 reaction. Current PSs are known to produce singlet oxygen predominately for the therapeutic action.[56] Direct excitation of ground state oxygen to singlet oxygen is strictly forbidden by selection rules. That is why photosensitization is necessary to produce ROS. Generated ROS reacts with vital biomolecules including nucleic acids, proteins, and unsaturated lipids resulting in cell death through apoptotic or necrotic pathways.[57,58] PDT is a promising option for state-of-the-art treatment methods like chemotherapy and radiotherapy, for clear reasons such

fewer side effects and immune system activation against cancer cells rather than suppression.

In order to facilitate ISC, the most commonly investigated method is to take advantage of the heavy-atom effect that can be acquired by the use of coordination centers (Ir(III), Pt(II), Ru(II), etc.) or alternatively use of heavy atoms (I, Br, Se, etc.).[59–62] Presence of heavy atoms or heavy transition metals in the structure induces a strong transition between singlet and triplet states determined by spin orbital coupling (SOC).[62] Larger heavy-atom effect is expected for atoms with high atomic number. Therefore, most of the Ir(III), Pt(II), and Ru(II) transition-metal complexes display efficient and ultrafast ISC.[62] For instance, $[Ru(bpy)_3]^{2+}$ (bpy = 2,2′-bipyridine) shows 100% triplet-state quantum yield but considerations on scarcity of heavy metals and the toxicity and is shifting interest in organic molecule-based PSs. However, compare to transition metal complexes the organic molecules have weak spin orbit coupling and resulting low triplet state quantum yield. In this perspective, mostly employed method to push ISC is to modify organic dyes with heavy atoms like iodine, bromine, etc. Vast number of PSs have been investigated for effective PDT with heavy atom modification. [52,63–66]

As a summary, an effective PS should apply low dark toxicity, strong absorbance at the excitation wavelength in red-NIR region, high $^1O_2$ quantum yield for and selectivity towards cancer cells to induce tumor-selective, strong phototoxicity.[26,27,67]

1.4 Fluorescence Imaging

Fluorescence is simply defined as the ability of a molecule to emit light that is absorbed a particular wavelength. First, molecule is excited with light in a certain wavelength and goes to the singlet excited state. At that state, possible relaxation pathways are emission of light, or undergoing inter-system crossing (ISC) or nonradiative relaxations (Figure1.3).[68] ISC results in long-lived triplet excited state, so it is a forbidden transition. ISC and fluorescence are two competing pathways so a molecule with high triplet quantum yield will lose its fluorescence property. The relaxation to ground state by releasing luminescence is referred as fluorescence. Florescent imaging agents are popular and promising option in cancer diagnosis studies as they yield images with spatial and temporal resolution and serve ease of operation and low cost.[69–72] Also, they are easy to be modified to increase sensitivity and selectivity through activatable agents. In

addition, fluorescent probes can serve as non-invasive real-time measurement agent without harming the cells and tissues.[73] However, widespread application of fluorescent imaging is hampered by limited penetration of the emitted light in tissues, especially in *in vivo* applications, and selective *in vivo* imaging with cancer cell activatable designs are in limited number. Therefore, vast of effort have been put to develop fluorescent imaging agents, which emit in the highly penetrating red or near infrared (NIR) region and can be activated only in cancer cells.[73] Activation is generally achieved by using a masking group that will be removed in the presence of cancer-related biological analytes in the tumor region.[74–76] Herein, development of new activatable agents depends on the research enlightening the tumor microenvironment. So far, several analytes including enzymes have been introduced and cage groups and probes are developed for some[77–80]. Development of new fluorescent probes also contributes development of PDT agents as it may be possible to convert a fluorescent imaging agent into a PDT agent through structural modifications. As mentioned in above ISC can be facilitated by heavy-atom effect that can be acquired by the use of coordination centers (Ir(III), Pt(II), Ru(II), etc.) or alternatively use of heavy atoms (I, Br, Se, etc.).[59,81] Fluorescent quantum yield of heavy atom modified molecule decreases due to effective ISC which is a competing pathway to fluorescence. However, fluorescence may not be completely quenched in such a way that imaging can be still possible with subjected molecule in combination with PDT called phototheranostic agents.[82,83]

1.5 Theranostic Approach: Combination of Therapy and Diagnosis

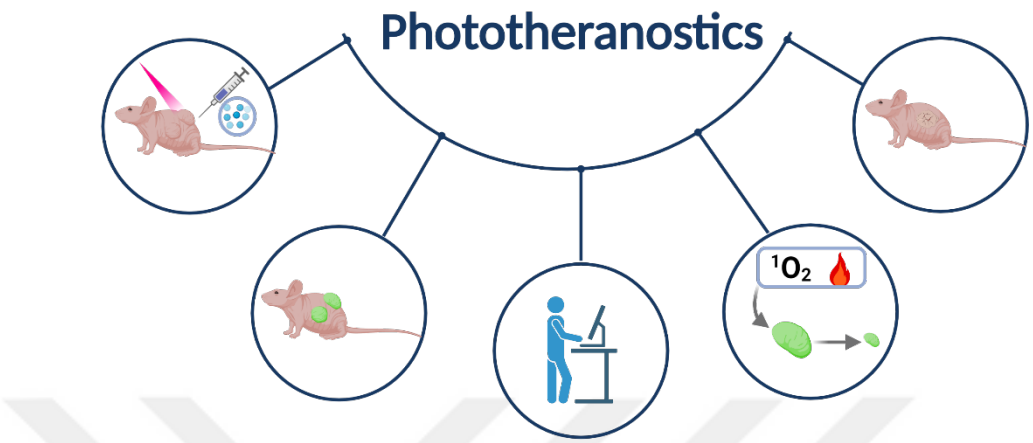

Figure 1.4 Representative working principle of phototheranostics.

The development of optical technology fastens the research on phototheranostics which combine simultaneous light-induced imaging with therapy.[84,85] Recently, phototheranostics have attracted great attention in the field of cancer theranostics. So far, remarkable progress in phototheranostics has been made and theranostic systems allowing imaging guided therapy. Beside phototheranostic nanoplatform several small organic molecule-based multimodal phototheranostic agents have been introduced in recent years.[43,63,86]

For example, in our previous work, we demonstrated PTT potential of brominated hemicyanine (Figure 1.5) under a single (640 nm or 808 nm) and dual laser (640 nm + 808 nm) irradiation in addition to its PDT potential. Both single 640 and 808 nm caused a significant cell death at 30 and 300 mW, and 1000 mW laser power, respectively on HeLa and SW480 cell lines after 5 min irradiation. Since the such strong therapeutic effect of **HC-1** was shown to be turned on by irradiation at 640 and 808 nm at the selected location that may be determined by the fluorescence of **HC-1** owing to reasonable fluorescence quantum yield (12%). That is, this work summarizes the realization of a strong image-guided multi-modal phototherapy via NIR and safe laser irradiation.[63]

In a different work, another NIR emissive activatable hemicyanine dye **ICy-N** was developed by decorating structure with iodine and 4-nitrobenzyl bromide for selective

phototheranostic activity (Figure 1.5).[86] **ICy-N** with cage group has no phototoxicity which is activated by removal of cage group with nitroreductase (NTR) activity. In this study, change in photophysical properties under hypoxic and normoxic conditions were studied since NTR is overexpressed under hypoxic conditions. It was proved that 4T1 cells exhibited no fluorescence under normoxic conditions while it induced strong fluorescence under hypoxia. In *in vivo*, there was no growth in tumor volume after the irradiation of **ICy-N** at 100 mW/cm^2 for 20 min while 5-fold increase was observed with only laser or **ICy-N** treatment. Additionally, *in vivo* studies carried out in Balb/c mice demonstrated that **ICy-N** is an efficient photosensitizer for restraining tumor growth through the PDT effect and offers precise tumor hypoxia imaging.

In another study **CYBF$_2$** was introduced by Zhao and co-workers as effective PDT agent. **CYBF$_2$** is a boron difluoride complex modified cyanine (Figure 1.5). The group was evaluated therapeutic action of **CYBF$_2$** in MCF7 cells based on various concentrations and light doses and reported that MCF7 cells showed strong fluorescence when treated with **CYBF$_2$** after 10 minutes. Then, **CYBF$_2$** was found to be cytotoxic due to PDT action and accumulates in mitochondria enhancing the PDT efficiency.[87]

1.6 Development of Small Organic Molecule Based Phototherapy Agents

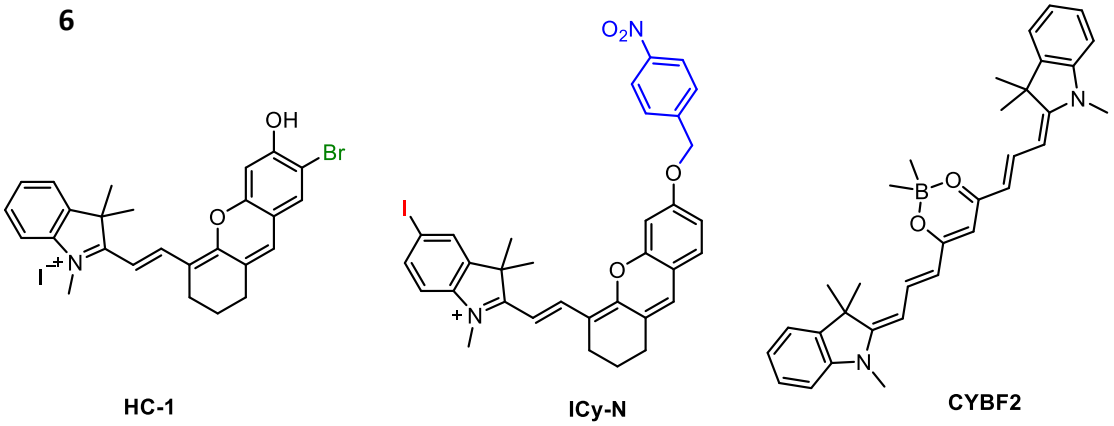

Figure 1.5 Small organic molecule based phototheranostic agents.

Photodynamic effect was first discovered in the early 20th by Von Tappeiner and Jesionek.[29] Yet, there was no significant improvement until the emergence of the sensitizer, which is purified as a byproduct during the synthesis of hematoporphyrin by Lipson in **1960** and later called hematoporphyrin derivative (HPT) (1) (Figure 1.6).[88] After the synthesis of HPT and discovery of photodynamic effect, Dougherty and his

colleagues demonstrated that HPT, was effective in the treatment of mammalian tumors through activation with light.[89] Further, Kelly and Snell conducted their first PDT study on humans using HPT for bladder cancer treatment.[90] After all these important developments, HPT received the necessary legal approvals and started to be applied in the clinic under the trade name Photofrin in the treatment of cervical, esophageal, gastric, and endobronchial cancers.

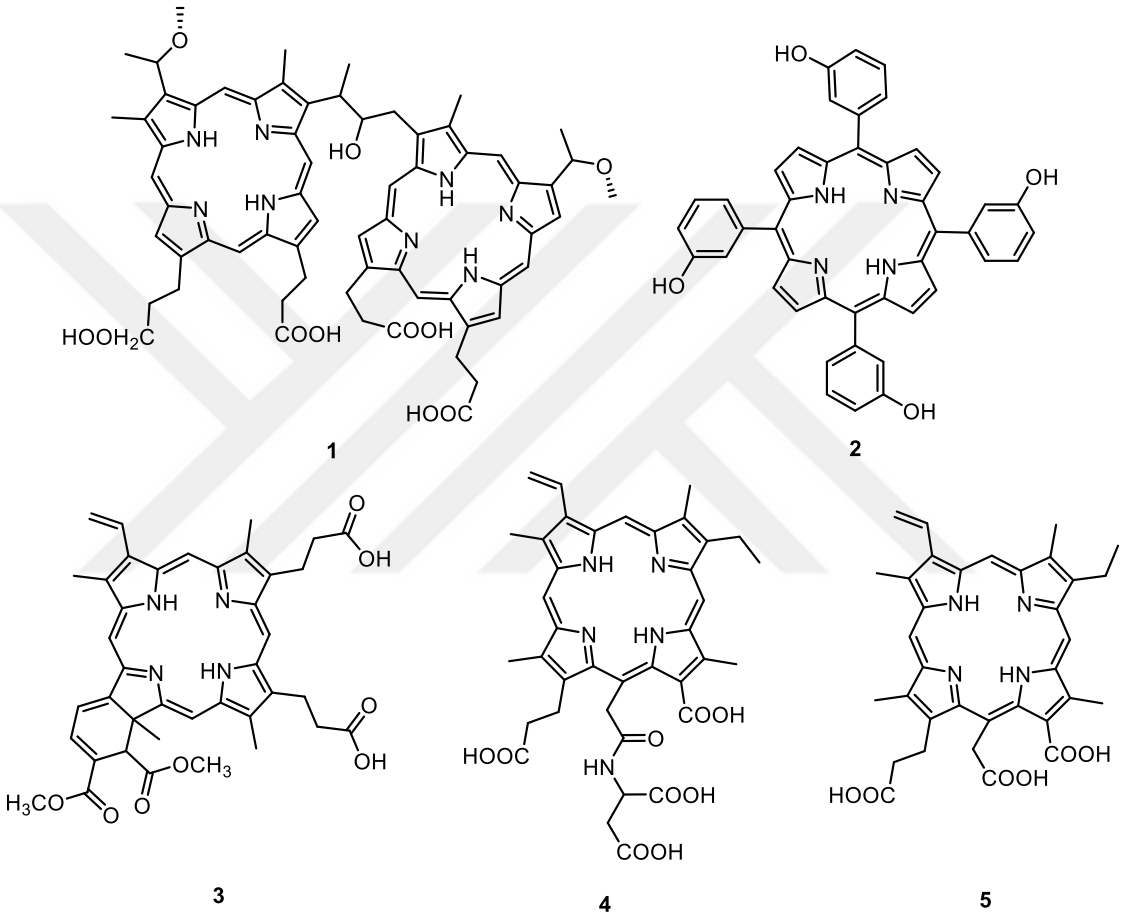

Figure 1.6 Porphyrin based pioneer PDT agents.

However, short wavelength absorption and low absorption coefficient of photofrin cause skin sensitivity leaded by light. Foscan **(2)** and Visudyne **(3)** agents have been developed to solve problems of photofrin (Figure 1.6). Although these PDT drugs have a longer wavelength absorption maximum than Photofrin and show less skin sensitivity, it has been found that these sensitizers precipitates in the body due to their hydrophobic structure.[91,92] In later years, the derivatives of chlorine, which is a reduced form of porphyrin laserphyrin (**4**) and Photolon (**5**) was developed. (Figure 1.6) Yields of these

sensitizers in PDT were not as high as expected since they are hydrophilic and not photostablable.[93]

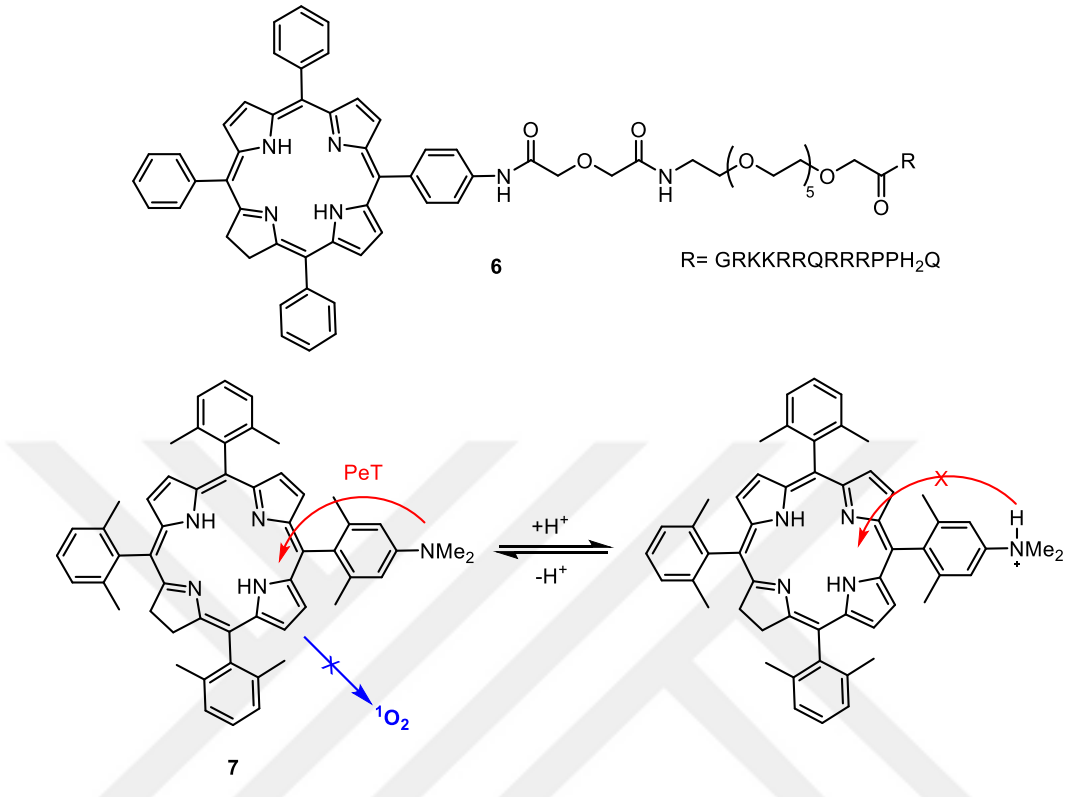

Figure 1.7 Activatable porphyrin-based PDT agents that selectively target the cancerous cell.

Recent studies are on PDT agents that can be activated in a cancerous cell or selectively targeting cancerous cell are of great interest they minimize possible side effects on healthy tissues.[74] In this regard, porphyrin derivatives that can be controlled for singlet oxygen production or can be directed to accumulation in cancerous cells are also frequently used in PDT studies.[94] For example, in the study conducted by Seghal and his colleagues, the porphyrin skeleton was modified with a peptide **(6)** to selectively direct to the prostate tumor (Figure 1.7).[95] Obtained photosensitizer **(6)** was shown to be more effective in cell death compared to HPT. In another study, tetraphenyl porphyrin modified with amine group **(7)** to achieve activation with pH (Figure 1.7).[96] In this design, singlet oxygen production blocked by photo-induced electron transfer (PeT) from aniline group. Electron transfer was interrupted, and sensitizing became active as a result of protonation of the amine group at low pH values (pH 5-6) adjusted to mimic tumor microenvironment (Figure 1.7). PeT is a very common photophysical process for controlling singlet oxygen production. As photo-induced electron transfer occurs faster than the transition between

systems, singlet oxygen production is interrupted in the molecule till PET stops with a molecular change.

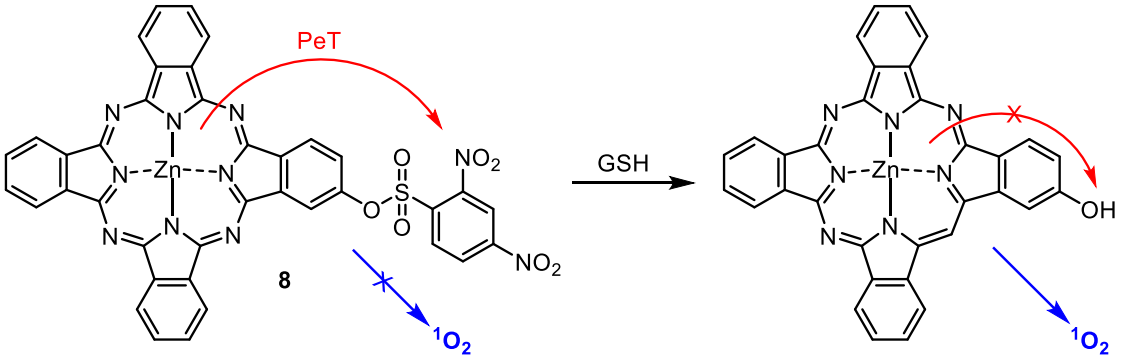

Figure 1.8 PDT agents based on phthalocyanine activated by cancer-related inputs.

Phthalocyanine derivatives are another fundamental sensitizing skeleton that has been used as PDT agent for many years like porphyrin. In the past 10 years, various phthalocyanine -based sensitizers that can be selectively activated in cancerous cells have been developed.[94] In one of these studies zinc-phthalocyanine was modified with the 2,4-dinitrobensensulfonate (DNBS) group known as the electron-acceptor group (Figure 1.8).[97] This modification inactivates singlet oxygen production due to photo-induced electron transfer in the presence of DNBS group. Electron transfer stops when GSH, which is known to be found in high concentrations in cancer cells, removes the DNBS group, and the PDT agent effectively induces singlet oxygen production. This agent was shown to perform PDT effectively in MCF-7 cancer cells.

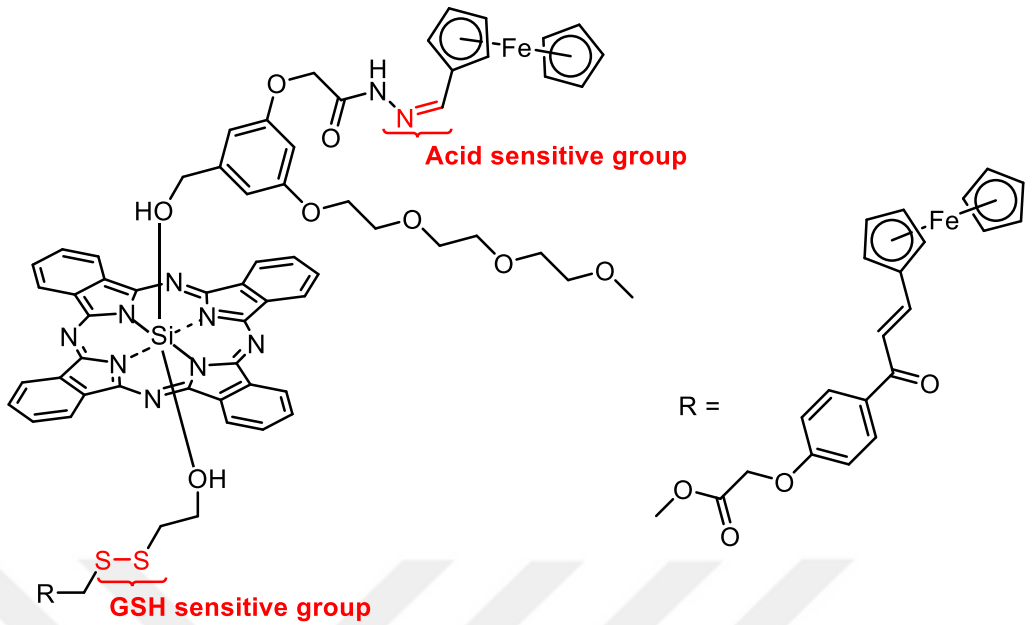

9

Figure 1.9 Zinc-phthalocyanine modified with hydrazon and ferrosen groups through disulfide bond.

In another study published by Ng and his colleagues in 2014, the PDT effect of zinc-phthalocyanine **(9)** was interrupted by incorporating hydrazon and ferrosen groups with disulfide bond to the structure (Figure 1.9). As a result of the protonation of hyrazone in acidic (pH 4.5-6.8) conditions and cleavage of disulfide bond with GSH which is known to overexpressed in cancer cells, the active sensitizer is released and produce singlet oxygen to induce cell death.[98] Further examination MCF-7 cells treated with **(9)** under confocal microscope revealed light stimulated cell death. Thus, an effective PDT agent activated in the presence of two different biological inputs associated with cancer cells was introduced. Such studies continue with targeting enzymes like protease, caspase that are overexpressed in cancer cells.[74]

Despite the widespread application of porphyrin and phthalocyanine based PDT agents, the synthetic problems they have and the difficulties in controlling their photophysical and biological properties have prompted researchers to develop other sensitizers. In this direction, boron-dipyrromethene (BODIPY) (Figure 1.10) derivatives have emerged as a good alternative with important properties such as relatively easy synthesis, high absorption coefficient, easy modification of skeletal structures and control of their photophysical properties by chemical modifications and have been successfully used in PDT studies for many years.[99]

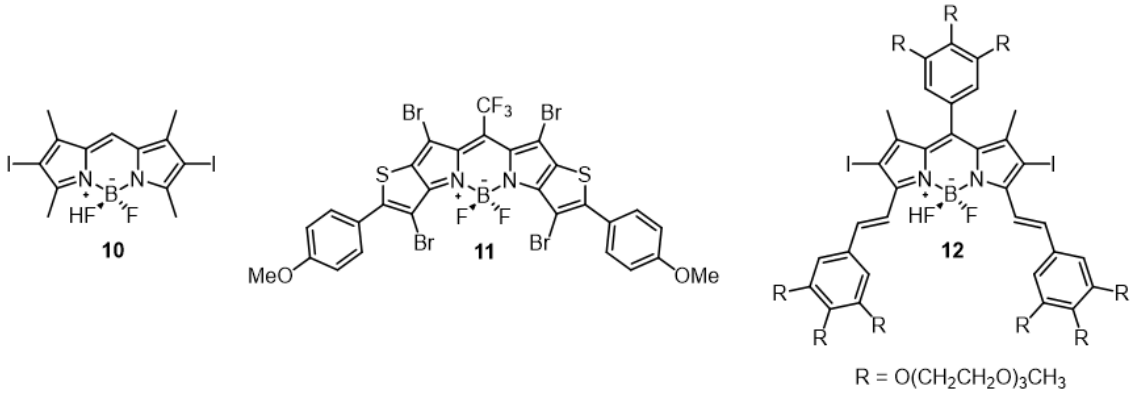

Figure 1.10 BODIPY based heavy atom modified PDT agents.

The BODIPY skeleton alone has a very low inter-system transition efficiency and therefore not suitable for PDT studies. The most basic approach to convert the BODIPY skeleton into PDT agent is to increase spin-orbit coupling which pushes intersystem crossing by modifying structure with heavy atoms such as iodine and bromine.[100] The first diiodo-BODIPY derivative (**10**) was introduced by Nagano and his colleagues in 2005 (Figure 1.10).[101] Following this, several, BODIPY derivatives with improved properties like absorption at longer wavelength **(11)** and high water solubility **(12)** (Figure 1.10).[102,103]

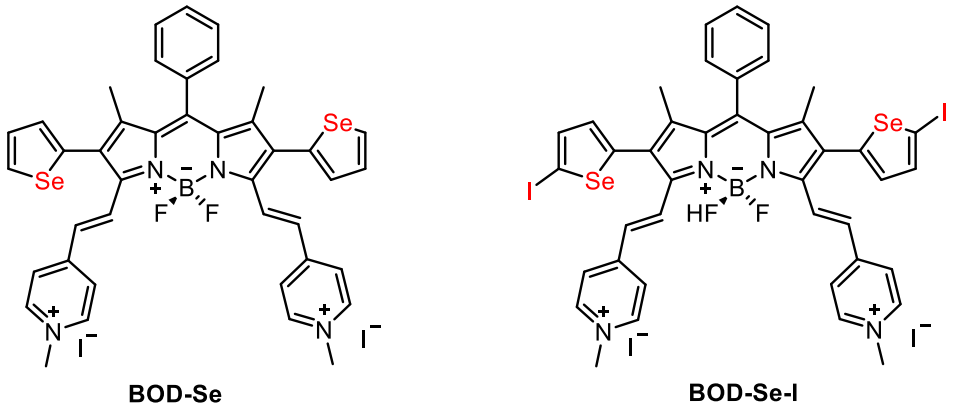

Figure 1.11 Mitochondria targeted BODIPY derivatives.

These pioneering studies was followed by BODIPY derivatives that are selectively activated in cancerous cells by sensing the environmental difference of cancer cells such as low pH, overexpressed enzymes etc.[99] However, BODIPY-based PDT agents have hydrophobic nature like porphyrin and phthalocyanine. Therefore, structural modifications are necessary to make them suitable for PDT studies, or transport with a

carrier in a hydrophilic environment are required. These requirements hamper the use of BODIPY agents *in vivo* and clinical trials.

Two red-absorbing, water-soluble and mitochondria (MT)-targeting selenophene-substituted BODIPY derivatives (**BOD−Se**, **BOD−Se−I**) were introduced by Karaman and colleagues (figure 1.11). PDT effect of these agents were studied the enhanced PDT action in relation with heavy-atom effect was evaluated. It was reported that better $^1O_2$ generation obtained with **BOD−Se−I** owing to higher heavy atom effect. Additionally, **BOD−Se−I** was demonstrated to differentiate cancer cells over normal cells since it shows better PDT effect under hypoxic conditions due to mitochondria accumulation.[52]

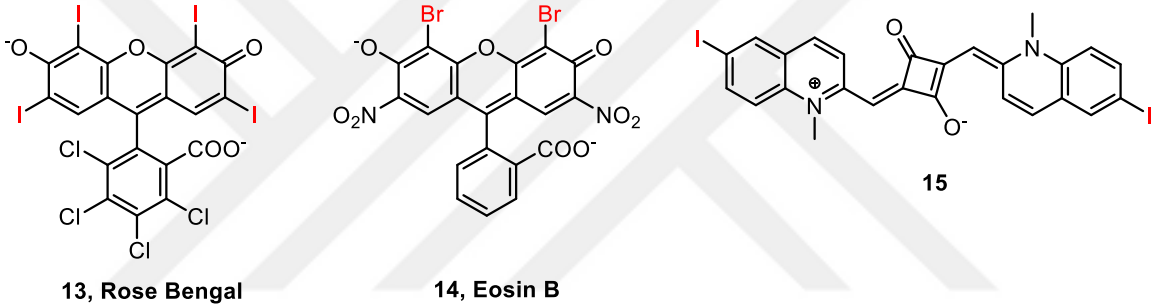

Figure 1.12 Heavy atom modified PDT agents.

In addition to extensively studied porphyrin, phthalocyanine and BODIPY derivatives, PSs with various structures with or without heavy atoms were studied. For instance, Rose Bengal **(13),** Eosin B **(14)** which are fluorescein derivatives modified with iodine or bromine (Figure 1.12).[104] These are the only fluorescein-based examples for long time, and they have problems with tissue permeability and phototoxicity due to their absorption at low wavelength. Another skeleton is the squaraines fluorophore decorated with heavy atoms (**15**) (Figure 1.12).[105] Although such PDT agents can absorb light in

red region of the spectrum, their reactive nature is problematic for intracellular applications.

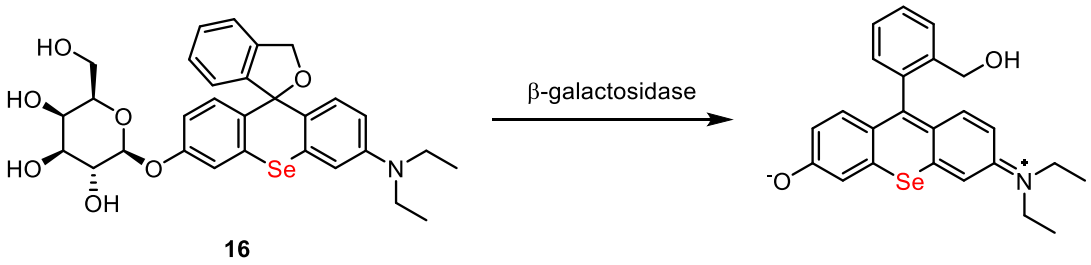

Figure 1.13 Activation of selenium modified xanthene-based PDT agent.

Selenium-substituted xanthone derivative synthesized by the Nagano group in 2014 are another important skeletal structure for PDT studies. In this study, a PS activated by the enzyme β-galactosidase (**16**) was designed (Figure 1.13).[106] Absorption and the singlet oxygen generation of the PS skeleton was masked with cage group since lactone formation breaks the conjugation on the agent. The removal of the cage group with selective enzymatic reaction enables the activation of singlet oxygen production. The synthetic challenges of selenium-substituted xanthone seem to be the most fundamental problem of these sensitizers.

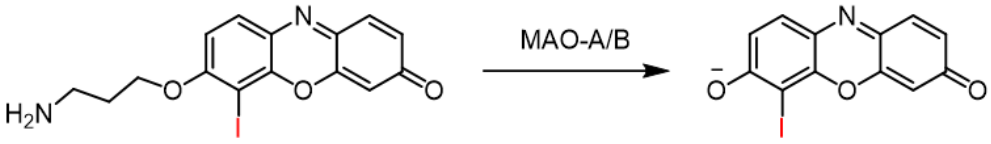

Figure 1.14 Activation of iodinated resorufin with MAO isoforms

A red-absorbing, water-soluble, and iodinated resorufin derivative was introduced by Almammadov *et al.* as an activatable agent **(R1)** (Figure 1.14). PDT potential of this monoamine oxidase (MAO) enzyme activatable core was evaluated and results showed that **R1** possesses high $^1O_2$ generation yields in aqueous solutions upon addition of MAO isoforms (MAO-A, MAO-B). Additionally, **R1** induced photocytotoxicity with endogenous MAO enzyme in SH-SY5Y neuroblastoma cells having MAO-A overexpression. **R1** has ability to differentiate cancer and normal cells, without any considerable dark toxicity.

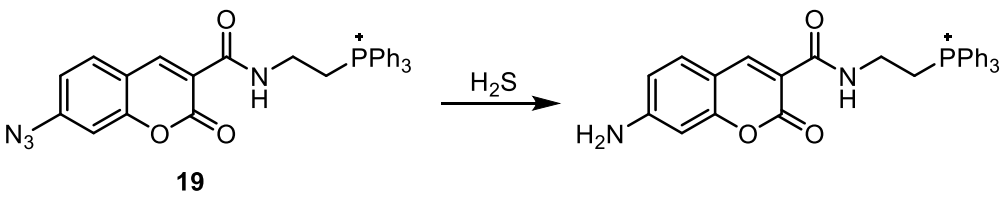

Figure 1.15 Activation of mitochondria targeted coumarin with H_2S.

Recent studies in the literature bring a better understanding of cancer biology, new small molecules and metals related to cancer cells were revealed. These studies contribute the development of activatable PDT agents in the desired region. One of cancer related analyte is the hydrogen sulfide (H_2S) molecule. It has been shown that cystathionine-β-cyntase enzyme and H_2S are high in colon and ovarian cancers and contribute to tumor growth.[107] In line with this discovery, H_2S is very suitable for the activation of PDT agents and based on our knowledge no H_2S activatable PDT agent introduced yet. Instead, several H_2S sensing fluorescent designs are published. These studies also can guide development of H_2S selective PDT agents as masking strategy is similar for PDT agents.

The most successful method of sensing intracellular hydrogen sulfide as fluorescence is the selective conversion of the azido group into amine in the presence of H_2S and the change of the photophysical properties of imaging agents following this reduction reaction.[108] In a study published in 2017, in which this method was applied, the fluorophore of the coumarin (**19)** was modified with azido and mitochondrial-guided triphenylphosphine groups (Figure 1.15).[109] The fact that hydrogen sulfide is overexpressed in the mitochondria of cancerous cells has allowed the reduction reaction to occur selectively in cancerous cells and fluorescence increase with shift in absorption wavelength. In the imaging performed with the confocal microscope **(19),** no emission increase was detected when incubated with healthy cells.

As seen in the aforementioned examples, the studies uncovering the cancer biology should be analyzed well and integrated into PDT applications in order to obtain PDT agents with improved properties and spread their use in clinical applications. On the other hand, it is very important that the PSs have ideal properties for biological studies so development of new skeletal structures that can be effective in PDT action is necessary.

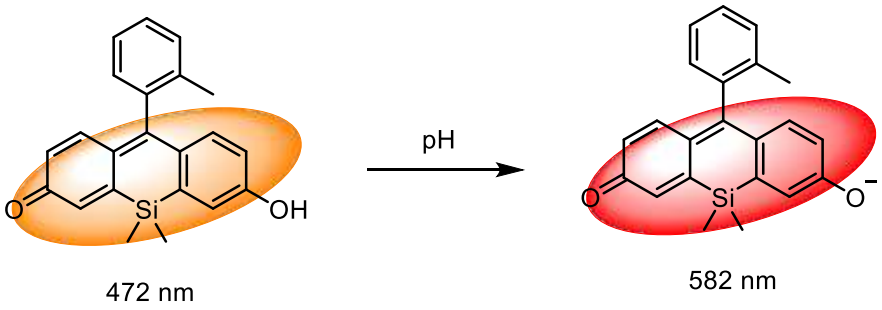

Figure 1.16 Change of structure and absorbance wavelength of TM with pH.

2-Me-TM was discovered to show a pH dependent change in the absorption and emission as summarized in table 3.3 (Figure 1.16). **2-Me-TM** possesses blue shifted broad absorption peak at 472 nm in acidic solutions with comparably small extinction coefficient and red shifted sharp absorption peak at 582 nm in basic solutions with high extinction coefficient. That is, deprotonation of the hydroxyl group on **2-Me-TM** yields 110 nm red-shift of the absorbance. This red shift is larger than that of fluorescein derivative **2-Me-TG** with oxygen instead of silicon. Deprotonation of the hydroxyl group on **2-Me-TG** yields 52 nm red-shift of the absorbance. It can be considered that this larger red shift in **2-Me-TM** is because of difference in the strength of the s*–p* conjugation

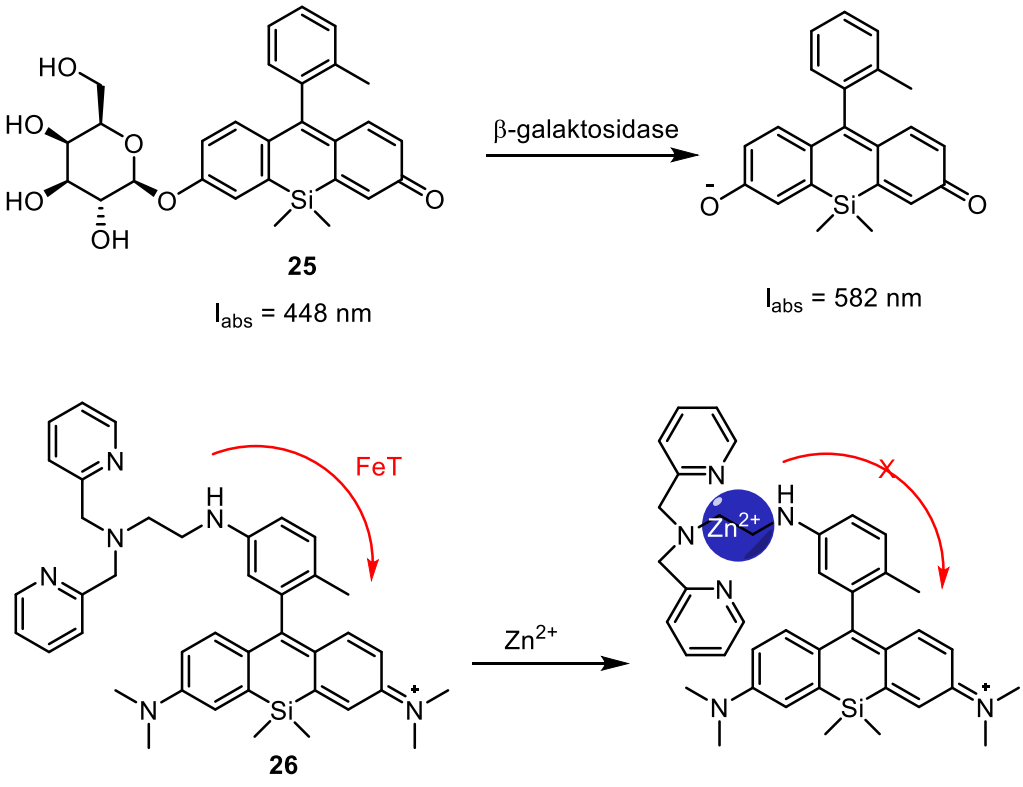

Figure 1.17 Activatable fluorescent probes based on Si-xanthene.

between the neutral form and the anion form like in case of Si-containing pyronine. It was reported by Nagano group that 78% of **2-Me-TM** is in anionic form pH with strong absorption in red region at physiological. This makes **2-Me-TM** an efficient fluorescence sensor probe with a high off/on ratio by utilizing the large redshift only so there is no need for additional strategy such as PeT or spiro cyclization. Herein, utilization of red shift can be easily performed by modifying the phenol in the structure a masking group that will leave **2-Me-TM-O**$^-$ after cleaved with certain analyte. This method widely employed with several derivatives of **TM** to obtain highly selective fluorescent probes (Figure 1.16).

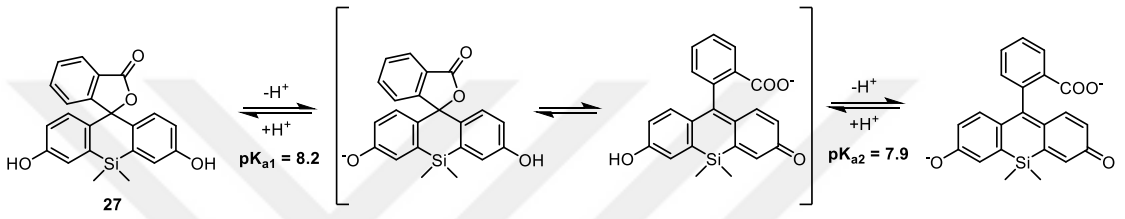

Figure 1.18 Structural changes in silicon substituted fluorescein (SF) with pH.

Spirolactone formation occurs when *ortho*-methyl in TM structure replaced with carboxylic acid (silicon-fluorescein, SF, **27**) (Figure1.18). pH titration with this molecule yields two different forms as spirolactone and dianion. When the hydroxyl group deprotonated in basic pH values dianion is obtained. However, pH values of spirolactone opening were higher than 7.4 and lactone was closed in the physiological environment and prefer to remain in lactone form (Figure 1.18).[110] This prevents fluorophore from being used as a fluorescent agent in pH 7.4 by as it is colorless and emission-free. Also, a study by the Nagano group showed that chlorine or fluorine atoms added to the skeletal structure adjust both pKa values below 7.4, making fluorophore **(28)** suitable for live cell imaging studies (Figure 1.19). Additionally, the addition of chlorine shifts the absorption maximum of fluorophore to 591 nm. A fluorophore activatable with β-galactosidase enzyme was also introduced by Hirabayashi *et al.* as a fluorescent agent activated in the presence of β-galactosidase enzyme.[110]

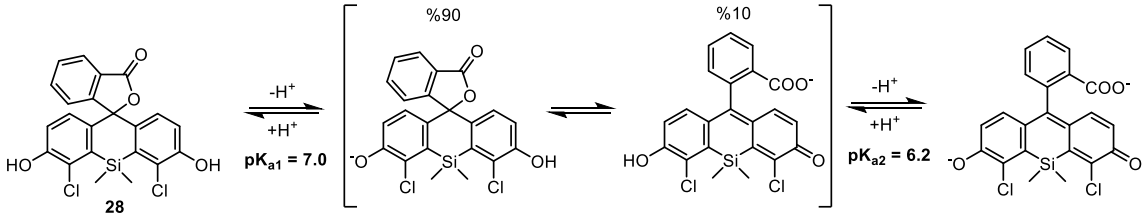

Figure 1.19 Structural changes in chlorinated silicon substituted fluorescein (SF) with pH.

Silicon-substituted xanthene derivatives shows impressive photophysical properties and chemical properties for biological applications and have great potential to be converted into PDT agents. So far there is no Silicon-xanthene derivative was investigated for phototherapeutic applications despite these promising properties. Herein, we put effort to convert SF to an effective PDT agent by modifying structure with iodine (Figure 1.20).[111] Halogenation of the structure will also adjust pKa to be in emissive dianion form at physiological pH and push the intersystem crossing to generate singlet oxygen.

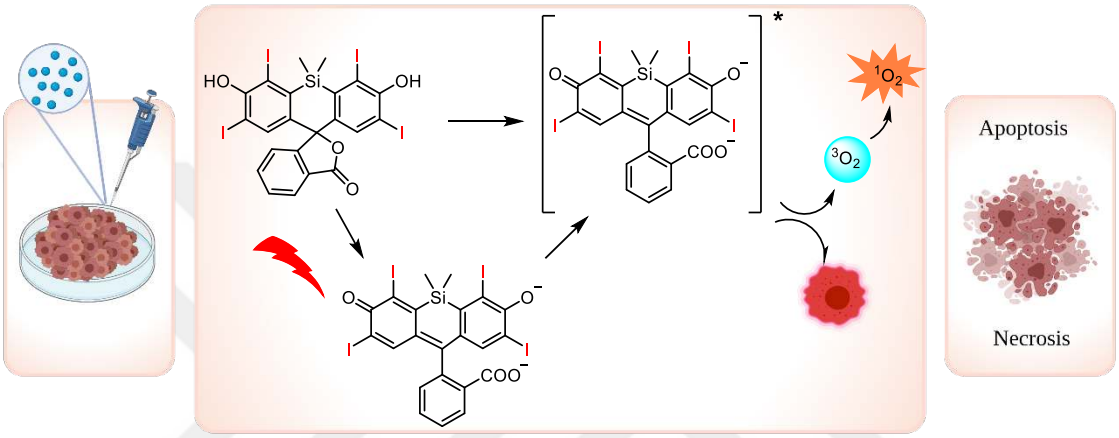

Figure 1.20 Action of SF-I as PDT agent.

As explained **TM** is another fluorescent probe with appealing properties and hold potential to be a PDT agent. Additionally, it is possible to adapt this method to develop selective PDT agent based on **TM** by using a masking group selective to the analyte which is overexpressed in cancer cells. First, TM itself does not expected to have high triplet quantum yield as there is nothing in the structure that can push intersystem crossing like heavy atom. Therefore, addition of a heavy atom (iodine) to the TM structure may result high triplet quantum yield and ability to produce singlet oxygen with photodynamic effect. Also, with this method it is not expected to lose fluorescent ability completely although ISC and fluorescent are two competing pathways. In addition, the choice of masking group should be guided by cancer cell research. As explained above there are vast of research showing overexpression of hydrogen sulfide in several cancerous cells. Therefore, a cage group known to responsive to H_2S can be applied to increase cancer cell selectivity of agent. As explained activatable PSs part several masking modalities have been studied so far. Using the reduction of azide group by reacting with H_2S is the mostly employed method. In a nutshell, in this project aim is to obtain H_2S activatable

TM based phototheranostic agent. azide containing H_2S responsive group was attached to TM core and iodinated (Figure 1.21).

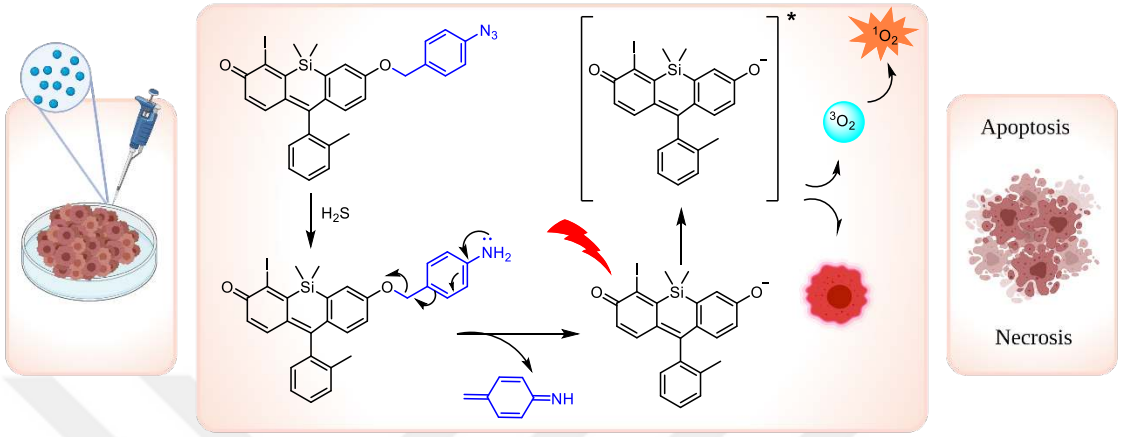

Figure 1.21 Design and activation of TM-I-H_2S with H_2S.

Chapter 2:

MATERIALS AND METHODS

2.1 Materials and Instruments

All reagents were commercially available and used without further purification unless otherwise noted. All dry solvents used in reactions were directly obtained from the Mbraun MBSPS5 solvent drying system. The inert atmosphere was obtained by argon. The ^{1}H and ^{13}C-NMR spectra were recorded on a Varian (500 MHz) or Bruker Avance III Ultrashield (400 MHz) spectrometers using $CDCl_3$ and d_6-DMSO as the solvents. The chemical shifts are reported in parts per million (ppm) downfield from an internal TMS (trimethylsilane) reference. Coupling constants (*J*) are reported in hertz (Hz), and the spin multiplicities were specified by the following symbols: s (singlet), d (doublet), t (triplet), and m (multiplet). NMR spectra were processed with MestReNova program. Column chromatography was performed by using thick-walled glass columns and silica Gel 60 (Merck 230-400 mesh). Thin layer chromatography (TLC Merck Silica Gel 60 F254) was performed by using commercially prepared 0.25 mm silica gel plates and visualization was provided by UV lamp. The relative proportions of solvents in chromatography solvent mixtures refer to the volume: volume ratio. Electronic absorption spectra in solution were acquired using a Shimadzu Uv-3600 UV-Vis-NIR spectrophotometer. Fluorescence spectra were determined on Agilent Cary Eclipse fluorescence spectrophotometer. Fluorescence quantum yields of the samples were investigated by using a fluorescence spectrometer (FLS 1000, Edinburgh Instruments) with an integrating sphere accessory. Mass spectra were recorded on Waters Synapt G1 High-Definition mass spectrometer. Roswell Park Memorial Institute 1640 (RPMI 1640), Dulbecco's Modified Eagle Medium (DMEM), Minimum Essential Medium (MEM), trypsin EDTA, and penicillin streptomycin were obtained from Multicell, Wisent Inc. (QC, Canada). Fetal bovine serum (FBS) was provided by Capricorn Scientific GmbH (Ebsdorfergrund, Germany). Phosphate-buffered saline (PBS) tablets and thiazolyl blue tetrazolium bromide (MTT) were obtained from Biomatik Corp. (ON, Canada). The Live/Dead Viability/Cytotoxicity Kit was purchased from ThermoFisher Scientific (USA). Annexin

V-FITC early apoptosis detection kit was observed from Cell signaling technology (UK). 96-well plates were purchased from Nest Biotechnology Co., Ltd (Wuxi, China).

2.2 Syntheses

2.2.1 Synthesis of Photosensitizer Core

*Synthesis of **1***

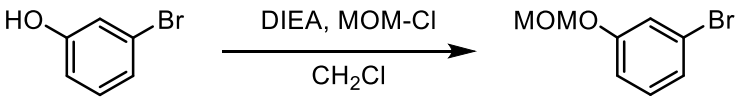

1

3-Bromophenol (10.0 g, 57.8 mmol) and DIEA (12.2 mL, 86.7 mmol) were mixed in DCM (130 mL) and cooled to 0 °C. Chloromethyl methyl ether (5.70 mL, 75.1 mmol) was added dropwise to this solution at 0°C. Then, the reaction solution was warmed to room temperature and left to be stirred for 4 hours. The reaction was monitored with TLC. Upon completion, the reaction mixture was diluted with DCM (50 mL) and washed with water. The collected organic phase was dried with Na_2SO_4 and concentrated in vacuo. The compound 1 was obtained through purification with column chromatography (Hexane) as colorless viscous liquid (11.2 g, 89% yield). ^{1}H NMR (500 MHz, $CDCl_3$) δ 7.28 – 7.24 (m, 1H), 7.19 – 7.12 (m, 2H), 7.03 – 6.97 (m, 1H), 5.16 (s, 2H), 3.48 (d, J = 0.7 Hz, 3H); ^{13}C NMR (126 MHz, $CDCl_3$): δ 158.1, 130.6, 125.0, 122.7, 119.6, 115.1, 94.4, 77.4, 77.2, 76.9, 56.1.

*Synthesis of **2***

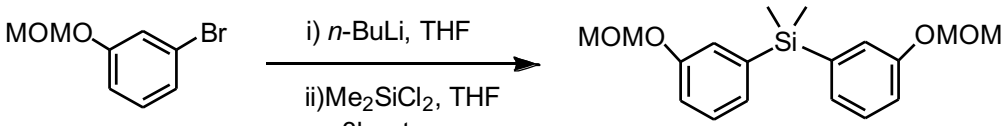

2

Compound **1** (3.00 g, 13.8 mmol) was dissolved in anhydrous THF (30 mL) under argon atmosphere and cooled to -78°C. *n*-BuLi (2.50 M hexane, 5.50 mL, 13.8 mmol) was added to this solution. The reaction mixture was stirred at -78 °C for 30 minutes. Dichlorodimethylsilane (0.60 mL, 5.80 mmol) dissolved in anhydrous THF (2.40 mL) and added to the reaction mixture at -78°C. Then, the solution was warmed to room temperature and stirred for 3 hours. Reaction was monitored with TLC. Upon completion, the reaction mixture was washed with saturated NH_4Cl solution, and extracted with

EtOAc. The collected organic phase was washed with brine and dried with Na_2SO_4. The compound **2** was obtained through colon chromatography (Hexane:EtOAc 4:1) as yellow liquid (1.28g, 56% yield) ^{1}H NMR (500 MHz, $CDCl_3$) δ 7.35 (dd, *J* = 8.2, 7.2 Hz, 2H), 7.28 – 7.20 (m, 4H), 7.13 (ddd, *J* = 8.2, 2.6, 1.1 Hz, 2H), 5.22 (s, 4H), 3.53 (s, 6H), 0.62 (s, 6H); ^{13}C NMR (126 MHz, $CDCl_3$) δ 156.9, 139.9, 129.1, 127.7, 125.0, 122.2, 116.7, 94.6, 77.4, 77.1, 76.9, 56.0, -2.2, -2.4, -2.6.

*Synthesis of **3***

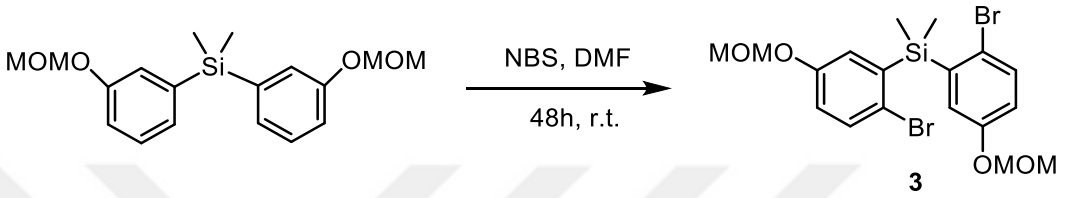

3

Compound **2** (0.190 g, 0.600 mmol) was dissolved in DMF (4 mL) and *N*-bromosuccinimide (0.203 g, 1.10 mmol) was added slowly. The reaction was stirred at room temperature for 48 hours. Reaction was monitored with TLC. Upon completion, reaction mixture was diluted with EtOAc (50 mL) and washed with water (5 x 10 mL). The collected organic phase was dried over Na_2SO_4 and concentrated *in vacuo*. The compound **3** was obtained through column chromatography (Hexane:EtOAc 3:1) as light yellow solid (0.260 g, 93% yield). ^{1}H NMR (500 MHz, $CDCl_3$) δ 7.42 (d, *J* = 8.7 Hz, 2H), 7.14 (d, *J* = 3.0 Hz, 2H), 6.95 (dd, *J* = 8.7, 3.1 Hz, 2H), 5.13 (s, 4H), 3.46 (s, 6H), 0.75 (s, 6H); ^{13}C NMR (126 MHz, $CDCl_3$) δ 155.9, 140.1, 136.8, 133.7, 133.5, 125.7, 124.2, 122.0, 118.7, 118.4, 94.7, 77.3, 77.0, 76.7, 56.0, 2.8, 1.0, -1.3.

*Synthesis of **4***

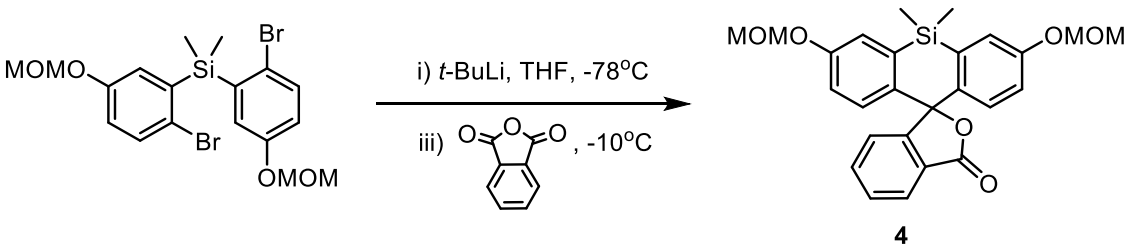

4

Compound **3** (0.200 g, 0.408 mmol) dissolved in anhydrous THF (5 mL) under argon atmosphere and cooled to -78 °C. *t*-BuLi (1.70 M in hexane, 1.06 mL, 1.79 mmol) was added to the solution and warmed to -10°C after stirring for 30 minutes at -78 °C. Phthalic anhydride (0.133 g, 0.897 mmol) was added in THF (10 mL) dropwise within 30 minutes. The reaction mixture was warmed to room temperature and stirred overnight. The reaction was monitored with TLC. Upon completion, the saturated NH_4Cl solution was added to

the solution, and extracted with EtOAc. The collected organic phase washed with $NaHCO_3$ and dried with Na_2SO_4.The product was obtained through column chromotography (Hexane:EtOAc 2:1) as yellow solid (0.0380 g, 20% yield). ^{1}H NMR (500 MHz, $CDCl_3$) δ 7.99 (dt, *J* = 7.7, 1.0 Hz, 1H), 7.68 (td, *J* = 7.5, 1.2 Hz, 1H), 7.58 (td, *J* = 7.5, 0.9 Hz, 1H), 7.34 – 7.32 (m, 3H), 6.95 – 6.89 (m, 4H), 5.19 – 5.16 (m, 4H), 3.47 (s, 6H), 0.65 (d, *J* = 15.6 Hz, 6H); 13C NMR (126 MHz, $CDCl_3$) δ

Synthesis of ***SF***

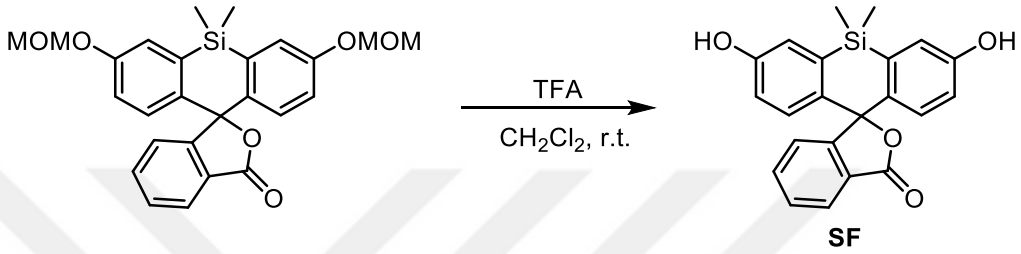

SF

Compound **4** (0.040 g, 0.050 mmol) DCM (5 mL) and added trifluoro acetic acid (2 mL) to the solution. The reaction mixture was stirred at room temperature for 2 days and monitored by TLC. Upon completion, toluene (20 mL) was added from the TFA environment contained in the reaction mixture and the solution concentrated *in vacuo*. **SF** was obtained through colon chromatography (Hexane:EtOAc 2:1) as orange solid (0.031 g, 96% yield).^{1}H NMR (500 MHz, $CDCl_3$) δ 7.99 (dt, *J* = 7.7, 1.0 Hz, 1H), 7.68 (td, *J* = 7.5, 1.2 Hz, 1H), 7.57 (td, *J* = 7.5, 0.9 Hz, 1H), 7.30 (dt, *J* = 7.8, 0.9 Hz, 1H), 7.13 (d, *J* = 2.8 Hz, 2H), 6.80 (d, *J* = 8.7 Hz, 2H), 6.66 (dd, *J* = 8.7, 2.8 Hz, 2H), 5.73 (s, 2H), 0.55 (s, 3H), 0.53 (s, 3H); ^{13}C NMR (126 MHz, $CDCl_3$) δ 171.50, 155.57, 154.21, 137.96, 135.89, 134.35, 129.24, 128.75, 126.24, 126.09, 124.59, 120.45, 116.83, 91.55, 0.00, -1.60.

Synthesis of ***SF-I***

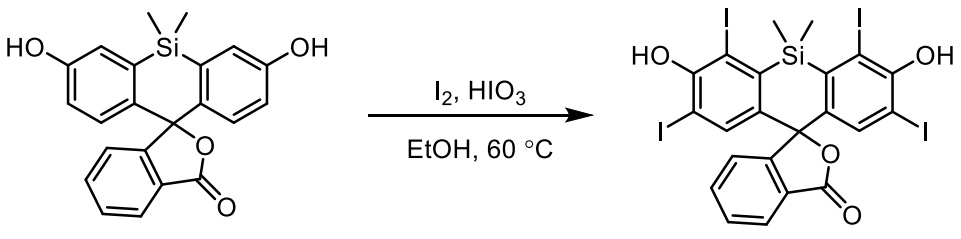

SF-I

Compound **5** (0.020 g, 0.027 mmol) and iodine (0.015 mg, 0.059 mmol) dissolved in ethanol (20 mL) and heated to 60 °C. Then, HIO_3 (0.010 mg, 0.027 mmol) was slowly added, and the reaction was stirred at 60 °C for 3 hours. The reaction was monitored by

TLC. Upon completion, the reaction mixture was concentrated *in vacuo*. Saturated sodium thiosulfate solution was added, and it was extracted with ethyl acetate. Compound **6** was obtained through column chromatography (Hexane:EtoAc 2:1) as sticky yellow solid (0.020 g, 42% yield). ^{1}H NMR (500 MHz, $CDCl_3$) δ 7.94 (d, *J* = 7.6 Hz, 1H), 7.60 (s, 2H), 7.55 – 7.51 (m, 1H), 7.48 – 7.45 (m, 1H), 7.00 (dt, *J* = 7.8, 0.9 Hz, 1H), 6.05 (s, 2H), 1.23 (s, 3H), 1.01 (s, 3H); ^{13}C NMR (126 MHz, $CDCl_3$) δ 170.4, 156.4, 153.1, 141.5, 139.0, 136.7, 135.2, 129.31, 126.7, 122.3, 122.1, 92.6, 87.8, 85.0, 77.3, 77.0, 76.8, 31.6, 29.7, 1.3, 1.0. HR-MS m/z calculated $C_{22}H_{14}I_4O_4Si$: 877.6840 $[M+H]^+$; found: 878.6923.

Synthesis of ***5***

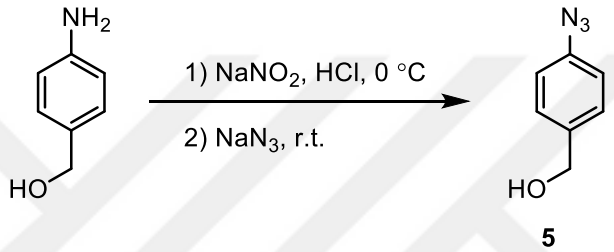

5

4-aminobenzyl alcohol (1.00 g, 8.12 mmol) was dissolved in HCl (5 mL, 5 M) and $NaNO_2$ (0.840 g, 12.1 mmol) was added to the solution. The resulting mixture was stirred vigorously at 0 °C. Then, NaN_3 (2.10 g, 32.3 mmol) was added to the reaction mixture. This mixture was stirred overnight at room temperature. Reaction was monitored by TLC. Upon completion, the mixture was poured in to the saturated $NaHCO_3$ solution. It was washed with ethyl acetate (2 x 50 mL). The organic phase washed with saturated brine. The collected organic phase was dried over Na_2SO_4 and concentrated *in vacum*. Compound **5** was obtained through colon chromatography (EtOAc:Hex 1:3) as yellow solid (1.17 g, 97% yield). ^{1}H NMR (500 MHz, $CDCl_3$) δ 7.31 – 7.28 (m, 2H), 6.99 – 6.97 (m, 2H), 4.58 (s, 2H), 2.86 (s, 1H); ^{13}C NMR (500 MHz, $CDCl_3$) δ 139.4, 137.6, 128.5, 119.1, 64.6.

Synthesis of ***6***

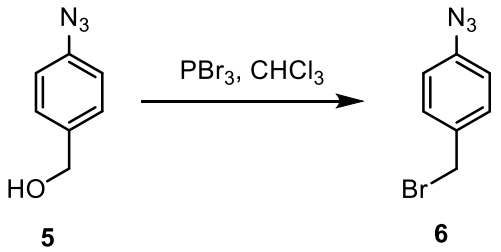

5 **6**

Compound **6** (0.322 g, 2.16 mmol) was dissolved in chloroform (20 mL) under the argon atmosphere and PBr_3 (0.800 g, 2.90 mmol) was added dropwise at room temperature. The reaction mixture was stirred overnight at room temperature and monitored by TLC. Upon completion, the reaction mixture was washed with saturated $NaHCO_3$ solution. The collected organic phase was dried over Na_2SO_4 and concentrated *in vacuo*. Compound **6** was obtained without purification as yellow solid (0.380 g, 83% yield). ^{1}H NMR (500 MHz, $CDCl_3$) δ 7.25 (d, J = 8.4 Hz, 2H), 6.93 (d, J = 8.4 Hz, 2H), 4.56 (s, 2H); ^{13}C NMR (126 MHz, $CDCl_3$) δ 139.2, 133.5, 129.6, 118.4, 31.9.

Synthesis of ***7***

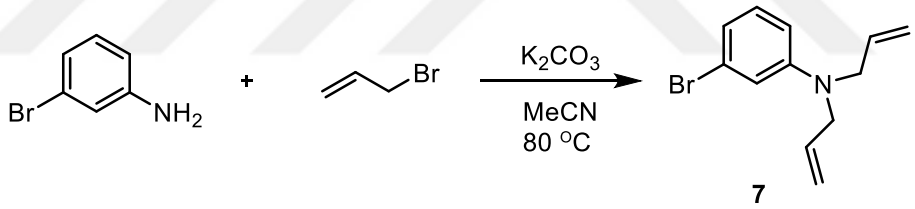

7

3-bromoaniline (13.00 g, 112.6 mmol) was dissolved in MeCN (37 mL) and K_2CO_3 (33.00 g, 18.60 mmol) and allyl bromide (35 mL, 21.80 mmol) was added to the solution. The reaction mixture was heated to 80°C and stirred at this temperature for 3 hours. The reaction was monitored by TLC. Upon completion, the mixture was cooled to room temperature and diluted with ethyl acetate (50 mL); followingly, washed with water (3 x 50 mL). After cooling to room temperature, the mixture was filtered through Celite, washed with EtOAc and solvent was evaporated. Purification by silica gel column chromatography (Hexane:EtOAc 30:1) yielded **7** as a thick yellow liquid (25.70 g, 85% yield). ^{1}H NMR (400 MHz, CDCl3): δ 7.10 (t, J = 8.1 Hz, 1H), 6.98 – 6.78 (m, 2H), 6.68 (dd, J = 8.5, 2.5 Hz, 1H), 5.95 – 5.86 (m, 2H), 5.27 – 5.25 (m, 2H), 5.24 – 5.22 (m, 2H), 3.98 – 3.96 (m, 4H). ^{13}C NMR (100 MHz, CDCl3): δ 149.9, 133.2, 130.3, 123.4, 119.1, 116.4, 115.0, 110.9, 52.8.

Synthesis of ***8***

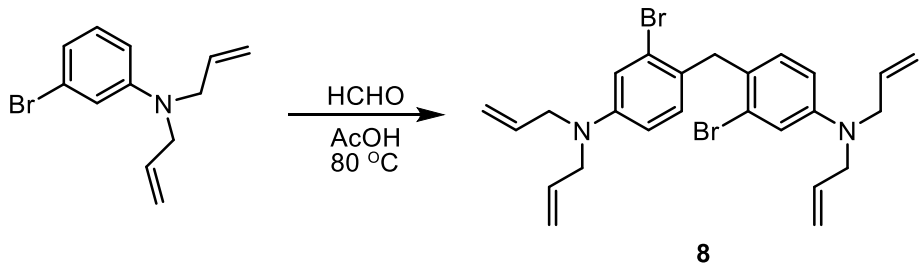

8

N, *N*-diallyl-3-bromoaniline (25.7 g, 102.0 mmol) dissolved in AcOH (120 mL) and formaldehyde (37%, 15.3 g, 511.0 mmol) was added to the solution. The reaction mixture was heated to 80°C and stirred at this temperature for 2 hours. The reaction was monitored by TLC. Upon completion, it was then cooled to room temperature and neutralized with saturated $NaHCO_3$ and saturated NaOH solutions. The resulting mixture was extracted with $CHCl_3$. The collected organic phase was dried with Na_2SO_4 and concentrated under low pressure. Purification by silica gel column chromatography (1:30 EtOAc: Hexane) yielded **9** as a thick yellow liquid (22.8 g, 87% yield). ^{1}H NMR (400 MHz, $CDCl_3$): δ 6.98 (d, *J* = 2.7 Hz, 2H), 6.89 (d, *J* = 8.6 Hz, 2H), 6.62 (dd, *J* = 8.6, 2.7 Hz, 2H), 5.96 – 5.82 (m, 4H), 5.36 – 4.92 (m, 8H), 4.04 (s, 2H), 3.96 – 3.92 (m, 8H). ^{13}C NMR (100 MHz, $CDCl_3$): δ 148.2, 133.5, 130.8, 127.0, 125.6, 116.3, 116.0, 111.7, 52.8, 39.8, 31.7, 22.7, 14.2.

Synthesis of ***9***

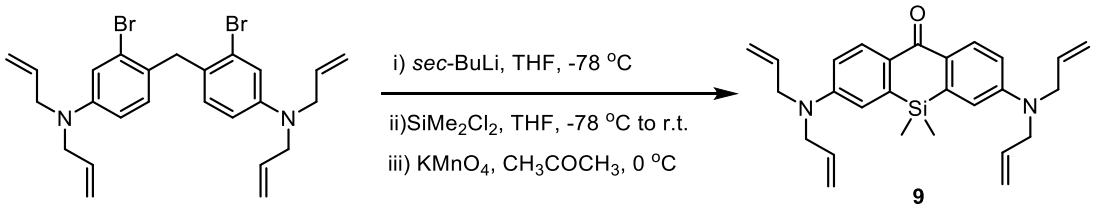

9

Compound **8** (7.3g, 14.1 mmol) and anhydrous THF (50 mL) were added. The mixture was cooled to -78ºC and *sec*-BuLi, 1.4 M in cyclohexane, (26 mL, 36.7 mmol) was added slowly. The reaction mixture stirred for 30 min, then $SiMe_2Cl_2$ (3.0 mL, 25.4 mmol) in 15 mL anhydrous THF was added at the same conditions. The mixture was warmed to room temperature and stirred for 1 h. The reaction was quenched with 2 N HCl, then neutralized with $NaHCO_3$ and extracted with CH_2Cl_2. The organic layer was washed with brine, dried over Na_2SO_4 and solvent was evaporated. Remaining residue

was kept under high vacuum for 2 hours. Without any further purification, the residue was dissolved in acetone (150 mL) and the solution was cooled to 0°C. To this solution of $KMnO_4$ (6.1g, 38.5 mmol) was added in small portions within 2 h. The reaction mixture was stirred for another 1 h at the same temperature, after that diluted with CH_2Cl_2 (200 mL). The mixture was filtered through Celite, and solvent was removed. Purification by silica gel column chromatography (CH_2Cl_2) gave **3** as a yellow solid (800 mg, 20% yield). ^{1}H NMR (400 MHz, $CDCl_3$): δ 8.36 (d, *J* = 8.6 Hz, 2H), 6.84 – 6.81 (m, 4H), 5.93 – 5.86 (m, 4H), 5.23 – 5.19 (m, 8H), 4.03 (d, *J* = 4.7 Hz, 8H), 0.43 (s, 6H). ^{13}C NMR (100 MHz, $CDCl_3$): δ 185.0, 150.0, 140.3, 132.9, 131.6, 129.8, 116.5, 114.7, 113.3, 52.6, -1.2.

*Synthesis of **10***

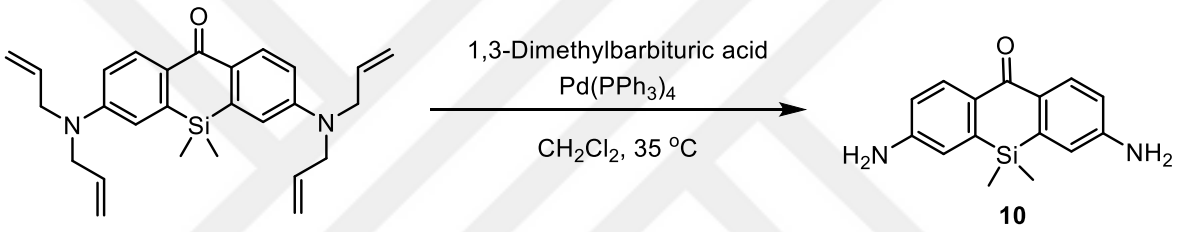

10

$Pd(PPh_3)_4$ (322 mg, 0.28 mmol) and 1,3-dimethylbarbituric acid (1.35 g, 8.6 mmol) were put in to a flame-dried round bottom flask and filled with N_2. Compound **9** (800 mg, 1.86 mmol) in dry CH_2Cl_2 (40 mL) was added to the mixture and the solution was stirred at 35°C for 16 h, which was then poured into satd. Na_2CO_3 aq. and extracted with EtOAc. The organic layer was washed with brine, dried over Na_2SO_4 and solvent was evaporated. Purification by silica gel column chromatography (1:1 EtOAc: Hexane) yielded **10** as a yellow-orange solid (400 mg, 75% yield). ^{1}H NMR (400 MHz, MeOD): δ 8.14 (d, *J* = 8.7 Hz, 2H), 6.89 (d, *J* = 1.9 Hz, 2H), 6.77 (dd, *J* = 8.3, 2.2 Hz, 2H), 0.42 (s, 6H).

*Synthesis of **11***

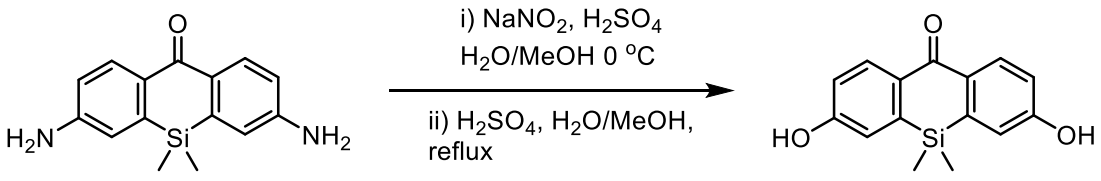

10 **11**

A solution of compound **10** (400 mg, 1.48 mmol) in 150 mL MeOH / 6N H_2SO_4 was cooled to 0ºC. A solution of $NaNO_2$ (634 mg, 9.47 mmol) in 10 mL H_2O was slowly added and the mixture is stirred for 1 h at the same temperature. The reaction mixture slowly added into boiling 120 mL of H_2SO_4. The resulting mixture was refluxed for another 10 min, and then allowed to cool to room temperature. After that the mixture was extracted with CH_2Cl_2. The organic layer was washed with brine, dried over Na_2SO_4 and solvent was evaporated. Purification by silica gel column chromatography (1:20 MeOH: CH_2Cl_2) yielded **11** as a white solid (160 mg, 40% yield). ^{1}H NMR (500 MHz, $CDCl_3$) δ 8.44 (dd, *J* = 28.3, 8.8 Hz, 2H), 7.12 (dd, *J* = 9.5, 2.7 Hz, 2H), 7.07 (td, *J* = 8.9, 2.7 Hz, 2H), 3.92 (s, 2H), 0.46 (s, *J* = 3.4 Hz, 6H).

*Synthesis of **12***

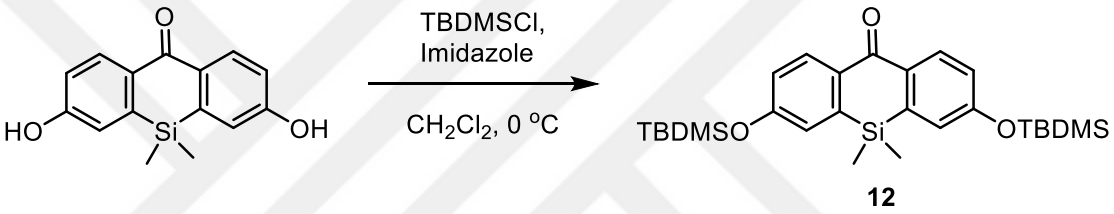

12

Compound **11** (0.0330 g, 0.122 mmol) and imidazole (0.0850 g, 1.26 mmol) dissolved in DCM (20 mL) and TBDMS-Cl (0.185 g, 1.23 mmol) in DCM (5mL) was slowly added to this mixture. Reaction mixture was stirred for 14 hours and monitored by TLC. Upon completion, reaction mixture was diluted with DCM (50 mL) and washed with water (3 x 50 mL). The collected organic phase was washed with brine, and after drying over with Na_2SO_4, and the reaction mixture was concentrated *in vacuo*. Compound **12** was obtained through colon chromatography (Hexane:EtOAc 20:1) as obtained (50.0 mg, 85% efficiency). ^{1}H NMR (500 MHz, $CDCl_3$) δ 8.38 (d, *J* = 8.7 Hz, 2H), 7.06 (d, *J* = 2.6 Hz, 2H), 7.00 (dd, *J* = 8.7, 2.6 Hz, 2H), 1.03 (s, 18H), 0.47 (s, 6H), 0.28 (s, 12H). ^{13}C NMR (126 MHz, $CDCl_3$) δ 186.0, 158.7, 141.2, 134.6, 132.3, 123.7, 121.8, 77.3, 77.0, 76.8, 25.7, 18.3, -1.5, -4.3.

*Synthesis of **13***

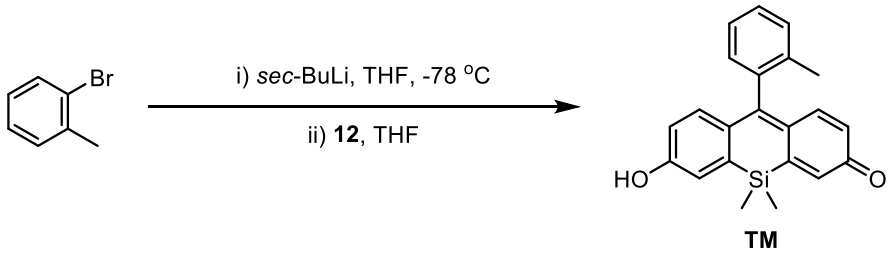

Bromotoluene (0.343 g, 2.01 mmol) dissolved in anhydrous THF (30 mL) and cooled to -78 °C, then *sec*-BuLi (1.60 mL, 1.40 M) dropwise. After stirred at this temperature for 20 minutes, compound **12** (0.200 g, 0.400 mmol) dissolved in anhydrous THF (5 mL) were added. The reaction mixture was stirred at this temperature for 90 minutes and monitored by TLC. Upon completion, the reaction mixture was diluted with DCM (50 mL) and washed with 1 M HCl (12 mL). The collected organic phase was washed with saturated NaCl solution. The obtained organic phase was dried over with Na_2SO_4, it was filtered-off and concentrated *in vacuo*. Compound 12 was obtained through colon chromatography (DCM:MeOH 20:1) as red solid (0.0860 g, 62% yield). ^{1}H NMR (400 MHz, $CDCl_3$) δ 7.38 – 7.34 (m, 1H), 7.29 (d, J = 8.2 Hz, 2H), 7.09 – 7.04 (m, 3H), 6.94 (d, J = 9.4 Hz, 2H), 6.56 (dd, J = 9.4, 2.1 Hz, 2H), 2.03 (s, 3H), 0.43 (s, 3H), 0.41 (s, 3H); ^{13}C NMR (100 MHz, $CDCl_3$) δ 172.6, 161.5, 146.0, 140.5, 139.3, 135.9, 130.2, 129.9, 129.1, 128.5, 125.7, 122.1, 19.6, -1.21, -1.5.

*Synthesis of **TM-H_2S***

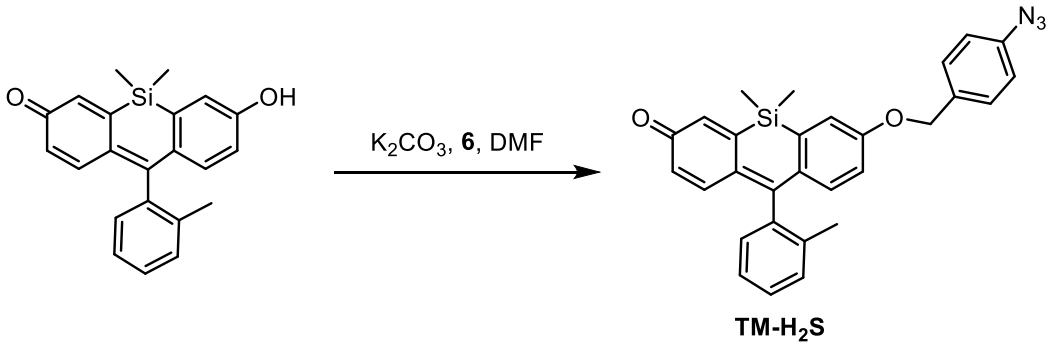

Compound **13** (0.077 g, 0.22 mmol) was dissolved in anhydrous DMF (10 mL) under argon atmosphere and K_2CO_3 was added (0.31 g, 0.45 mmol). After the color change was observed, 1-azido-4-(bromomethyl) benzene (0.0950 g, 2.24 mmol) was added, and the reaction was stirred at room temperature for 1 hour. Reaction was monitored with TLC.

Upon completion, the reaction mixture was filtered-off and concentrated *in vacuo*. Compound **14** was obtained through colon chromatography (DCM:MeOH 50:1) as orange solid (0.090 g 85% yield). ^{1}H NMR (500 MHz, $CDCl_3$) δ 7.41 (d, *J* = 8.4 Hz, 3H), 7.37 (dd, *J* = 7.5, 1.4 Hz, 1H), 7.34 – 7.29 (m, 2H), 7.25 (d, *J* = 2.9 Hz, 1H), 7.10 (dd, *J* = 7.5, 1.4 Hz, 1H), 7.05 (d, *J* = 8.4 Hz, 2H), 6.94 (d, *J* = 10.1 Hz, 1H), 6.86 (d, J = 6.2 Hz, 1H), 6.84 (s, 1H), 6.77 (dd, J = 9.0, 2.8 Hz, 1H), 6.24 (dd, *J* = 10.1, 2.2 Hz, 1H), 5.06 (s, 2H), 2.06 (s, 3H), 0.48 (d, *J* = 8.4 Hz, 6H); ^{13}C NMR (126 MHz, $CDCl_3$) δ 185.6, 160.6, 156.8, 148.1, 142.8, 141.8, 141.4, 140.5, 138.1, 137.2, 136.5, 135.0, 133.8, 131.3, 130.5, 130.4, 129.8, 129.7, 129.4, 128.9, 126.9, 122.8, 120.5, 120.3, 116.2, 70.7, 20.7, 0.0, -0.3. HR-MS m/z calculated $C_{29}H_{25}N_3O_2Si$: 475.1720 $[M+H]^+$; found: 476.1794.

Synthesis of ***TM-I-H$_2$S***

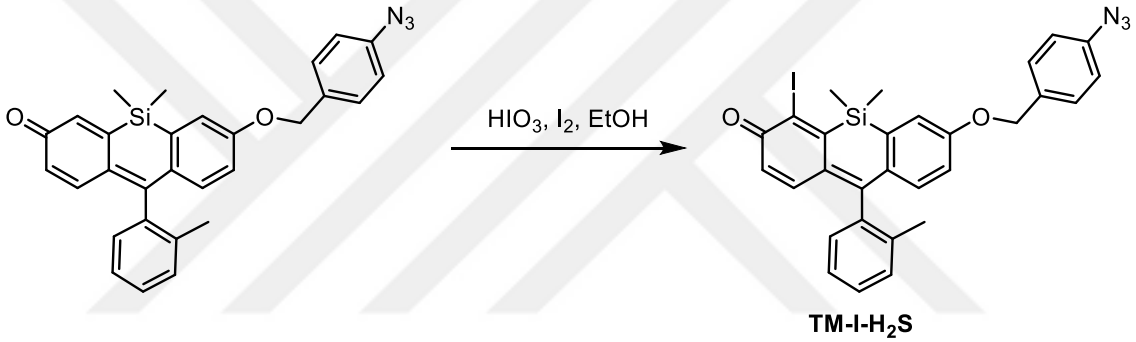

TM-I-H_2S

Compound **14** (0.043 g, 0.090 mmol) and iodine (0.044 g, 0.17 mmol) dissolved in EtOH (5 mL) and heated to 60 °C. HIO_3 (0.026 g, 0.15 mmol) was slowly added, and the reaction mixture was stirred for 2 hours at this temperature. Reaction was monitored by TLC. Upon completion, ethyl alcohol was removed under reduced pressure. The remaining solid was dissolved with ethyl acetate (50 mL) and washed with saturated sodium thiosulfate solution. The collected organic phase was dried over Na_2SO_4 and concentated *in vacuo*. Compound 14 was obtained through colon chromatography (Hexane:EtOAc 2:1) as red solid (0.040 g, 74% yield). ^{1}H NMR (500 MHz, $CDCl_3$) δ 7.36 – 7.32 (m, 2H), 7.31 (dd, *J* = 7.4, 1.4 Hz, 1H), 7.26 – 7.21 (m, 2H), 7.17 (d, *J* = 2.7 Hz, 1H), 7.03 – 7.00 (m, 1H), 7.00 – 6.97 (m, 2H), 6.94 (d, *J* = 9.9 Hz, 1H), 6.73 (d, *J* = 9.0 Hz, 1H), 6.68 (dd, *J* = 9.0, 2.7 Hz, 1H), 6.29 (d, *J* = 9.9 Hz, 1H), 5.00 (s, 2H), 1.98 (d, *J* = 1.4 Hz, 4H), 0.72 (d, *J* = 5.6 Hz, 6H). ^{13}C NMR (126 MHz, $CDCl_3$) δ 208.2, 178.4, 161.2, 158.4, 152.4, 143.7, 143.6, 141.2, 140.7, 136.7, 136.5, 133.8, 133.5, 131.2, 130.94,

130.3, 130.0, 129.4, 126.9, 125.8, 124.7, 122.7, 120.3, 116.13, 70.6, 20.5, 0.0, -0.0. HR-MS m/z calculated $C_{29}H_{25}N_3O_2Si$: 601.0680 $[M+H]^+$; found: 602.0740.

2.3 Photophysical characterization

*2.3.1 Photophysical characterization of **SF-I***

Absorption and Emission characteristics

Emission and absorption spectrum of **SF-I** was measured by preparing the solution of **SF-I** (5 uM) in pH 7.4 PBS puffer by adjusting DMSO amount to 0.5%.

Fluorescence quantum yield

Fluorescence quantum yield of **SF-I** was investigated by using a fluorescence spectrometer (FLS 1000, Edinburgh Instruments) with an integrating sphere accessory. A continuous-wave xenon lamp was used as the excitation source and the emitted fluorescence was detected with a standard photomultiplier (PMT-900) covering a wavelength range of 200-800 nm. During the measurements, the PMT was cooled down to -20 ^{0}C by using a built-in housing to reduce the undesired dark current noise.

For quantum yield measurement, an integrating sphere (Edinburgh Instruments) was placed inside the sample compartment of the spectrometer. Internal cavity of the sphere was coated with a PTFE-like material to enable a reflectance of approximately >99% (>95%) over the wavelength range between 400 and 1500 nm (250 and 2500 nm). The sphere had two ports which were 90^o apart. The excitation beam was sent to the sample through the excitation port and the fluorescence was collected from the emission port. The excitation port of the sphere consisted of a lens to effectively focus the beam on the sample. The emission port was open aperture.

Prior to the experiments performed with the samples, the blank spectrum was measured by using the reference solvent (PBS (pH 7.4, 0.5% DMSO)). For both measurements (blank and sample), two identical quartz cuvettes with equal volumes were used. First, the reference sample was placed inside the sphere and the emission/excitation slits were adjusted at the excitation wavelength so that the response of the PMT remained linear during the measurements. To cover a scattering range, the emission scans were started from 20 nm below the actual excitation wavelengths (594 nm) and finished at 750 nm. Furthermore, the step size and the integration time of the measurements were set to 1 nm

and 0.2 seconds, respectively. After the all the emission measurements of the samples and references were complete, the quantum yields of the samples were determined by using the Fluoracle® software. The built-in analysis tool calculates the quantum yield (QY) as

$$QY = \frac{E_s - E_B}{S_B - S_s}$$

where E_s (E_B) and S_s (S_B) are the selected areas for the emitted and scattered signals of the sample (blank).

pH titration

Dependence of absorption and fluorescence characteristics of **SF-I** to the pH changes in aqueous solution was evaluated by using solutions: (glycine (pH 2.5-3.5), sodium acetate (pH 4.0- 5.5), MES (6.0-6.8), PBS (pH 7.2-8.2) and carbonate (pH 9.2-10.0) in 50 mM concentration). Aqueous solutions with different pH values and **SF-I** with final concentration 5 µM and final DMSO amount %0.5 were prepared. Absorption and emission of these solutions were recorded.

Singlet Oxygen Detection with ADMDA

To evaluate singlet oxygen generation of **SF-1** a water-soluble trap molecule 2,2'-(anthracene-9,10-diyl)bis(methylene)dimalonic acid (ADMDA) was used. As a reference photosensitizer methylene blue (ΦΔ = 0.52 in PBS buffer) was employed to calculate singlet oxygen quantum yield of **SF-I**. Below equation was used for calculation:

$$\Phi_\Delta(\text{PS}) = \Phi_\Delta(\text{ref}) \times \frac{m(PS)}{m(ref)} \times \frac{F(ref)}{F(PS)} \times \frac{PF(ref)}{PF(PS)}$$

PS: **SF-I** ref: methylene blue (MB)

M: slope of absorbance of ADMDA at 380 nm versus time graph,

F: the correction factor: $F = 1 - 10^{-|OD|}$ (OD: irradiation wavelength, 595/630 nm)

PF: absorbed photonic flux in µEinstein $dm^{-3}s^{-1}$.

In our calculation PF was ignored because same light source were used for irradiation of both **SF-I** and MB.

To obtain absorbance of ADMDA at 380 nm versus time graph with 595 nm LED light irradiation, solution of **SF-I** (5 μM) and ADMDA (O.D. = 0.6-1.5) in oxygen bubbled PBS (pH 7.4, 0.5% DMSO) was prepared. First, a few measurements were taken without any light irradiation to show no change in the absorption of ADMDA. Then, the solution was exposed to the LED light (595 nm) for 20 seconds from 10 cm of distance and absorbance recorded. This procedure repeated every 20 seconds and after each

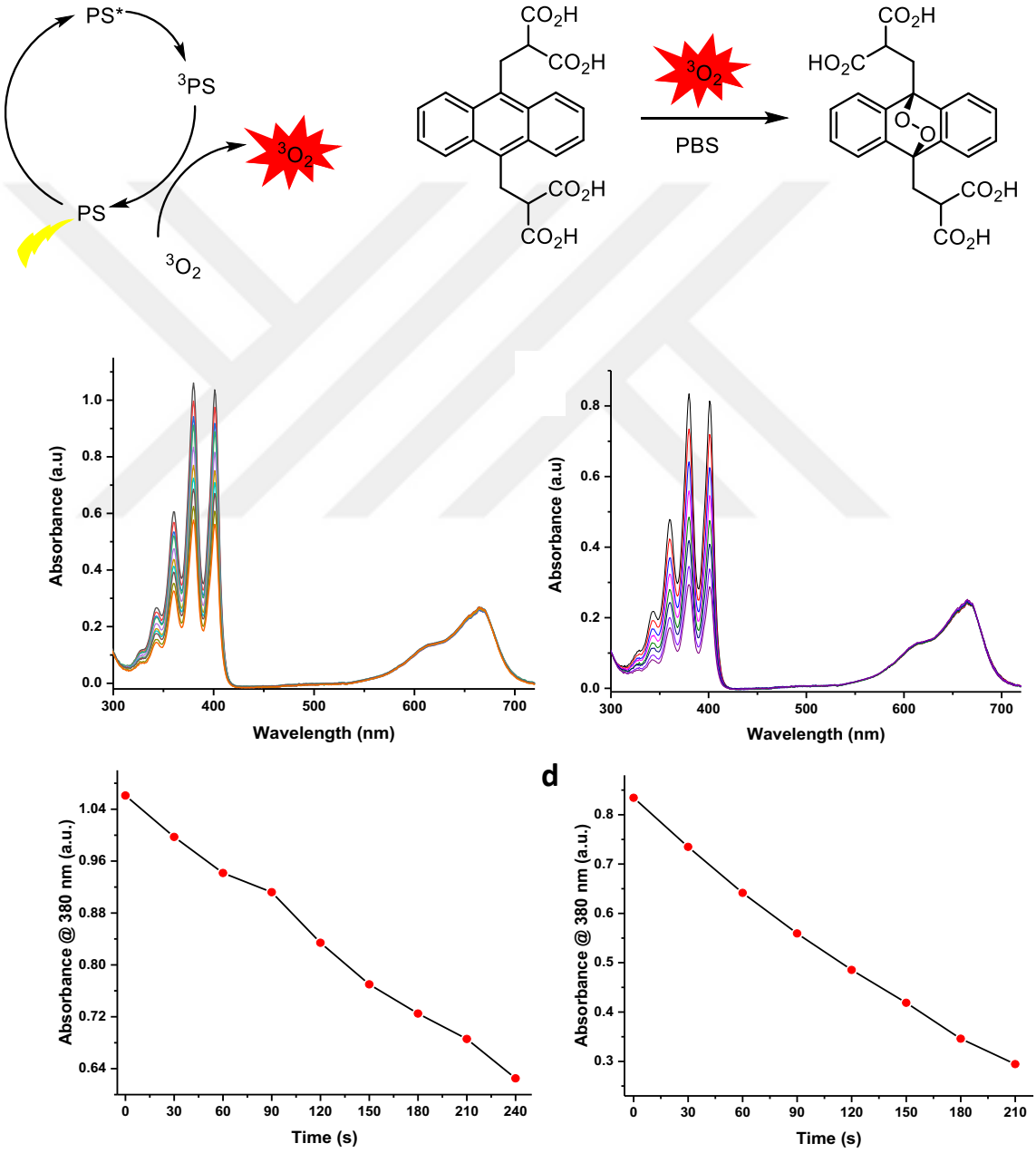

Figure 2.1 Absorption spectra of solution of MB (OD ~ 0.2) in PBS (pH 7.4, 0.5% DMSO) and ADMDA upon irradiation with 595 nm (a) 630 nm (b) LED light. Decrease in the absorption signal of ADMDA upon irradiation with 595 nm (c) 630 nm (d) LED light.

irradiation, absorbance of the ADMDA was recorded. Same procedure was repeated with MB.

To obtain absorbance of ADMDA at 380 nm versus time graph with 630 nm LED light irradiation, same procedure was followed with 30 second time interval and MB under same conditions. For both **SF-I**, and MB, slope of absorbance of ADMDA at 380 nm versus time graph were drawn for both lights.

Singlet Oxygen Detection with SOSG

Another experiment to evaluate singlet oxygen generation was carried by using SOSG (Singlet Oxygen Sensor Green) which shows emission at 530 nm in presence of singlet oxygen. Aqueous solution of 5 µM **SF-I** (pH 7.4, %0.5 DMSO/oxygen bubbled PBS) was added SOSG (5 µM) in MeOH. Several measurements were taken without light irradiation then the solution was irradiated with LEDs (630/595 nm) for 30 seconds. The resulting green emission was recorded at 530 nm wavelength by a spectrofluorometer with excitation wavelength at 504 nm. This procedure is repeated at every 30 seconds. As

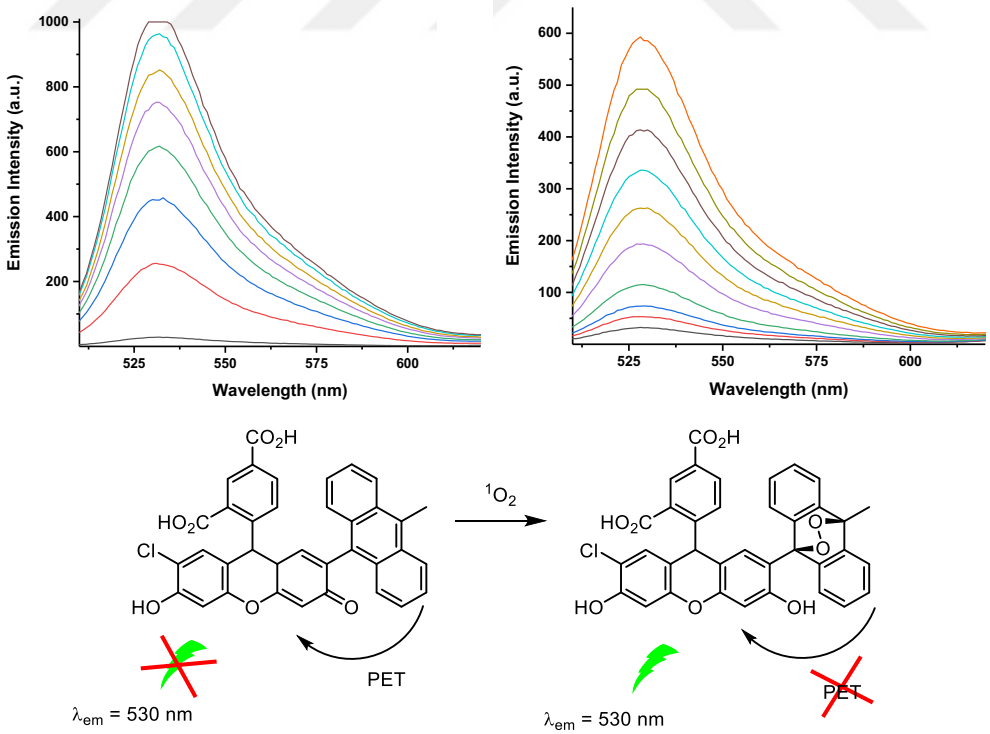

Figure 2.2 Emission spectrum of SOSG after irradiation with 595 nm (a) 630 nm (b) light irradiation in presence of SF-I.

a control for SOSG, blank solution was prepared without **SF-I** and the same experiment was repeated.

*2.3.2 Photophysical characterization of **TM-I-H_2S***

Absorption and Emission characteristics

Emission and absorption spectrum of **TM-I-H_2S** was measured by preparing the solution of **TM-I-H_2S** (10 μ) in pH 7.4 PBS puffer by adjusting DMSO amount to 10% with and without the addition of H_2S (200 μM).

pH Titration

Dependence of absorption and fluorescence characteristics of **TM-I-H_2S** to the pH changes in aqueous solution was evaluated by using solutions: (glycine (pH 2.5-3.5), sodium acetate (pH 4.0- 5.5), MES (6.0-6.8), PBS (pH 7.2-8.2) and carbonate (pH 9.2-10.0) in 50 mM concentration). Aqueous solutions with different pH values and **TM-I-H_2S** with final concentration 10 μM and final DMSO amount 10% were prepared and Na_2S (200 uM, PBS) was added. After standing for 10 minutes, absorption and emission of these solutions were recorded.

Fluorescence quantum yield

Evaluation of fluorescence quantum yield (Φ_f) of **TM-I-H_2S** was done by using Tokyo Magenta (TM) as reference florophore which Φ_f in aqueous solutions was known as 42%.[112] Aqueous solutions of **TM-I-H_2S** and TM was prepared (10 μM TM-I-H_2S/TM, 7.4 PBS, 10% DMSO). Absorption spectrum of TM was measured first to get excitation wavelength where absorption maxima of TM. Emission spectrum of TM was also recorded. Absorption and emission spectrum of **TM-I-H_2S** was measured after the addition of N_2S solution (200 uM, PBS).

Area under the emission spectrum of **TM-I-H_2S** and TM was calculated and placed in below equation to calculate Φ_f. (figure x)

$$\Phi_f(PS) = \Phi_f(ref) \times \frac{A(PS)}{A(ref)} \times \frac{F(ref)}{F(PS)}$$

PS: **TM-I-H_2S** , ref: Tokyo Magenta (TM)

A: area under the emission spectrum,

F: the correction factor: $F = 1 - 10^{-|OD|}$ (OD: absorbance at excitation wavelength (580 nm)

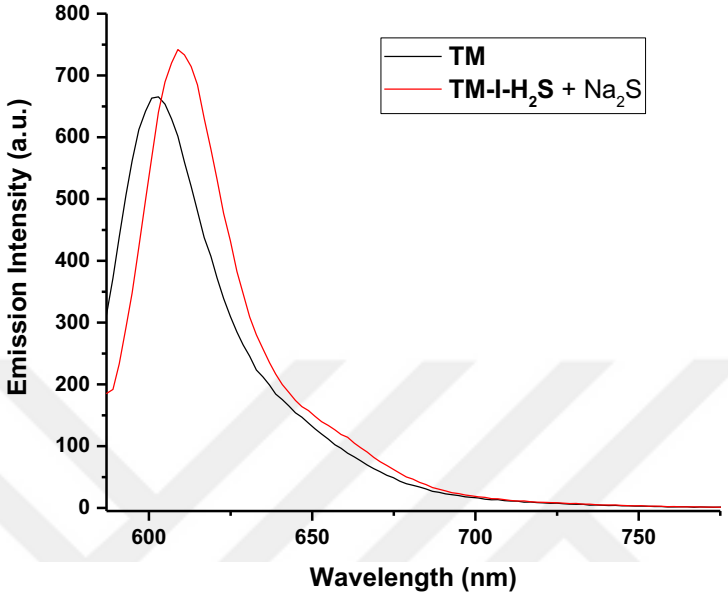

Figure 2.3 Emission spectrum of solutions TM (10 µM, pH 7.4, 10% DMSO), TM-I-H2S + Na2S (10 µM, pH 7.4, 10% DMSO) ex: 582.

Singlet Oxygen Detection

To evaluate singlet oxygen generation of **TM-I-H_2S** a water-soluble trap molecule 2,2'-(anthracene-9,10-diyl)bis(methylene)dimalonic acid (ADMDA) was used. As a reference photosensitizer methylene blue ($\Phi\Delta$ = 0.52 in PBS buffer) was employed to calculate singlet oxygen quantum yield of **TM-I-H_2S** after cleaved with H_2S. Below equation was used for calculation:

$$\Phi_\Delta(PS) = \Phi_\Delta(ref) \times \frac{m(PS)}{m(ref)} \times \frac{F(ref)}{F(PS)} \times \frac{PF(ref)}{PF(PS)}$$

PS: **TM-I-H_2S** ref: methylene blue (**MB**)

M: slope of absorbance of ADMDA at 380 nm versus time graph,

F: the correction factor: $F = 1 - 10^{-|OD|}$ (OD: irradiation wavelength, 595/630 nm)

PF: absorbed photonic flux in µEinstein $dm^{-3}s^{-1}$.

In our calculation PF was ignored because same light source were used for irradiation of both **TM-I-H_2S** and **MB**.

To obtain absorbance of ADMDA at 380 nm versus time graph with 595 nm LED light irradiation, solution of **TM-I-H_2S** (10 µM, 10% DMSO/PBS, oxygen bubled) was prepared and added H_2S (100 µM). After observing full cleavage, ADMDA (O.D. = 0.6-1.5) was added. First, a few measurements were taken without any light irradiation to show no change in the absorption of ADMDA in the dark. Then, the solution was exposed to the LED light (595 nm) for 30 seconds from 10 cm of distance and absorbance recorded. This procedure repeated and after each irradiation, absorbance of the ADMDA was recorded. Same experiment was repeated without addition of H_2S. Same procedure was repeated with MB.

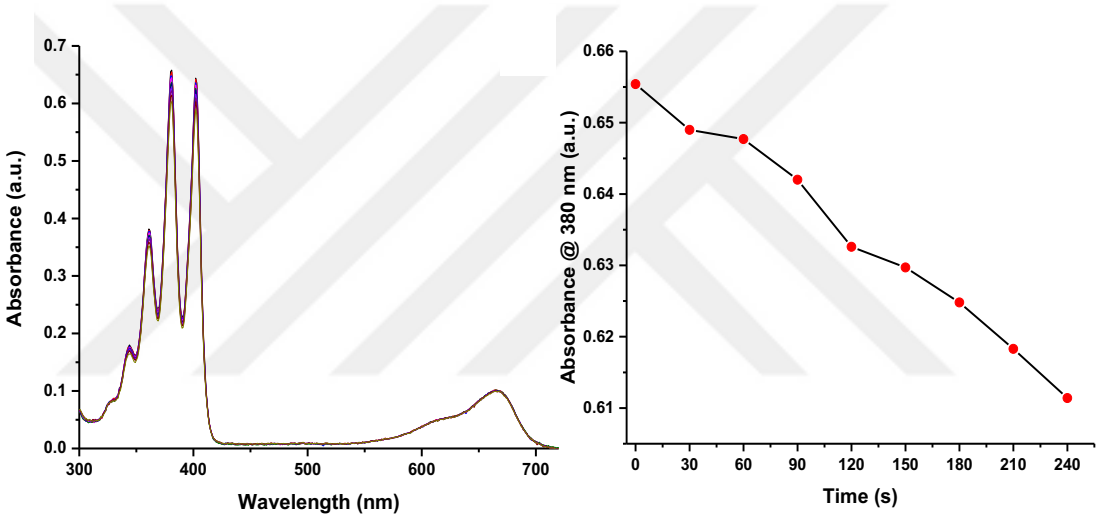

Figure 2.4 Absorption spectra of solution of MB (OD ~ 0.1) in PBS (pH 7.4, 10% DMSO) and ADMDA upon irradiation with 595 nm (a) LED light. Decrease in the absorption signal of ADMDA upon irradiation with 595 nm (b) LED light.

Selectivity

To perform selectivity experiments aqueous stock solutions of Na_2S, Cysteine, GSH, H_2O_2, $NaNO_2$, NaF, Na_2SO_3, NaBr, KSCN, $Na_2S_2O_3$, NH_4Cl, CH_3COONa, $KHCO_3$, H_2PO_4 were prepared in 1mM concentration. Then, solutions of **TM-I-H_2S** (10 µM, 10% DMSO, PBS pH 7.4) with addition of certain analyte in final 200 µM concentrations were obtained and their absorption and emission spectrums were recorded.

2.4 In Vitro Experiments

*2.4.1 In Vitro experiments of **SF-I***

Cell culture

Human colorectal carcinoma (HCT-116) cells and triple negative breast cancer (MDA MB-231) cells were grown in RPMI 1640 and DMEM high glucose supplemented with 10% heat-inactivated FBS, 200 mM L-glutamine, 100 U/mL penicillin and 100 µg/mL streptomycin in a humidified atmosphere of 5% CO_2 at 37 °C, respectively. The cells were sub-cultured at 80–90% confluency in every 2-3 days. Cells were used up to 4-6 passages in all experiments.

Dark toxicity and photodynamic effect

To evaluate the dark toxicity, cells were treated with the increasing concentrations (0.5-20 µM) of **SF-I** (dissolved in DMSO) for 24 h at culture conditions. For the photodynamic effect, cells were treated with same concentrations and irradiated with either 595 ± 5 nm (35.4 J/H_2S for 1 h and 70.8 J/cm^2 for 2 h) or 630 ± 10 nm (87.5 J/cm^2 for 1 h and 175.0 J/cm^2 for 2 h) LED light for various time intervals (1 or 2 h), followed by dark incubations up to 24 h at the incubator. Cell's viability was calculated by MTT assay.

Cell viability assay

The viability of cells was assessed with 3-(4,5-dimethylthiazol-2-yl)2,5-diphenyl-tetrazolium bromide (MTT) method. In brief, cells were seeded at a density of 2×10^4 cells/well at 37°C and then incubated with various concentrations of **SF-I**, as described above. After all incubation periods, 10 µL MTT solution (5 mg/mL in PBS) was added to each well containing 100 µL of fresh medium, and the samples were incubated at 37°C for 4 h. MTT formazan crystals were dissolved with 100 µL 10% SDS in 0.01 M HCl overnight at 37°C. The absorbance of each well was measured at reference wavelengths of 490 nm and 570 nm using a microplate reader (Multiskan Sky Microplatereader, Thermo Scientific, USA). Results were reported as the percentages of DMSO treated vehicle control. All the experiments were held three times (n=4).

Determination of ROS generation

Intracellular formation of ROS was assessed based on 2′,7′-dichlorodihydrofluororescein diacetate (DCFH-DA) assay. In brief, cells were seeded at

a density of 2 × 10^4 cells/well. Then cells were treated with **SF-I** (5 μM) in the presence or absence of 10 mM NaN_3 (singlet oxygen scavenger) and irradiated with 595 ± 5 nm LED light for 2 h at 37˚C. After incubation, the medium was removed, and the cells were washed 3 times with PBS. Cells were further incubated with 20 μM DCFH-DA for 30 min at 37˚C, shielded from light. Cells were washed with PBS twice and the fluorescence images were captured at 488 nm excitation using Zeiss LSM 900 confocal system (Carl Zeiss, Oberkochen, Germany). H_2O_2 (500 μM, 2 h) used as a positive control. (20× objective magnification). All the experiments were held in triplicate.

Assessment of cellular uptake

Cells were incubated with **SF-I** (5 μM) for 2 h at 37˚C. Then cells were wash with PBS twice and stained with 2 μg/ml Hoechst 33342 in HBSS for additional 10 min at 37˚C. After incubations, cells were washed three times with PBS and confocal fluorescence images were captured using Zeiss LSM 900 confocal system (Carl Zeiss, Oberkochen, Germany). Hoechst 33342 and **SF-I** were excited at 405 nm and 614 nm laser, respectively. 40X oil immersion objective lens was used.

Cell apoptosis assay

Cells were treated with **SF-I** (5 μM) in the presence or absence of 10 mM NaN_3 (singlet oxygen scavenger) and irradiated with 595 ± 5 nm LED light for 2 h at 37°C. Then incubated for additional 30 min at dark and stained with Annexin V Alexa Fluor™ 488- Propidium Iodide (PI) solution at room temperature in the dark for 15 min, according to the manufacturers protocol. After adding 500 μL of binding buffer, the cells were directly visualized by Zeiss LSM 900 confocal system (Carl Zeiss, Oberkochen, Germany) (20× objective magnification). All the experiments were held in triplicate.

*2.4.2 In vitro experiments of **TM-I-H_2S***

Cell Culture

Human colorectal carcinoma (HCT-116) cells and mouse embryonic fibroblast (NIH 3T3) cells were grown in RPMI 1640 and DMEM high glucose supplemented with 10% heat-inactivated FBS, 1% L-glutamine, 1% penicillin/streptomycin, 1% amphotericin in a humidified atmosphere of 5% CO_2 at 37 °C, respectively. The cells were examined with inverted light microscope to check confluency in every 2-3 days. When 70–80% confluency obtained, cells were sub-cultured used up to 3-7 passages in all experiments.

Dark toxicity and photodynamic effect

HCT-116 cells were seeded to 96-well plate at a density of 2×10^4 cells/well at 37°C and then incubated. To evaluate the dark toxicity, cells were treated with the increasing concentrations (0.1-20 μM) of **TM-I-H_2S** (dissolved in DMSO) for 24 h at culture conditions. For the photodynamic effect, cells were treated with same concentrations and irradiated with 595 ± 5 nm (9.83 mW/cm^2) LED light for various time intervals (2 or 4 h), either in absence or presence of singlet oxygen scavengers NAC (5mM), NaN_3(10mM), mannitol (20mM) followed by dark incubations up to 24 h at the incubator. Cell's viability was calculated by MTT assay.

Cell viability assay

The viability of cells was assessed with 3-(4,5-dimethylthiazol-2-yl)2,5-diphenyl-tetrazolium bromide (MTT) method. In brief, cells were seeded at a density of 2×10^4 cells/well at 37°C and then incubated with various concentrations of **TM-I-H_2S** as described above. After all incubation periods, 10 μL MTT solution (5 mg/mL in PBS) was added to each well containing 100 μL of fresh medium, and the samples were incubated at 37°C for 4 h. MTT formazan crystals were dissolved with 100 μL 10% SDS in 0.01 M HCl overnight at 37°C. The absorbance of each well was measured at reference wavelengths of 490 nm and 570 nm using a microplate reader (Multiskan Sky Microplate reader, Thermo Scientific, USA). Results were reported as the percentages of DMSO treated vehicle control. All the experiments were held three times (n=4). Obtained results were analyzed in GraphPad Prism 8.0 software and IC_{50} values were calculated by analyzing non-linear regression.

Determination of Intracellular localization

Cells were seeded at a density of 1×10^4 cells/well at 37°C in petri dishes (35mm) and incubated with **TM-I-H_2S** (1 μM) for 4 hours at 37 °C, 5% CO_2. Then, cells were washed with PBS three times and fixed with 4% paraformaldehyde. After fixation, excess paraformaldehyde was removed by washing and cells are incubated with mitochondria stain Janus B Green (5 μM) for 30 minutes; nucleus stain Hoechst 33342 (1 μg/mL) for 5 minutes at room temperature. Cells are washed after incubation and confocal images

were obtained at 361⁄497 nm (ex/em) (Hoechst), and 490/516 (ex/em) (JGB), 567/590-650 (ex/em) (LSM 900, Carl Zeiss, Almanya) (40X) (n=3).

Determination of Intracellular ROS generation

Intracellular formation of ROS was assessed based on 2′,7′-dichlorodihydrofluororescein diacetate (DCFH-DA) assay. In brief, cells were seeded at a density of 2×10^4 cells/well. Then cells were treated with **TM-I-H_2S** in concentration and time decided by IC_{50} calculation in the presence or absence of NAC (5mM), NaN_3(10mM), mannitol (20mM) and irradiated with 595 ± 5 nm LED light at 37°C. After incubation, the medium was removed, and the cells were washed 3 times with PBS. Cells were further incubated with DCFH-DA (20 µM), Hoechst 33342 (1 µg/mL) and prodiyum iodie (PI, 10 µg/mL) for 30 min at 37°C, shielded from light. Cells were washed with PBS twice and the fluorescence images were captured at 488 nm excitation using Zeiss LSM 900 confocal system (Carl Zeiss, Oberkochen, Germany). H_2O_2 (500 µM, 2 h) used as a positive control. (20× objective magnification). All the experiments were held in triplicate and 4 images were obtained for each group (10X).

Evaluation of apopthosis/necrosis ratio

Annexin V and PI dyes are used for cell death mechanism studies. Cells were seeded at a density of 2×10^4 cells/well in 96-well plate and incubated with **TM-I-H_2S** (IC_{50}) for 4 h. Then, they are exposed to 595 nm LED (9.83 mW/cm^2) in presence and absence of NAc or NaN_3. After light exposure, cells were washed with HEPES including Ca^{2+} two times then incubated with AV-Alexa Fluor™ (5 µg/mL), PI (488.1 µg/mL) and Hoechst 33342 (1 µg/mL) in dark at 37 °for 15 min followed by the washing procedure with HEPES. After washing , focal images were obtained at wavelengths ex/em: 361⁄488 nm, ex/em: 535⁄ 617 nm ve 361⁄497 nm (ex/em) for AV,PI and Hoechst respectively by using Zeiss LSM 900 confocal microscope. Carl Zeiss, Oberkochen, Germany) (10×).

Chapter 3:

RESULTS AND DISCUSSION

3.1 Synthesis of SF-I

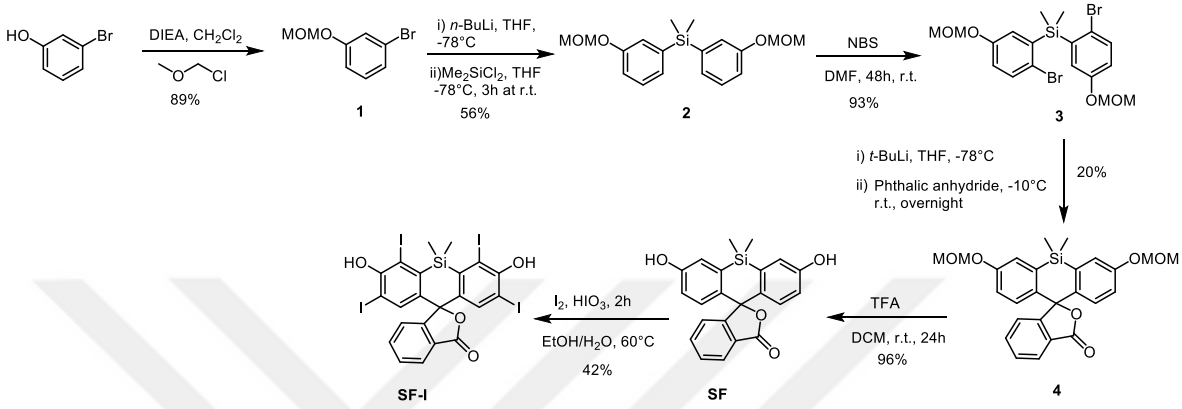

Figure 3.1 The synthetic pathway of **SF-I**.

For the synthesis of **SF,** a literature method developed by Lavis group was followed. (Fig. 3.1).[113] The first step in this synthetic path was the protection of phenol group with methyl methyl ether by using DIEA as base in DCM. This group is known to be stable under basic conditions and can be removed by acid treatment. This is to protect acidic proton which can be destroyed by strong base and nucleophile *n*-BuLi in the next step. In the second step *n*-BuLi was used to perform Li-Halogen exchange and then substitution was performed by adding dimethylsilane group. This step was performed under argon atmosphere in a dry polar aprotic solvent (THF) at -78 ^{o}C with caution as *n*-BuLi is a pyrophoric reagent and it is very strong base, presence of any acidic proton can block the action of *n*-BuLi and destroy reaction. Following step was the bromination of active ring from *para* position of ether group by using NBS as brominating reagent in DMF. In the structure, there are two competing positions (*ortho* and *para* positions), that is why NBS was used to perform controlled bromination of *para* position only and the product was obtained with a good yield. It was followed by another very sensitive reaction procedure including the use of *t*-BuLi. This reaction has low yield as after Li-Halogen exchange, obtained intermediate is very reactive, dryness of reaction environment and the temperature is crucial to control its reactivity. Also, *t*-BuLi can lose its activity in the presence of any acidic proton or even in the presence of trace amount of water. Although

all cautions were taken considering aforementioned issues, reaction yield could only be increased above 20%. Then, the protecting group was removed by using trifluoroacetic acid (TFA) in DCM to obtain **SF** core. Finally, iodination of **SF** was aimed but halogenation of xanthene-based cores may be difficult due to their fully conjugated structure.[64] However, silicon-fluorescein in its lactone form with broken conjugation was found to be modified easily with iodine in the presence of iodic acid. Additionally, it was proved that introduction of only one iodine is difficult because higher iodinated derivatives can be formed as side products. Therefore, reaction conditions were designed to push tetra iodination directly. As a result, successful tetra-iodination of active phenol rings with iodine and catalytic amount of iodic acid resulted in **SF-I**.

3.2 Photophysical properties of SF-I

After the successful synthesis of **SF-I**, photophysical characterization experiments were performed. First, emission and absorption spectra of **SF-I** at physiological pH (7.4) were measured. Absorption maxima of **SF-I** was found to be at 614 nm and emission peak located at 630 nm. (Figure 3.2) Owing to iodine in the structure, there is a red-shift compare to parent **SF** core, which has absorption and emission maxima at 580 nm and 598 respectively.[114] Additionally, fluorescence quantum yield of **SF-I** was found as 11% at pH 7.4. It is lower than the other **SF** derivatives without heavy atoms in their structures **(SF-Cl, SF-F)** due to the effective heavy atom mediated ISC. This is because ISC is a

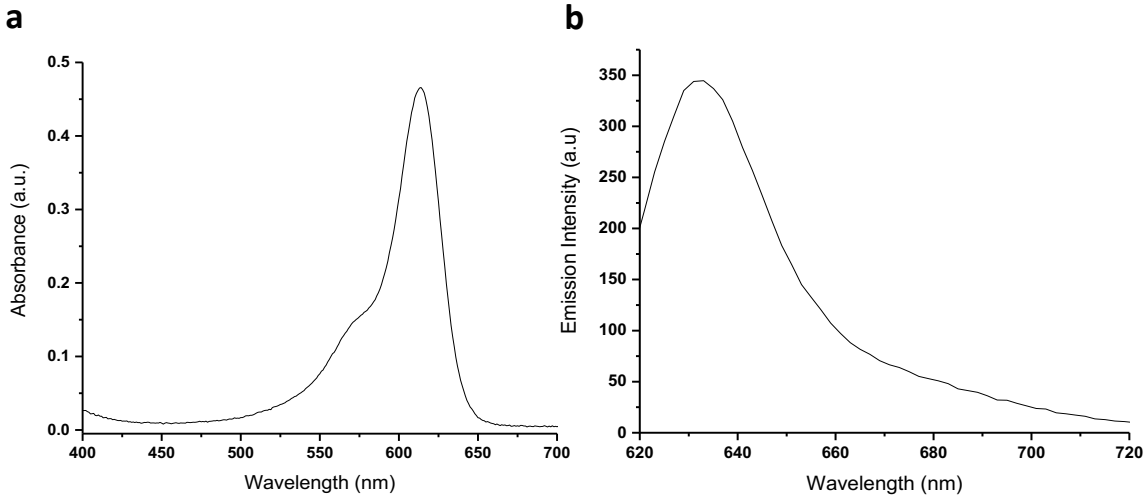

Figure 3.2 Absorption (a) and emission spectra (b) of **SF-I** (5 μM) in PBS (pH 7.4, 0.5% DMSO).

competing relaxation pathway to the fluorescence. However, **SF-I** did not lose its emission completely and its yield can still be considered as high enough to be used as a diagnostic agent.

Table 3.1 Photophysical properties and $^1O_2$ quantum yields of **SF-I** and **SF**.

PS	λ_{abs} (nm)	ε ($M^{-1}cm^{-1}$)	λ_{ems} (nm)	φ_F (%)	φ_Δ (%)[c]
SF-I	614[a]	76500[a]	630[a]	11[a,b]	45 ± 0.08[a,d] 30 ± 0.01[a,e]
SF	580[f]	110000[f]	598[f]	38[f]	n.d.

[a] measured in PBS buffer (pH 7.4, 0.5% DMSO) [b] calculated via spectrophotometer with an integrated sphere detector [c] methylene blue was used as a reference in PBS buffer ($\Phi_\Delta = 0.52$)[115] [d] upon irradiation with a 595 nm LED [e] upon irradiation with a 630 nm LED [f][114], n.d.: not determined

Next, it is important to show the pH dependance of the absorption and fluorescence signals of **SF-I**. It is known that fluorescein conjugates exist majorly in two different forms as intramolecular spirolactone and dianion and conversion between these two forms depends on pH of the medium. Lactone form is colorless and non-emissive as conjugation is lost due to broken π-system on the xanthene moiety, while dianion form is highly emissive. **SF** was shown to be predominantly in its lactone form at physiological pH (7.4).[110] It was foreseen that iodination of the core decreases the pKa of the phenolic oxygen due to the inductive effect caused by iodine. Thus, **SF-I** is expected to form dianion at physiological pH. This is also supported by literature examples on modification of xanthene core of **SF** with electron withdrawing halogens like chlorine (**SF-Cl**) and fluorine (**SF-F**). (Figure 3.3). These agents are in their deprotonated dianion form so

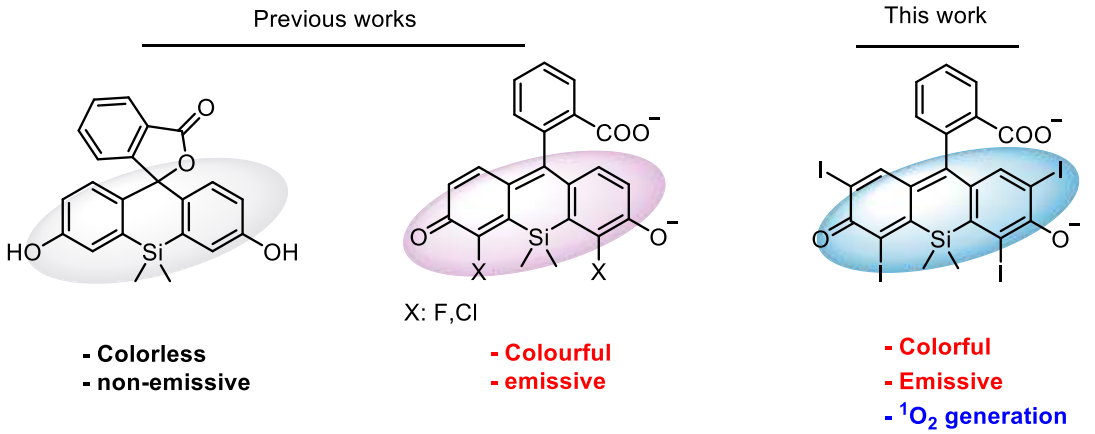

Figure 3.3 Chemical structures of different silicon fluorescein derivatives at physiological conditions (pH 7.4)

colorful and highly emissive at physiological pH.[110] Therefore, modification of **SF** with iodine is also expected to form predominantly or fully deprotonated dianion at physiological medium.

To prove iodine improves the predominance of dianion form of **SF-I** at pH 7.4, pH titration was performed by preparing aqueous solutions of **SF-I** at different pH values. Change in absorption and emission of these solutions were recorded. (Figure 3.4) In figure 3.4a and c, increase in the absorption and emission spectrum of **SF-I** clearly showed pH

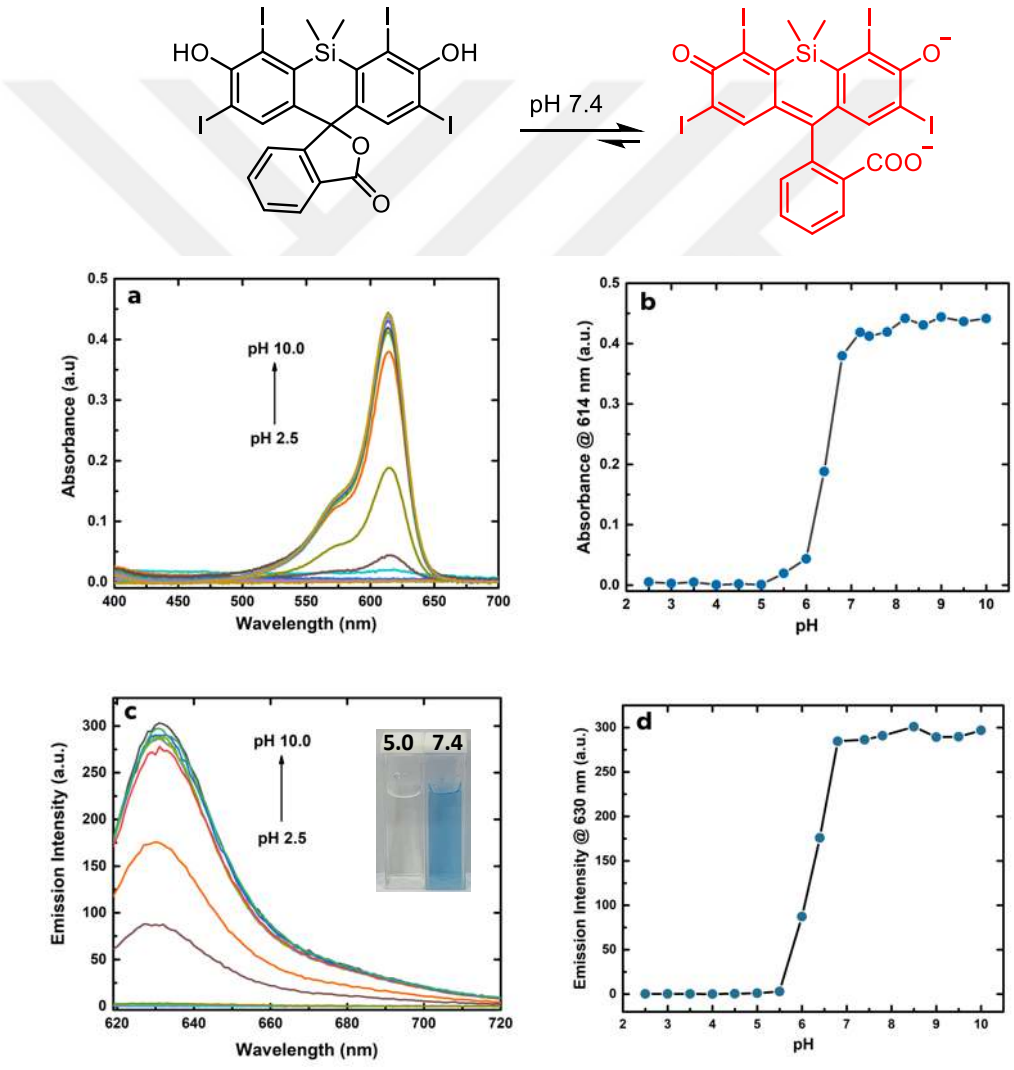

Figure 3.4 pH dependent change in the structure. Absorption (a) and emission spectra (c) of **SF-I** (5 μM) in different buffers (pH 2.5, 3.0, 3.5, 4.0, 4.5, 5.0, 5.5, 6.0, 6.4, 6.8, 7.4, 7.8, 8.5, 9.0, 9.5, 10.0, 0.5% DMSO). Corresponding pH plots of absorbance at 614 nm (b) and fluorescence at 630 nm (d). Reproduced from ref. 111 with permission from ACS copyright 2021.

dependent increase centered at 614 nm and 630 nm, respectively. In acidic pH below 5, no absorption and emission observed, meaning **SF-I** is in its lactone form completely. Figure 3.3.b and d, show pH versus absorption at 614 nm graph, which also concludes **SF-I** fully forms dianion at pH 7.4 so it is emissive and colorful like **SF-Cl** and **SF-F**.

3.3 Chemical detection of singlet oxygen production

Singlet oxygen generation of **SF-I** was evaluated by using a water-soluble trap molecule ADMDA, which reacts with singlet oxygen and loses its conjugation. Solution of **SF-I** (5 μM) was prepared in oxygen saturated PBS (0.5% DMSO, pH 7.4) and ADMDA (O.D.~1.0) was added to the solution. Initially several measurements were taken in dark to show no change in the absorption of ADMDA without light irradiation. Then, the solution was exposed to LED light (595 nm, 9.83 mW/cm^2, 630 nm, 24.3 mW/cm^2) and absorption spectrum was recorded. (Figure 3.5) As **SF-I** has a broad absorption band spanning between 550-650 nm in aqueous solutions, two different LED lights (595 nm, 630 nm) were used.

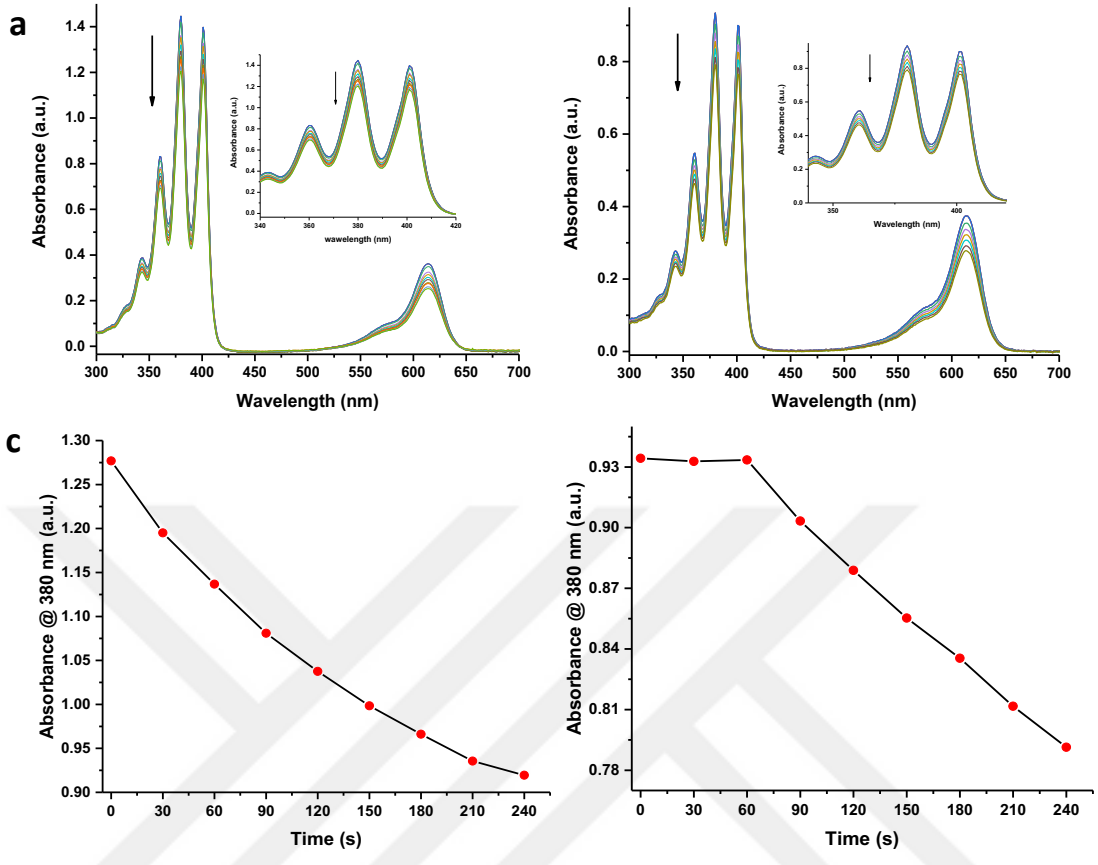

Figure 3.5 Absorption spectra of solution of SF-I (5 μM) in PBS (pH 7.4, 0.5% DMSO) and ADMDA upon irradiation with 595 nm (a) 630 nm (b) LED light. Decrease in the absorption signal of ADMDA upon irradiation with 595 nm (c) 630 nm (d) LED light.

It was observed that after each irradiation, absorption of ADMDA at 380 nm decreased as generated $^1O_2$ performs [4+2] cycloaddition to the anthracene core. That is, the gradual decrease in ADMDA absorption is directly related with $^1O_2$ production. The graph of time versus absorbance of ADMDA at 380 nm was drawn for both cases. (Figure 3.5c, d). In order to determine $^1O_2$ quantum yield of **SF-I,** methylene blue (Φ_Δ = 52% in PBS buffer)[115] was used as a reference PS and yield was calculated as 45% with 595 nm light irradiation and 30% with 630 nm light irradiation. It was concluded that irradiation with 630 nm light can also induce $^1O_2$ production in a good yield. Yet, $^1O_2$ quantum yield of **SF-I** with 630 nm light irradiation was found to be lower than that of 595 nm excitation. This may result from stronger absorption signal at 595 nm and the flux of two lights is different. Additionally, same experiment was performed with **SF** upon 595 nm light irradiation by using ADMDA to prove iodine in the structure is responsible for $^1O_2$

production and there will be no $^1O_2$ generation in non-iodinated form. As suggested, no change in the absorption of ADMDA was observed.

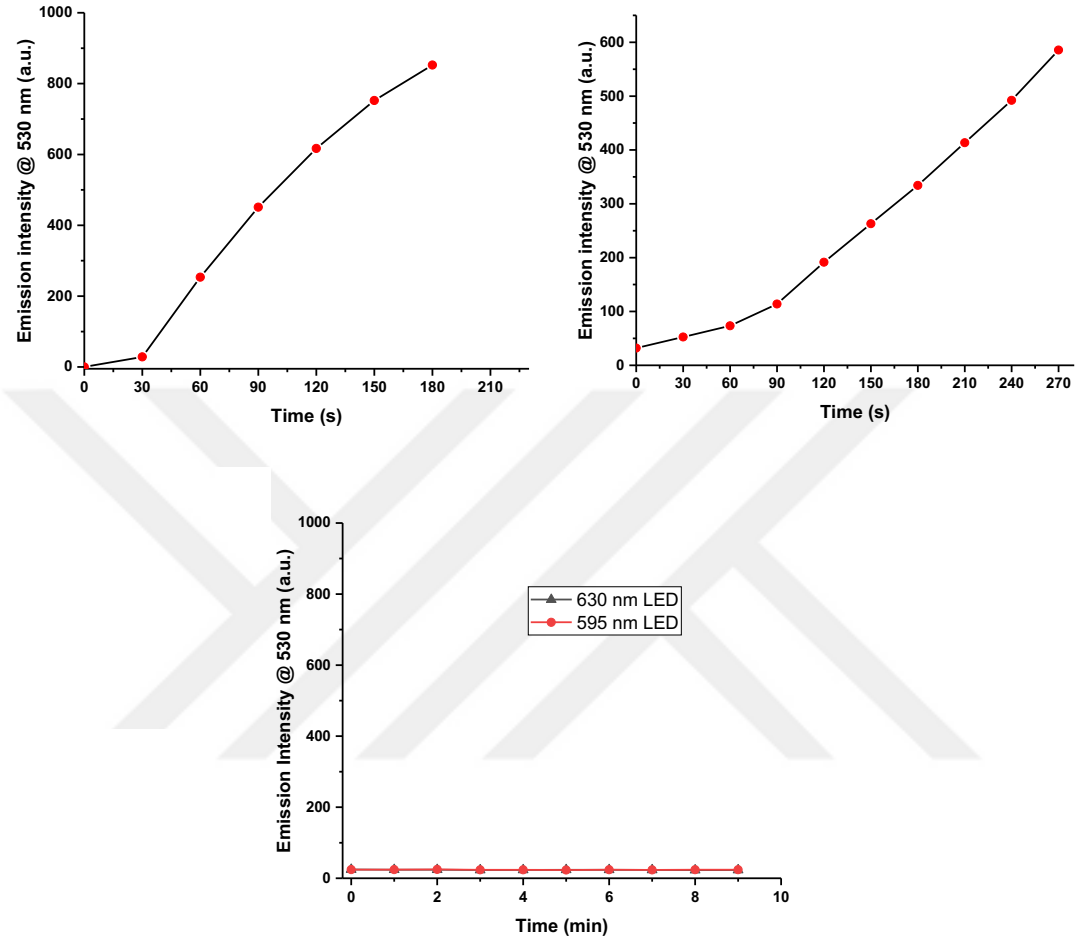

Figure 3.6 Increase in the emission signal of SOSG upon irradiation of SF-I (5 µM) with 595 nm (a) with 630 nm (b) LED light, change in the emission of blank solution upon irradiation with 595 nm/630 nm LED light (c).

$^1O_2$ production was further confirmed by using singlet oxygen sensor green (SOSG). In this case, appearance of green emission at 530 nm indicates $^1O_2$ production as SOSG reacts with $^1O_2$ selectively, which breaks conjugation on anthracene in the structure and blocked PET results in turn-on fluorescence response. (Figure 2.2) Irradiation of aqueous solutions of **SF-I** (5 µM, 0.5% DMSO, PBS pH 7.4) with a LED light (595 nm/630 nm), in the presence of SOSG displayed a gradual increase in the emission intensity of SOSG at 530 nm. (Figure 3.6). This clearly indicates the presence of photosensitized singlet oxygen. This experiments also showed that 595 nm light irradiation causes more increase

in SOSG emission compared to 630 nm. This result supports the singlet oxygen quantum yield results. A blank solution was also evaluated to prove that SOSG does not show degradation with light irradiation without **SF-I**. (Figure 3.6c).

Photostability

Photostability experiments were also carried to show that the LED lights are safe. Solution of **SF-I** (5 µM, 0.5%DMSO/PBS) was prepared and exposed to light for 2 hours in total and absorption and emission spectra were recorded at 30 minutes interval. The experiment was repeated for both light sources 630 nm and 595 nm and only a small decrease in both emission and absorption signals of **SF-I** were observed. However, this can be ignored as it has high singlet oxygen quantum yield and does not require light irradiation more than 2 hours. Further *in vitro* studies demonstrated that 1- or 2-hours light irradiation is enough to trigger almost complete cell death.

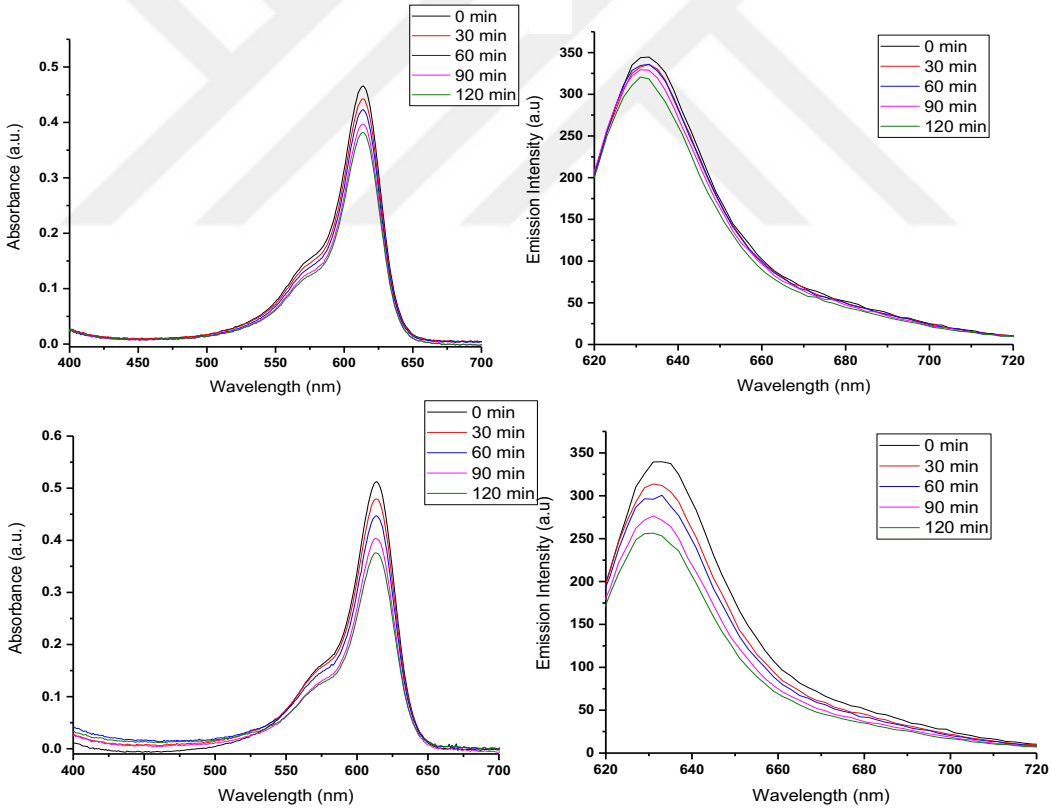

Figure 3.7 Absorption and emission spectra of SF-I respectively upon 630 nm (a), (b) and 595 nm, (c), (d) LED irradiation.

3.4 In vitro Evaluation of SF-I

After ensuring the $^1O_2$ production in aqueous solution, *in vitro* photocytotoxicity of **SF-I** was investigated first by conventional MTT assay in two different cell lines, triple negative breast (TNBC, MDA MB-231) and colorectal (HCT-116) cancers. These cells are known to show complex prognosis and limited chemotherapeutic options are possible for them.[116,117] To find IC_{50} value, cells were incubated with different concentrations of **SF-I** spanning from 0-20 µM and then exposed to light with two different LED sources (595 nm and 630 nm, 9.83 and 24.3 mW/cm^2) for 1 or 2 hours. Irradiation with both light sources resulted in a gradual decrease in dell viability in a dose-dependent manner in both cancer cells. (Figure 3.8) Lower IC_{50} values were obtained in 2 hours light irradiation predictably (Figure 3.8, Table 3.2). The 595 nm irradiation demonstrated more toxicity

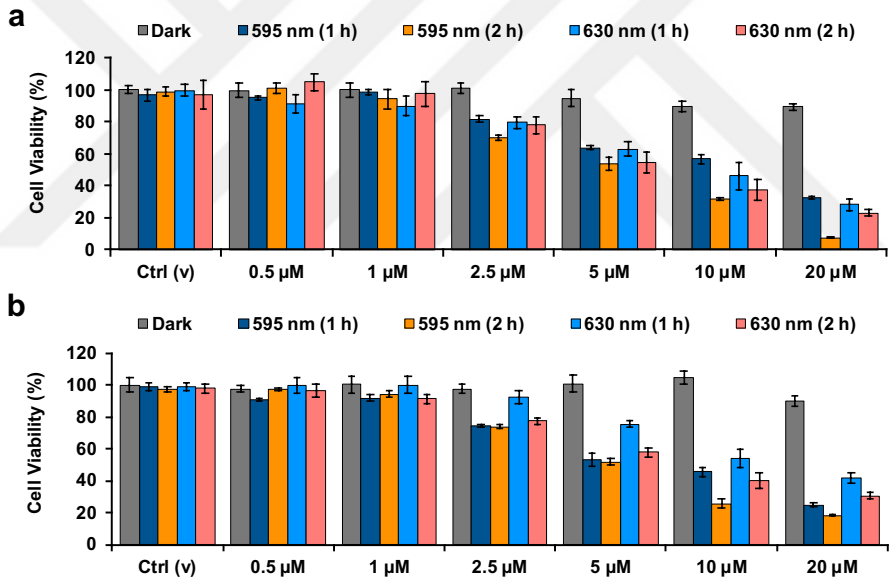

Figure 3.8 Cell viabilities of HCT-116 (a) and MDA MB-231 (b) cancer cells treated with the increasing concentrations (0.5-20 µM) of SF-I either at dark (24 h) or upon irradiation with LED light (595 nm or 630 nm) for 1 h or 2 h, followed by 23 h and 22 h dark, respectively. Ctrl(v): vehicle control. Data is presented as mean ± SD. (n=4). Reproduced from ref. 111 with permission from ACS copyright 2021

compared to that of 630 nm. This can be correlated with higher $^1O_2$ quantum yields upon 595 nm irradiation (Table Sx). Yet, 630 nm light has ability to penetrate deeper so IC_{50} values upon 630 nm irradiation is also reasonable in both cells. Cell viability was not affected under dark even at high concentrations. That is, cytotoxicity was triggered by light only, so **SF-I** is advantageous over standard PS methylene blue with its comparable

$^1O_2$ generation yield and no observable dark toxicity unlike MB, which shows inherent dark toxicity.[118] Cytotoxicity of light source was also investigated and no detectable cytotoxicity was observed.

Table 3.2 Calculated IC_{50} values of **SF-I** irradiated with LED light sources (595 nm or 695 nm) at different time intervals (1h or 2h) followed by dark incubation up to 24 h in HCT-116 and MDA MB-231 cancer cell lines.

	HCT-116 (IC_{50})		**MDA MB-231 (IC_{50})**	
LED (λ)	**1 h**	**2 h**	**1 h**	**2 h**
595 nm	11.34 μM	**5.35 μM**	7.04 μM	**5.38 μM**
630 nm	8.45 μM	6.72 μM	13.41 μM	7.56 μM

Another method employed to show intracellular ROS generation induced by **SF-I** upon light irradiation is to use a cell permeable ROS sensor 2',7'-dichlorofluorescein diacetate ($DCFH_2$-DA) as a stain and monitor cancer cells (MDA MB-231 and HCT-116) under confocal microscopy. $DCFH_2$-DA emits strong green emission in presence of ROS through oxidation. Both cells were incubated with $DCFH_2$-DA and **SF-I** then irradiated with a 595 nm light. In figure 3.9(c, h), the observed green emission is the result of ROS production. To examine if ROS species responsible for green emission is singlet oxygen, a singlet oxygen scavenger NaN_3 was used.[119] Treatment of the cells with NaN_3 resulted in disappearance of the green emission which means that primary cytotoxic agent in PDT action induced by **SF-I** is singlet oxygen. (Figure 3.9d,i) Also, no detectable green emission was observed in the cells treated in dark control and the cells incubated only with $DCFH_2$-DA under light irradiation. (Figure 3.9a,f,b,g) Finally, to check the reliability

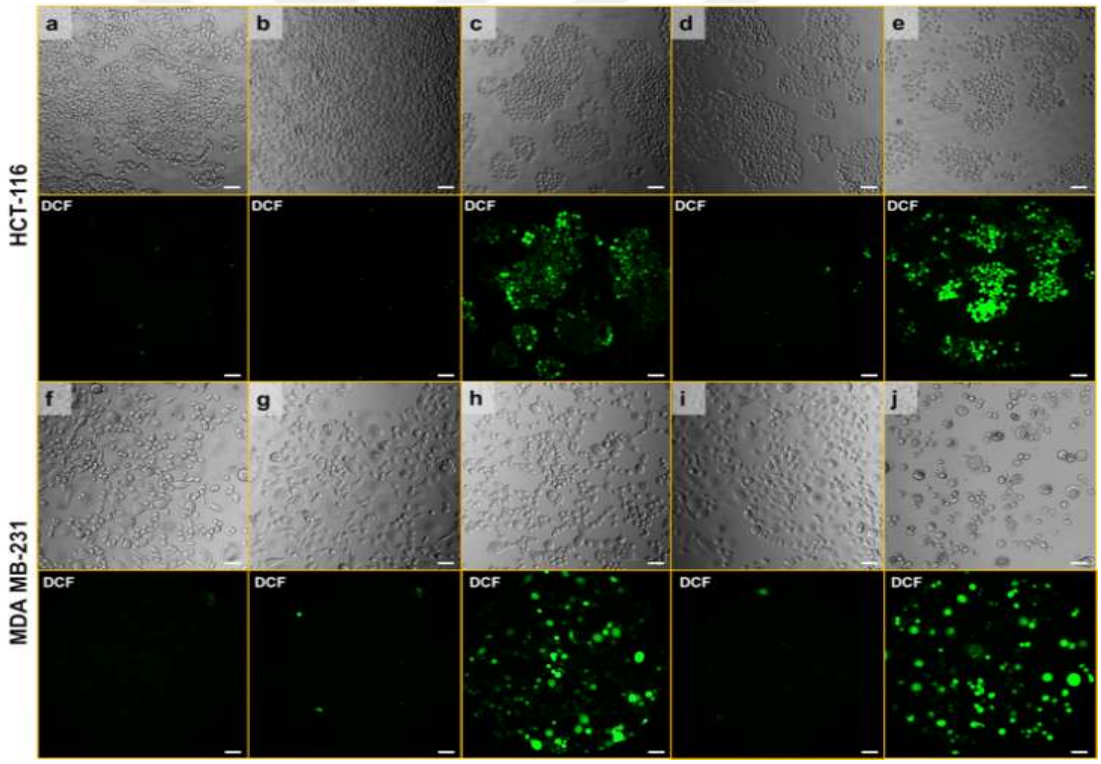

Figure 3.9 Intracellular ROS levels detected by DCFH2-DA staining in HCT-116 (a-e) and MDA MB-231 (f-j) cells treated with DMSO (0.5%) (a, f) or SF-I (5 μM) at dark (b, g). SF-I treated cells were irradiated with LED light (595 nm) in the absence (c, h) or presence (d, i) of NaN3 for 2 h. H2O2 (500 μM, 2 h) treated cells were used as positive control (e, j). Scale bar: 50 μm. Reproduced from ref. 111 with permission from ACS copyright 2021.

of staining, cells were pre-treated with H_2O_2 and proved that as expected $DCFH_2$-DA works fairly in the presence of ROS. (Figure 3.9e,j).

Green emitting annexin V-FITC (AV, detects early apoptotic cells) and red emitting propidium iodide (PI, detects late apoptotic and necrotic cells) were employed to examine cell death mechanism during the PDT action. The cells (MDA MB-231 and HCT-116) were incubated with **SF-I** (5 µM) and irradiated for 2 hours with a 595 nm LED light followed by the treatment with AV and PI stains 30 minutes after PDT. Another group of cells were incubated with **SF-I** and treated in dark. Only irradiated cells display green and red emission in consistent with previous dark toxicity experiments. (Figure 3.10)

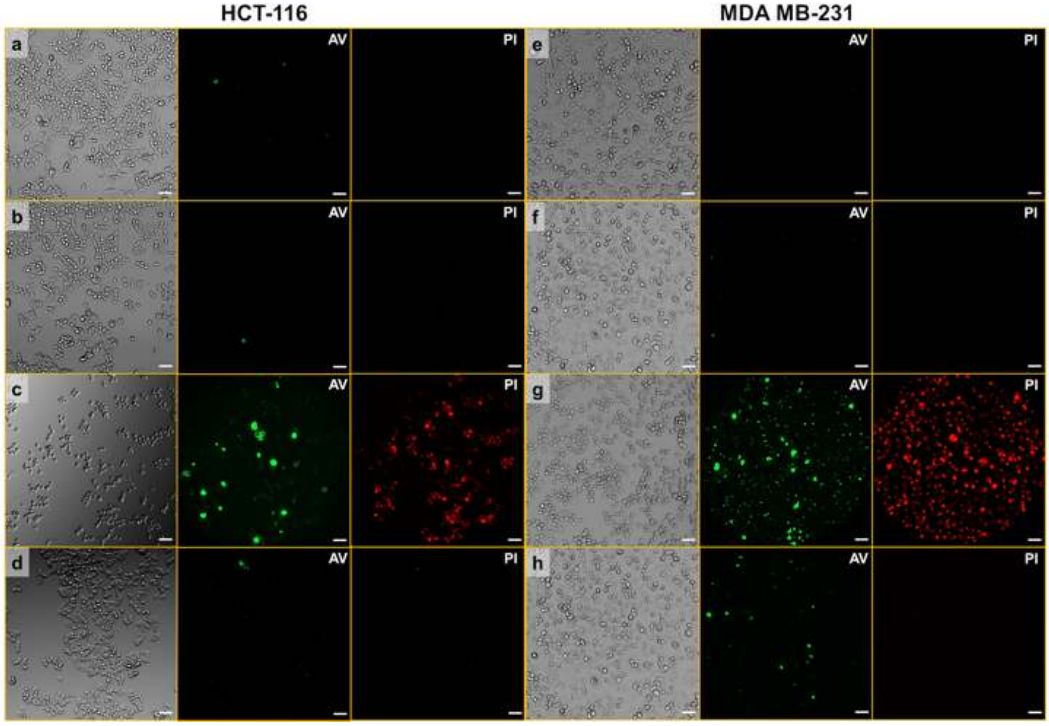

Figure 3.10 Confocal microscopy images of apoptosis and necrosis of HCT-116 (a−d) and MDA MB-231 (e−h) cells treated with DMSO (0.5%) (a, e) or SF-I (5 µM) under dark conditions (b, f). SF-I treated cells were irradiated with LED light (595 nm) in the absence (c, g) or presence (d, h) of NaN3 for 2 h. After treatments, cells were stained with Annexin V-FITC (green) and PI (red) to monitor apoptotic or necrotic cells, respectively. Scale bar: 50 µm. Reproduced from ref. 111 with permission from ACS copyright 2021.

Detection of both green and red emission means that there is early apoptosis as well as late apoptosis/necrosis at 30 minutes post PDT. (figure 3.10c,g). Further, treatment of cells with NaN_3 demonstrated a dramatic suppression in the cell death even after 2 hours PDT action. (Figure 3.10d,h) This also proves that the primary cytotoxic specie is $^1O_2$.

It was previously shown in solution experiments that **SF-I** has a strong emission signal in aqueous solutions at pH 7.4. Therefore, it is necessary to investigate *in vitro* imaging

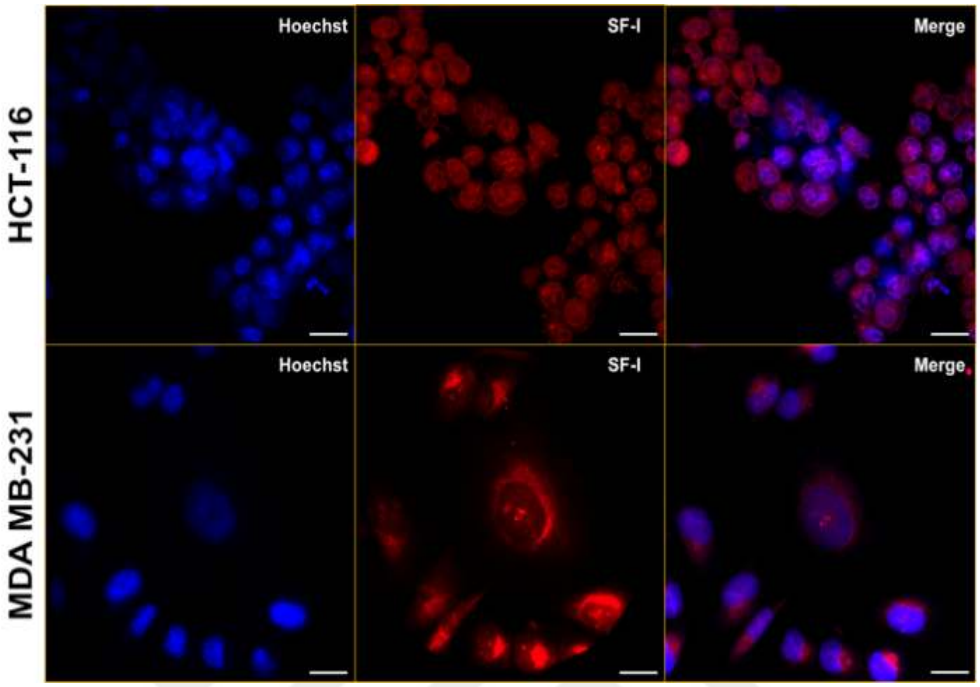

Figure 3.11 Confocal images of SF-I (5 μM) in HCT-116 (a) and MDA MB-231 (b) cancer cells after 2 h incubation. Blue, Hoechst 33342; red, SF-I. Scale bar: 20 μm. Reproduced from ref. 111 with permission from ACS copyright 2021

ability of **SF-I**. The cells (MDA MB-231 and HCT-116) were incubated with **SF-I** (5 μM) for 2 hours and washed prior to confocal imaging. Cytosolic and rarely nuclear red emission was observed in both cells. (Figure 3.11) That is, **SF-I** is cell permeable and can be used for imaging owing to its strong intracellular fluorescence signal despite of four iodine atoms in the structure.

In a nutshell,

3.5 Synthesis of TM-I-H_2S

To obtain **TM-I-H_2S**, synthesis of the cage group *p*-azidobenzyl bromide **(6)** and the synthesis of **TM** were performed separately. Then, the cage group was incorporated to the **TM** structure through substitution reaction under basic conditions followed by the iodination of the resulting structure.

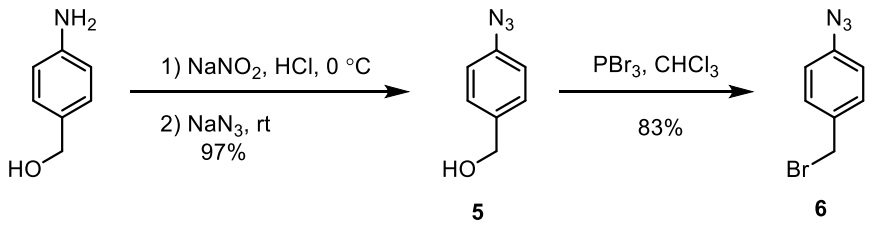

Figure 3.12 Synthetic pathway of para-azidobenzyl bromide **(6).**

First, the cage group **(6)** was synthesized starting with commercially available *p*-aminobenzyl alcohol. (Figure 3.12) It was converted into *p*-azidobenzyl alcohol **(5)** through Sandmeyer reaction followed by sodium azide addition. Then, benzylic hydroxy was brominated by using phosphorus tribromide in chloroform and *p*-azidobenzyl bromide **(6)** was obtained for further use as a caging group.

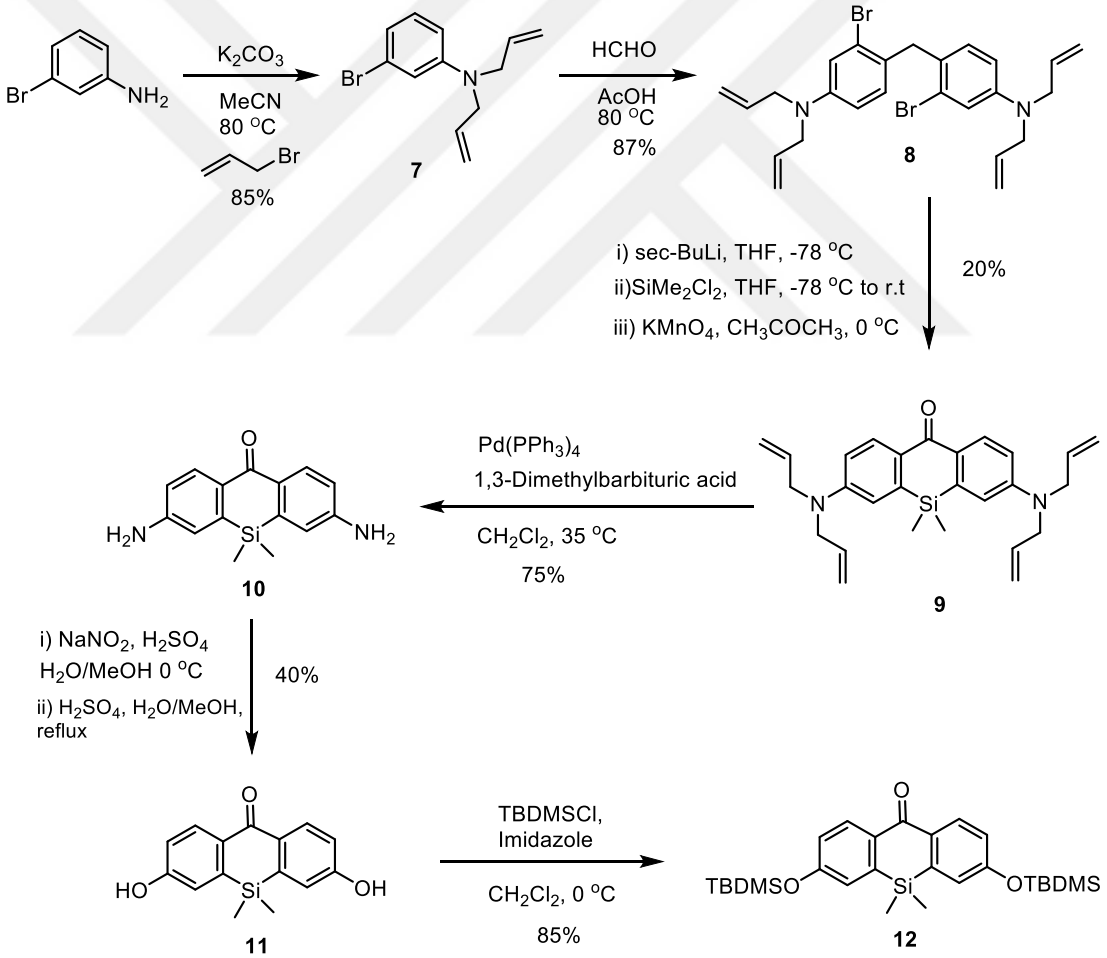

Figure 3.13 Synthetic pathway of key intermediate (12).

For the synthesis of **TM**, a method developed by Nagano research group which is based on the synthesis of xanthene moiety from 3-bromoaniline was followed (Figure 3.14). In this study, allyl group was used as protecting group due to weak electron-withdrawing character which results in less influence on the dimerization Additionally, it resists to destruction in lithiation reaction with *sec*-butyllithium for the synthesis of Si-containing xanthone **(9)**. Therefore, the first step for the synthesis is the protection of the amine group on 3-bromoaniline by using allyl bromide in MeCN to obtain **7**. Then, for the formation of **8** dimerization reaction was performed with formaldehyde and acetic acid at 80 °C. To obtain_Si-containing xanthone **(9)**, lithiation was performed with *sec*-BuLi at -78 °C followed by the addition of dimethylsilyl chloride to form silicon bridge. Without further purification, oxidation was applied with $KMnO_4$ in acetone at 0 °C. Allylic protecting group in this product was removed by using $Pd(PPh_3)_4$ and 1,3-dimethylbarbituric acid and diaminoxanthone **(10)** was obtained. To transform diaminoxanthone **(10)** to dihydroxyxanthone **(11)** sodium nitrite was used to form nitrous acid with sulfuric acid and eventually to form diazonium salt, which will be converted to hydroxy group by using H_2SO_4 at reflux temperature. The hydroxy groups on the

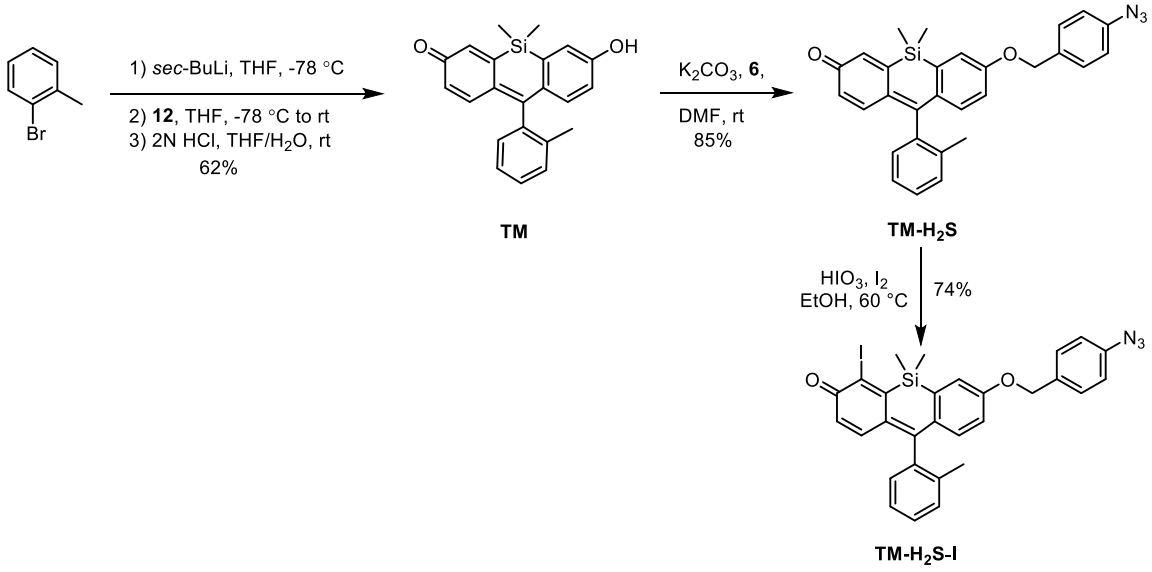

Figure 3.14 Synthetic pathway for **TM-I-H_2S.**

dihydroxyxathone **(11)** were protected by using TBDMSCl and key intermediate **(12)** was obtained.

The method to obtain **TM** is first Li-halogen exchange on commercially available *ortho*-bromo toluene by using *sec*-BuLi under argon atmosphere in dry THF at -78 ºC. Then, **12** addition of same conditions to perform addition of the 2-lithiated toluene to xanthanone with protecting groups was followed **(12).** Finally, after the removal of protecting group with HCl, **TM** should be obtained. At this point, iodination of this core could be performed but it was showed before on resorufin core that iodination of xanthene cores is difficult as they are fully conjugated. Additionally, previous study on resorufin proved that iodination is easier on xanthene cores[64] when phenol is replaced with a cage group. Therefore, first caging was performed through etherification with **6** by using potassium carbonate as base in DMF to obtain **TM-H$_2$S**. Later, iodination of **TM-H$_2$S** with iodine and iodic acid resulted in **TM-I-H$_2$S.**

3.6 Photophysical Characterization of TM-I-H$_2$S

After the successful synthesis of **TM-I-H$_2$S**, photophysical properties were investigated. First, emission and absorption characteristics of **TM-I-H$_2$S** in presence and absence of H_2S in aqueous solutions were investigated. The expectation is the change in

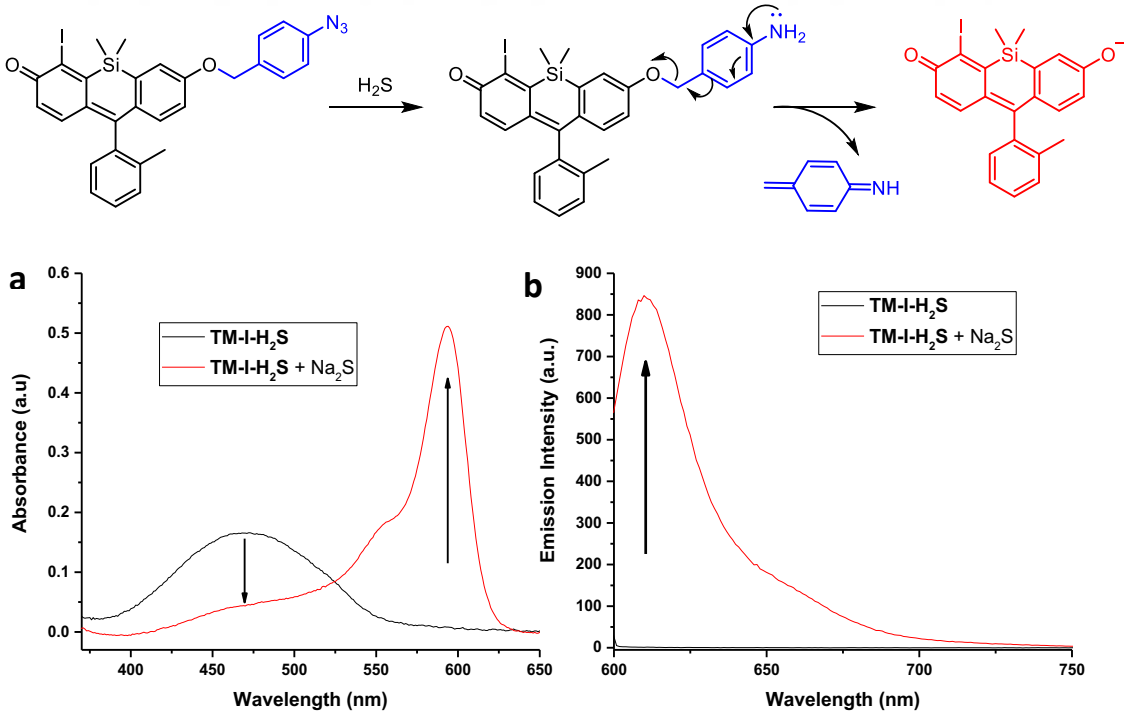

Figure 3.15 Activation mechanism of TM-I-H_2S with H_2S. Absorption (a) and emission (b) spectra of **TM-I-H$_2$S** in presence and absence of Na_2S

absorption and emission characteristics with the removal of the cage group with H_2S as shown in figure 3.15. Solution of **TM-I-H_2S** (10 μM) in PBS (pH 7.4, %10 DMSO) was prepared and its absorption maxima was found as 463 nm (ε = 16500 $M^{-1}cm^{-1}$). Then, to the solution of **TM-I-H_2S** (10 μM) in PBS (pH 7.4, %10 DMSO) Na_2S solution (200 μM) prepared in PBS (pH 7.4) was added to uncage **TM-I-H_2S** and color change was observed with naked eye. For experiments involving aqueous sulfide solutions, we used N_2S toproduce H_2S as it is more practical to use sulfide salts, Na_2S, rather than H_2S gas directly.[120] Absorption spectra also proved cage cleavage. While absorption peak with maxima at 463 nm disappeared, red-shifted sharper peak emerged with a maxima at 595 nm (ε= 50800 $M^{-1}cm^{-1}$). This clearly proves removal of cage group and formation of deprotonated iodo Tokyo Magenta in anionic form **(TM-I-O^-)** (Figure 3.15). In addition, emission of **TM-I-H_2S** both in presence and absence of H_2S was measured. While **TM-I-H_2S** solution with H_2S shows strong emission peak at 610 nm, no emission was observed without H_2S addition (ex: 595 nm) (Table 3.3).

Table 3.3 Table 3.4 Photophysical properties and $^1O_2$ quantum yields of **TM** derivatives.

PS	λ_{abs} (nm)	ε ($M^{-1}cm^{-1}$)	λ_{ems} (nm)	φ_F (%)	φ_Δ (%)[c]
TM-I-H_2S	463[a]	16500[a]	n.d.	n.d.	n.d.
TM-I-OH	489[b]	14200[b]	n.d.	n.d.	n.d.
TM-I-O^-	595[a]	50800[a]	610[a]	34[c]	34[d]
2-Me-TM -OH	472[e]	29000[e]	593[e]	10[e]	n.d.
2-Me-TM -O^-	582[e]	110000[e]	598[e]	42[e]	n.d.

[a] measured in PBS buffer (pH 7.4, 10% DMSO) (ex: 595 λ_{ems} for [b] measured in glycine buffer (pH 3.0, 10% DMSO) [c] calculated by taking TM as reference PBS buffer (pH 7.4, 10% DMSO) (ex: 582 nm) [d] methylene blue was used as a reference in PBS buffer (Φ_Δ = 0.52)[115] upon irradiation with a 595 nm LED [e] ref[112], n.d.: not determined

Fluorescence quantum yield of the **TM-I-H_2S** after the removal of cage group **(TM-I-O^-)** was calculated by using **2-Me-TM** as reference fluorophore whose fluorescence yield was known (42%)[112] and it was found as 34% (Table 3.3). It concludes that **TM-I-**

H_2S can be effectively employed as phototheranostic agent thanks to its reasonably high fluorescence quantum yield.

2-Me-TM was discovered to show a pH dependent change in the absorption and emission as summarized in introduction part and given in table 3.3.[112,114] **TM-I-H_2S** was also expected to show pH dependent change in absorption and emission characteristics after the removal of cage group. Additionally, it was reported by Nagano group that 78% of **2-Me-TM** is in anionic form with strong absorption in red region at physiological pH.[112] In case of **TM-I-H_2S,** this percentage was expected to increase owing to inductive

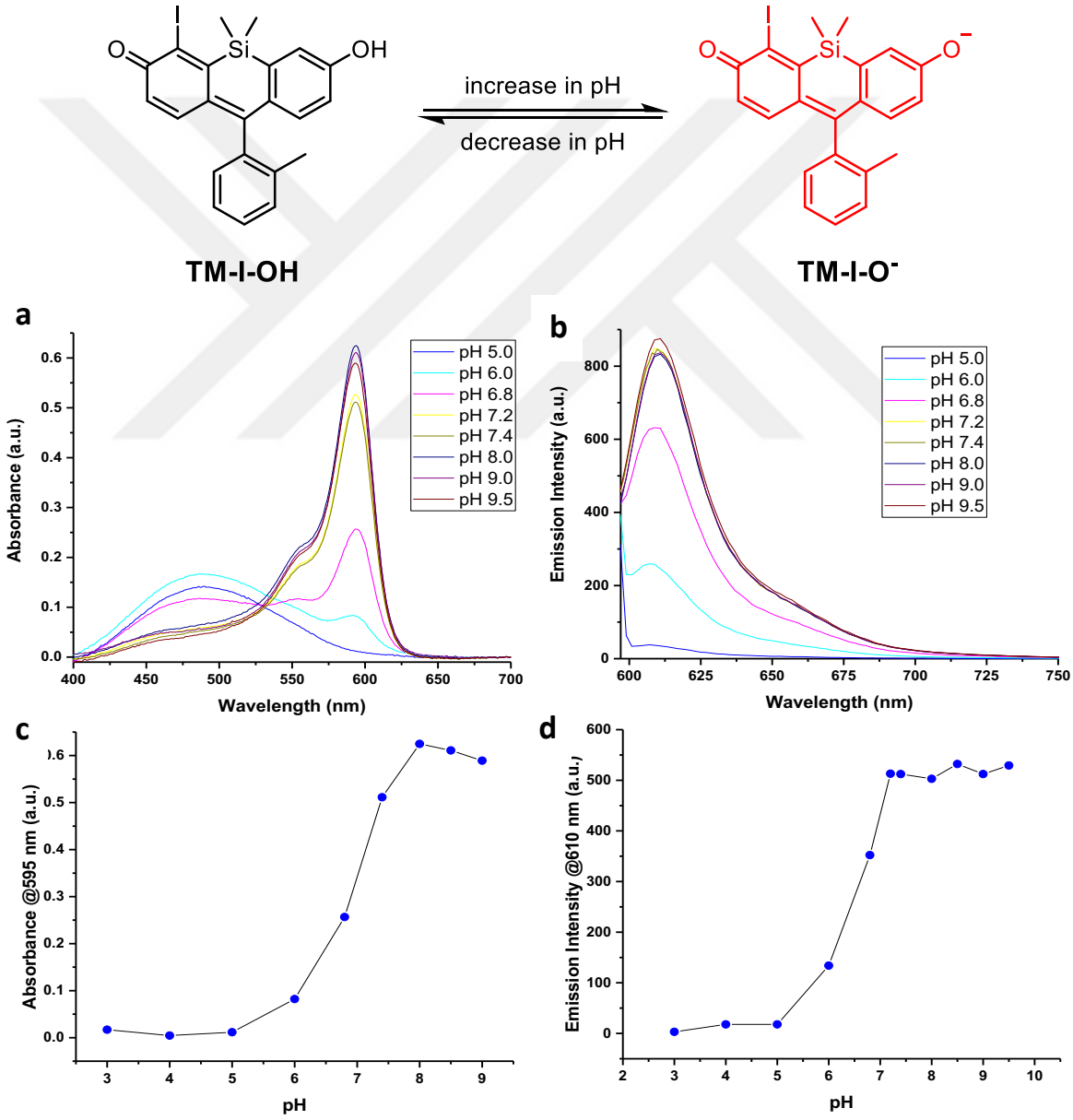

Figure 3.16 Deprotonation of TM-I-OH, absorption (a) and emission (b) spectra of TM-I in different buffer solutions. Absorbance (c) and emission (d) change with respect to pH.

effect of iodine. Therefore, absorption and emission spectrum of **TM-I-H_2S** after the removal of cage group was evaluated by using different buffer solutions (Figure 3.16).

In the absorption at 595 nm versus pH graph (Figure 3.16c), it can be concluded that maximum amount of **TM-I-O^-** was obtained at pH 8.0, then no further increase observed at higher pHs. At pH 7.4, almost 85% of **TM-I-OH** converted to anion form so as it is expected the concentration of anion form is higher than that of **2-Me-TM** due to lower pKa of **TM-I-OH.**

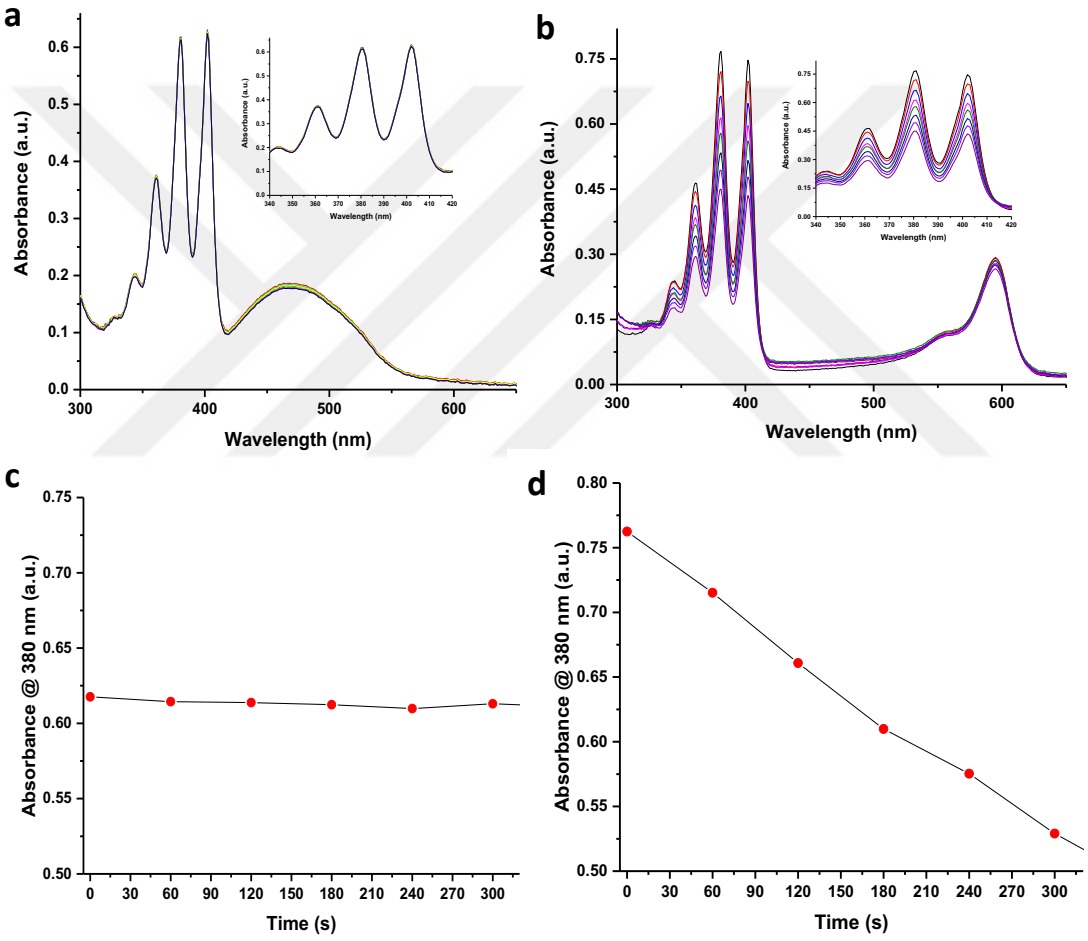

Figure 3.17 Absorption spectra of solution of **TM-I-H_2S** (10 µM) in PBS (pH 7.4, 10% DMSO) and ADMDA upon irradiation with 595 nm in absence of Na_2S (a) and presence of Na_2S (b). Change in the absorption signal of ADMDA upon irradiation with 595 nm in absence of Na_2S (c) and presence of Na_2S (d).

Singlet oxygen generation of **TM-I-H_2S** was evaluated by using a water-soluble trap molecule ADMDA, which reacts with singlet oxygen and lose its conjugation. Solution of **TM-I-H_2S** (10 µM) was prepared in oxygen saturated PBS (10% DMSO, PBS pH 7.4,

200 μM Na_2S) and ADMDA (O.D.~0.8) was added. Initially several measurements were taken in dark to show no change in the absorption of ADMDA without light irradiation. Then, the solution was exposed to LED light (595 nm, 9.83 mW/cm^2) and absorption spectrum was recorded. (Figure 3.17b). Same experiment repeated without addition of Na_2S means no H_2S present in the solution (Figure 3.17a)

It was observed that after each irradiation, absorption of ADMDA at 380 nm decreased in presence of H_2S (Figure 3.17d) and no change was detected in the absence of analyte (Figure 3.17c). The gradual decrease in ADMDA absorption is directly related with $^1O_2$ production so no singlet oxygen production was observed in the absence of H_2S with 595 nm light irradiation. The graph of time versus absorbance of ADMDA at 380 nm was drawn for **TM-I-H_2S** in presence of H_2S and slope of this curve was used for $^1O_2$ quantum yield (Φ_Δ) calculation (Figure 3.17d). In order to determine $^1O_2$ quantum yield of **TM-I-H_2S,** methylene blue (Φ_Δ = 52% in PBS buffer)[115] was used as a reference PS and yield was calculated as 34% upon 595 nm light irradiation.

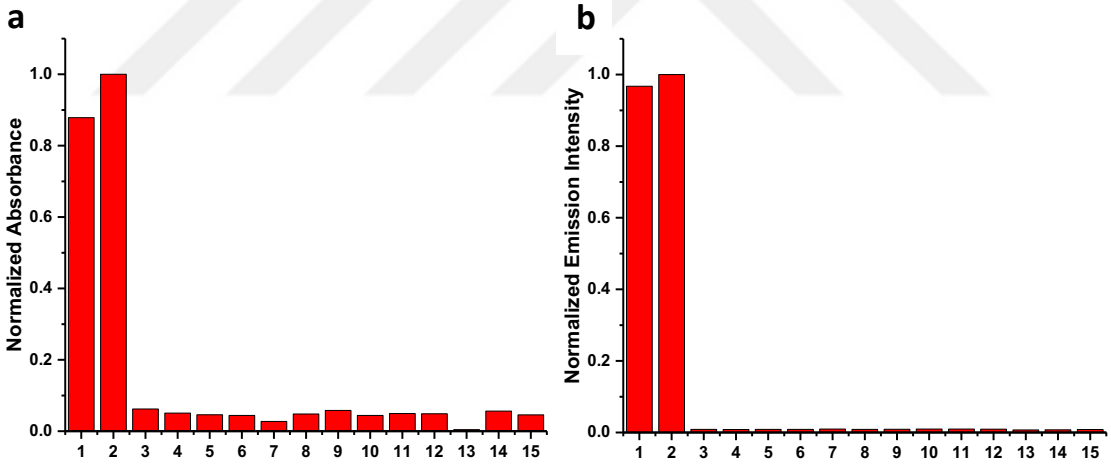

Figure 3.18 Absorption (a) and emission (b) signals of **TM-I-H_2S** at λ_{max} in presence of analytes; 1:Na_2S, 2:Na_2S+Cys+GSH, 3:Cys, 4:GSH, 5:H_2O_2, 6:$NaNO_2$, 7:NaF, 8: Na_2SO_3, 9:NaBr, 10: KSCN, 11: $Na_2S_2O_3$, 12: NH_4Cl, 13: CH_3COONa, 14: $KHCO_3$, 15: H_2PO_4 respectively.

Finally, selectivity experiments were performed to show that **TM-I-H_2S** activates its red shifted absorption and emission characteristics only in the presence of H_2S but not with other analytes. Several competing analytes (1mM) were added to the solution of **TM-I-H_2S** (10% DMSO, PBS pH 7.4) and absorption and emission of resulting solutions were recorded (Figure 3.18). No remarkable change was monitored in both absorption

and emission signals of the agent in the absence of H_2S. Thus, it was proven that **TM-I-H_2S** is only responsive to H_2S.

3.7 In vitro Experiments of TM-I-H_2S

After examining the photophysical properties of the **TM-I-H_2S** the in *vitro* therapeutic effect was investigated through cell culture studies. *In vitro* photocytotoxicity of **TM-I-H_2S** was investigated by conventional MTT assay in two different cell lines, triple negative breast (TNBC, MDA MB-231) and colorectal (HCT-116) cancers. Cells were treated with different concentrations of **TM-I-H_2S** spanning from 0-20 µM and incubated in the dark for 2 or 4 hours. Then cells were exposed to light with LED source (595 nm mW/cm^2) for 2 hours followed by the dark incubation for 24 hours. MTT assay showed a gradual decrease in cell viability in a dose-dependent manner in both cancer cells (Figure 3.19). It was determined that 4 hours of incubation time was more suitable for the activation of the agent and a dose dependent decrease in cell vitality after light stimulation for both cells (IC_{50}= 6.33 mM) (Figure 3.19). No significant toxicity were

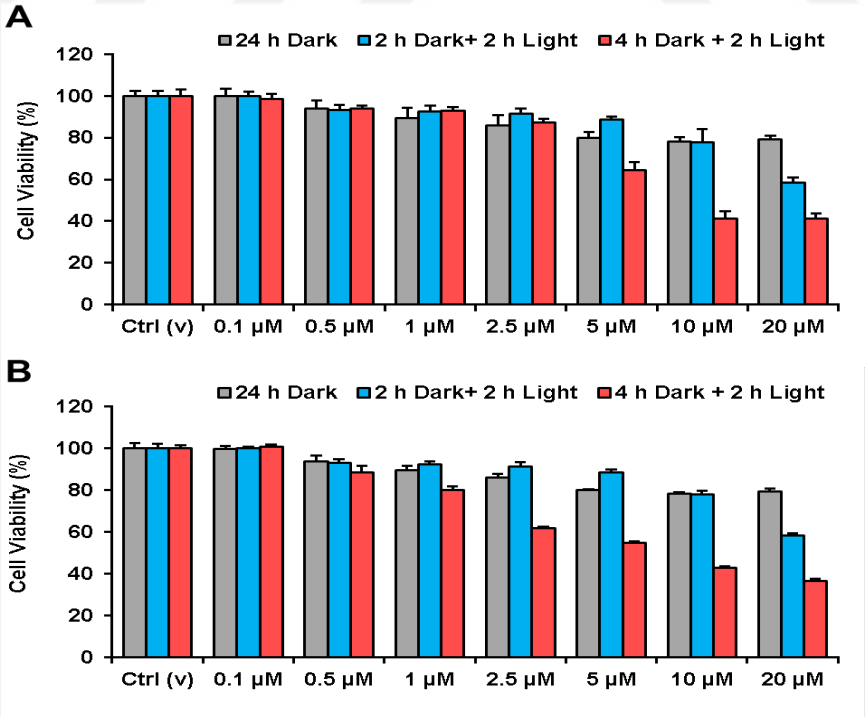

Figure 3.19 Cell viabilities of (a) MDA MB-231 and (b) HCT-116 cancer cells treated with the increasing concentrations (0.1-20 µM) of TM-I-H_2S either at dark (24 h) or 2 or 4 h at dark, followed by irradiation with LED light (595 nm 9.83 mw/cm^2 for 2 h, then incubated up to 24 h at dark. Ctrl(v): vehicle control. Data is presented as mean ± SD. (n=5-6)

detected in the cells without light (Figure 3.19). Thus, it has been shown that **TM-I-H_2S** agent can be activated with endogenous H_2S and then induce cell death as a result of PDT action without showing dark toxicity.

After showing cytotoxicity under light stimulation in the cells, intracellular ROS production induced by **TM-I-H_2S** agent and consequent cell death were monitored under confocal microscope in HCT-116 cancer cells using cell permeable ROS sensor 2'.7'-dichlorofloresein diacetate ($DCFH_2$-DA) and PI dyes (Figure 3.20). The cells are also stained with nuclear dye Hoechst. The observed green emission is the result of ROS

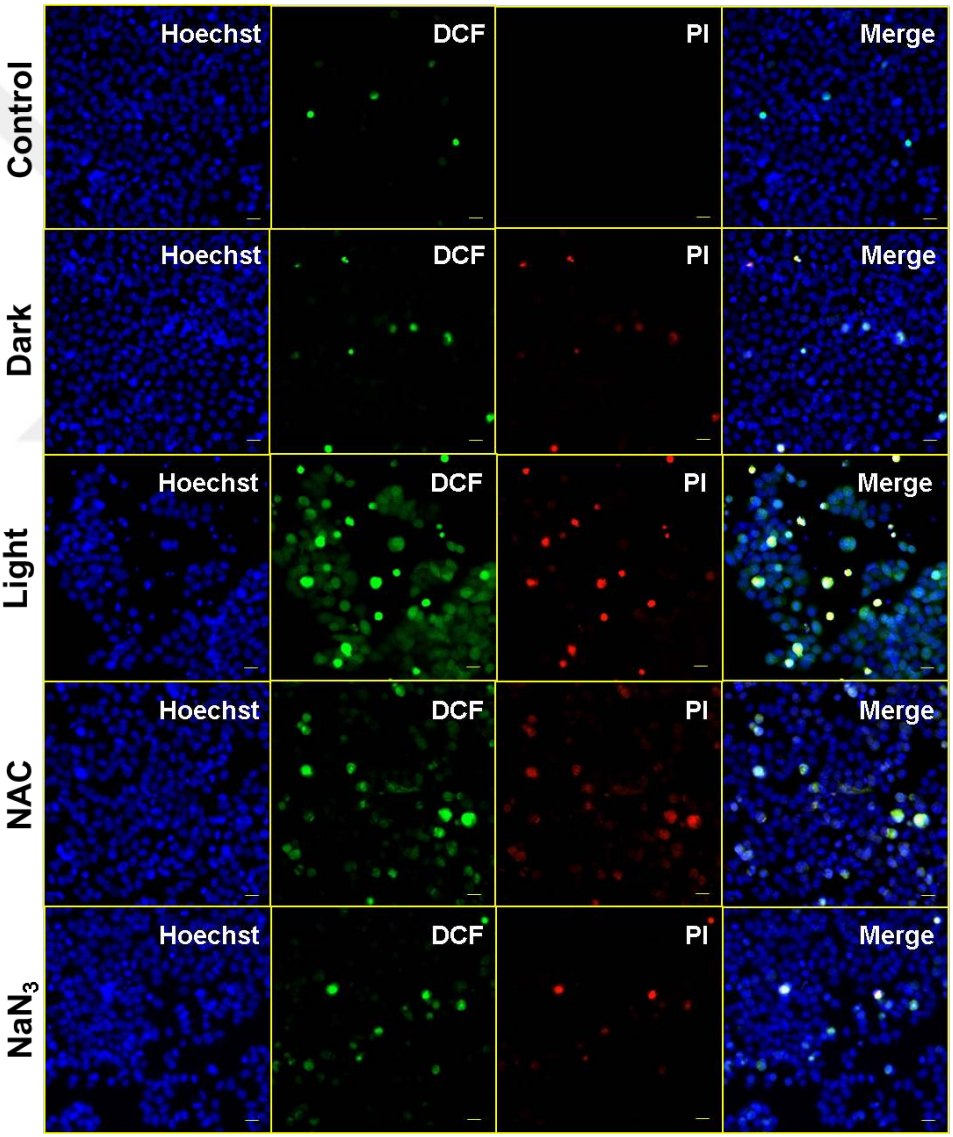

Figure 3.20 Images of triple Hoechst/DCF-DA/PI staining of HCT-116 treated with IC_{50} (6.33 µM) value of **TM-I-H_2S for** 4 h at dark then 2h with LED light (595 nm 9.83 mw/cm^2) in the presence or absence of NAC (5 mM), NaN_3 (10 mM). Blue:Hoechst 33342, Green: DCF, red: PI. DCF: 2′− 7′- dichlorofluorescein, PI: Propium iodide. Scale bar: 20 µm.

production and red emission shows cell death. In figure 3.20, green emission after light irradiation indicates ROS production and red emission indicates consequent cell death.

On the other hand, there is no significant signal in the cells without light. Also, use of ROS scavengers NaN_3 and NAC results in fading of both green and red emission meaning ROS production is responsible for cell death (Figure 3.20).[119]

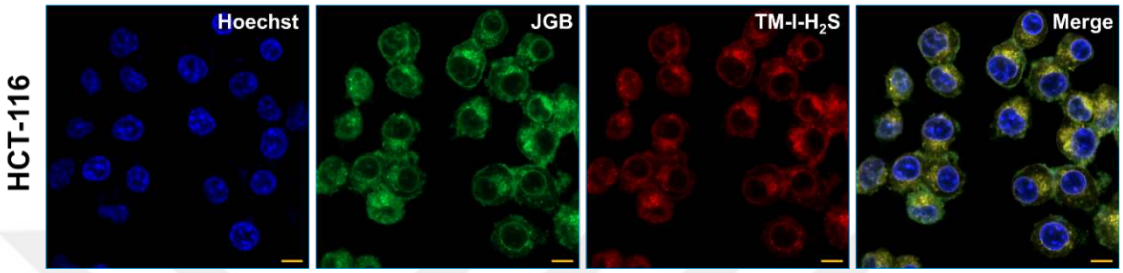

Figure 3.21 Cellular internalization of TM-I-H_2S (1 μM, 4 h) in HCT-116 cancer cells. Blue, Hoechst 33342; Green, Janus Green B; red, TM-I-H_2S. Scale bar: 10 μm.

As mentioned in the photophysical characterization section, **TM-I-H_2S** shows fluorescence in addition to singlet oxygen production. Accordingly, the fluorescent imaging potential of **TM-I-H_2S** was investigated in HCT-116 cells. The cells were incubated for 4 hours with **TM-I-H_2S** and washed with PBS. Also, nuclear staining Hoeschst and Mitochondrial staining Janus B Green (5 mM) were added.[121,122] Confocal microscope images indicates that red emission from **TM-I-H_2S** is in great match with green emission from Janus B Green (Figure 3.21). That is, **TM-I-H_2S** shows localization and activation in mitochondria. This can be explained by the high level of H_2S in the mitochondria of the cancerous cell. As a result, **TM-I-H_2S** has been shown to be an activatable and mitochondria- localized theranostic agent.

Chapter 4:

CONCLUSION

To close, in this study, iodinated silicon-fluorescein **(SF-I)** and iodinated Tokyo Magenta **(TM-I-H_2S)** were introduced as effective red-shifted theranostic agents at physiological conditions for the first time. **SF-I** showed high $^1O_2$ quantum yields under both 595 and 630 nm irradiations, and its cytotoxicity was evaluated in two cancer cells (HCT-116, TNBC MDA-MB-231) with limited chemotherapy options. Result of *in vitro* cell culture experiment clearly shoved that **SF-I** can induce cell death as a consequence of effective PDT action and can still act as a fluorophore at the same time. Therefore, **SF-I** possesses desirable properties toward the realization of image-guided PDT applications as a new class of easily accessible photosensitizers. Also, **SF-I** addresses most of the chronic problems of the current PSs such as high-water solubility, high $^1O_2$ quantum yield in aqueous solutions, red-shifted absorption/emission signals, photostability, and negligible dark toxicity. Further modifications on **SF-I** core are highly applicable to improve its properties as theranostic agents. For example, different cage groups or targeting moieties as well as organelle directing units can be incorporated to the structure by substitution through phenolic groups to design highly effective cancer cell selective agents.

TM-I-H_2S is another highly promising phototheranostic agent introduced in this study. Tokyo Magenta **(TM)**, which possesses appealing properties as fluorescent imaging agent was converted into theranostic agent by modifying structure with iodine and a H_2S cleavable cage group. This is the first example of activatable silicon xanthene based phototheranostic agent with high singlet oxygen quantum yield (34%) and fluorescence quantum yield (34%) through activation with H_2S under both 595 nm light irradiation. Further phototheranostic efficiency of **TM-I-H_2S** was studied in two cell lines (HCT-116, MDA-MB-231) and found to demonstrate phototheranostic effect in these cells.

TM-I-H_2S also has appealing properties as theranostic agent such as high-water solubility, high $^1O_2$ quantum yield in aqueous solutions, red-shifted absorption/emission signals, photostability, and negligible dark toxicity just like **SF-I.** Additionally, **TM-I-H_2S** is expected to be selective toward cancer cells with higher H_2S level compared to healthy cells. It is also possible to modify structure with different cage groups or targeting

moieties to employ its activity in different cancer types. All in all, novel phototheranostic agents holding great promise with highly appealing properties in cancer therapy were developed in the scope of this study.

BIBLIOGRAPHY

(1) Senga, S. S.; Grose, R. P. Hallmarks of Cancer - The New Testament: Expanding the Hallmarks of Cancer. *Open Biol.* **2021**, *11* (1).

(2) Lau, A. N.; vander Heiden, M. G. Metabolism in the Tumor Microenvironment. *Annu. Rev. Cancer Biol* **2019**, *2020*, 17–40.

(3) Quail, D. F.; Joyce, J. A. Microenvironmental Regulation of Tumor Progression and Metastasis. *Nat. Med.* **2013**, *19* (11), 1423–1437.

(4) Desai, T. J. Developmental Insights into Lung Cancer. *Annu. Rev. Cancer Biol. 2021* **2021**, *5*, 351–369.

(5) Abbas, Z.; Rehman, S. An Overview of Cancer Treatment Modalities. In *Neoplasm*; InTech, 2018. https://doi.org/10.5772/intechopen.76558.

(6) Ames, B. N.; Gold, L. S.; Willett, W. C. The Causes and Prevention of Cancer. *Proc. Natl. Acad. Sci. U.S.A.* **1995**, *92* (12), 5258–5265.

(7) Ferlay, J.; Colombet, M.; Soerjomataram, I.; Mathers, C.; Parkin, D. M.; Piñeros, M.; Znaor, A.; Bray, F. Estimating the Global Cancer Incidence and Mortality in 2018: GLOBOCAN Sources and Methods. *Int.J. Cancer* **2019**, *144* (8), 1941–1953.

(8) Bray, F.; Ferlay, J.; Soerjomataram, I.; Siegel, R. L.; Torre, L. A.; Jemal, A. Global Cancer Statistics 2018: GLOBOCAN Estimates of Incidence and Mortality Worldwide for 36 Cancers in 185 Countries. *CA: Cancer J. Clin.* **2018**, *68* (6), 394–424.

(9) Ferlay, J.; Soerjomataram, I.; Dikshit, R.; Eser, S.; Mathers, C.; Rebelo, M.; Parkin, D. M.; Forman, D.; Bray, F. Cancer Incidence and Mortality Worldwide: Sources, Methods and Major Patterns in GLOBOCAN 2012. *Int. J. Cancer* **2015**, *136* (5), E359–E386.

(10) Weigelt, B.; Peterse, J. L.; Van't Veer, L. J. Breast Cancer Metastasis: Markers and Models. *Nat. Rev. Cancer* **2005**, *5* (8), 591–602.

(11) Steeg, P. S. Targeting Metastasis. *Nat. Rev. Cancer* **2016**, *16* (4), 201–218.

(12) Sounni, N. E.; Noel, A. Targeting the Tumor Microenvironment for Cancer Therapy. *Clin. Chem.* **2013**, *59* (1), 85–93.

(13) Palucka, K.; Banchereau, J. Cancer Immunotherapy via Dendritic Cells. *Nat. Rev.Cancer* **2012**, *12* (4), 265–277.

(14) Wu, H.-C.; Chang, D.-K.; Huang, C.-T. Targeted Therapy for Cancer. *J. Cancer Mol.* **2006**, *2* (2), 57–66.

(15) Wagner, A.; Ploder, O.; Enislidis, G.; Truppe, M.; Ewers, R. Virtual Image Guided Navigation in Tumor Surgery - Technical Innovation. *J. Craniomaxillofac. Surg.* **1995**, *23* (5), 271–273.

(16) Delaney, G.; Jacob, S.; Featherstone, C.; Barton, M. The Role of Radiotherapy in Cancer Treatment: Estimating Optimal Utilization from a Review of Evidence-Based Clinical Guidelines. *Cancer* **2005**, *104* (6), 1129–1137.

(17) Baskar, R.; Lee, K. A.; Yeo, R.; Yeoh, K. W. Cancer and Radiation Therapy: Current Advances and Future Directions. *Int. J. Med.l Sci.* **2012**, *9* (3), 193–199.

(18) Andrews, D. W.; Scott, C. B.; Sperduto, P. W.; Flanders, A. E.; Gaspar, L. E.; Schell, M. C.; Werner-Wasik, M.; Demas, W.; Ryu, J.; Bahary, J. P.; Souhami, L.; Rotman, M.; Mehta, M. P.; Curran, W. J. Whole Brain Radiation Therapy with or without Stereotactic Radiosurgery Boost for Patients with One to Three Brain Metastases: Phase III Results of the RTOG 9508 Randomised Trial. *Lancet* **2004**, *363* (9422), 1665–1672.

(19) DeVita, V. T.; Chu, E. A History of Cancer Chemotherapy. *Cancer Res.* **2008**, *68* (21), 8643–8653.

(20) Aslam, M. S.; Naveed, S.; Ahmed, A.; Abbas, Z.; Gull, I.; Athar, M. A. Side Effects of Chemotherapy in Cancer Patients and Evaluation of Patients Opinion about Starvation Based Differential Chemotherapy. *J. Cancer Therapy* **2014**, *05* (08), 817–822.

(21) Felsher, D. W. Cancer Revoked: Oncogenes as Therapeutic Targets. *Nat. Rev. Cancer* **2003**, *3* (5), 375–380.

(22) Perillo, B.; di Donato, M.; Pezone, A.; di Zazzo, E.; Giovannelli, P.; Galasso, G.; Castoria, G.; Migliaccio, A. ROS in Cancer Therapy: The Bright Side of the Moon. *Exp. Mol. Med.* **2020**, *52* (2), 192–203.

(23) Zhang, J.; Ning, L.; Huang, J.; Zhang, C.; Pu, K. Activatable Molecular Agents for Cancer Theranostics. *Chem. Sci.* **2020**, *11* (3), 618–630.

(24) Dolmans, D. E. J. G. J.; Fukumura, D.; Jain, R. K. Photodynamic Therapy for Cancer. *Nat. Rev. Cancer* **2003**, *3* (5), 380–387.

(25) Shi, H.; Sadler, P. J. How Promising Is Phototherapy for Cancer? *Br. J. Cancer* **2020**, *123* (6), 871–873.

(26) Wilson, B. C. Photodynamic Therapy for Cancer: Principles. *Can. J. Gastroenterol.* **2002**, *16* (6), 393–396.

(27) Agostinis, P.; Berg, K.; Cengel, K. A.; Foster, T. H.; Girotti, A. W.; Gollnick, S. O.; Hahn, S. M.; Hamblin, M. R.; Juzeniene, A.; Kessel, D.; Korbelik, M.; Moan, J.; Mroz, P.; Nowis, D.; Piette, J.; Wilson, B. C.; Golab, J. Photodynamic Therapy of Cancer: An Update. *CA: Cancer J. Clin.* **2011**, *61* (4), 250–281.

(28) Baskaran, R.; Lee, J.; Yang, S. G. Clinical Development of Photodynamic Agents and Therapeutic Applications. *Biomater. Res.* **2018**, *22* (1), 1–8.

(29) v. Tappeiner, H. Ueber Die Wirkung Fluorescirender Substanzen Auf Fermente Und Toxine. *Berichte der deutschen chemischen Gesellschaft* **1903**, *36* (3), 3035–3038. https://doi.org/10.1002/cber.19030360370.

(30) Istomin, Y. P.; Alexandrova, E. N.; Zhavrid, E. A.; Voropay, E. S.; Samtsov, M. P.; Kaplevsky, K. N.; Lugovsky, A. P.; Lugovsky, A. A. The Effect of Hypoxia on Photocytotoxicity of TICS Tricarbocyanine Dye In Vitro. *Exp. Oncol.* **2006**, *28* (1), 80–82.

(31) Lan, M.; Zhao, S.; Liu, W.; Lee, C. S.; Zhang, W.; Wang, P. Photosensitizers for Photodynamic Therapy. *Adv. Healthcare Mater.* **2019**, *8* (13), 1900132.

(32) Mallidi, S.; Anbil, S.; Bulin, A. L.; Obaid, G.; Ichikawa, M.; Hasan, T. Beyond the Barriers of Light Penetration: Strategies, Perspectives and Possibilities for Photodynamic Therapy. *Theranostics* **2016**, *6* (13), 2458–2487.

(33) Stolik, S.; Delgado, J. A.; Pérez, A.; Anasagasti, L. Measurement of the Penetration Depths of Red and near Infrared Light in Human ″ex Vivo″ Tissues. *J. Photochem. Photobiol. B* **2000**, *57* (2–3), 90–93.

(34) Wilson, W. R.; Hay, M. P. Targeting Hypoxia in Cancer Therapy. *Nat. Rev. Cancer* **2011**, *11* (6), 393–410.

(35) Gilkes, D. M.; Semenza, G. L.; Wirtz, D. Hypoxia and the Extracellular Matrix: Drivers of Tumour Metastasis. *Nat. Rev. Cancer* **2014**, *14* (6), 430–439.

(36) Cosse, J.-P.; Michiels, C. Tumour Hypoxia Affects the Responsiveness of Cancer Cells to Chemotherapy and Promotes Cancer Progression. *Anti-Cancer Agents Med. Chem.* **2012**, *8* (7), 790–797.

(37) Zhou, Z.; Song, J.; Tian, R.; Yang, Z.; Yu, G.; Lin, L.; Zhang, G.; Fan, W.; Zhang, F.; Niu, G.; Nie, L.; Chen, X. Activatable Singlet Oxygen Generation from Lipid Hydroperoxide Nanoparticles for Cancer Therapy. *Angew. Chem. Int. Ed.* **2017**, *56* (23), 6492–6496.

(38) Liu, Y.; Jiang, Y.; Zhang, M.; Tang, Z.; He, M.; Bu, W. Modulating Hypoxia via Nanomaterials Chemistry for Efficient Treatment of Solid Tumors. *Acc. Chem. Res.* **2018**, *51* (10), 2502–2511.

(39) Tian, H.; Luo, Z.; Liu, L.; Zheng, M.; Chen, Z.; Ma, A.; Liang, R.; Han, Z.; Lu, C.; Cai, L. Cancer Cell Membrane-Biomimetic Oxygen Nanocarrier for Breaking Hypoxia-Induced Chemoresistance. *Adv.Funct.l Mater.* **2017**, *27* (38), 1703197.

(40) Pan, G. Y.; Jia, H. R.; Zhu, Y. X.; Wang, R. H.; Wu, F. G.; Chen, Z. Dual Channel Activatable Cyanine Dye for Mitochondrial Imaging and Mitochondria-Targeted Cancer Theranostics. *ACS Biomater. Sci. Eng.* **2017**, *3* (12), 3596–3606.

(41) Liu, H. W.; Hu, X. X.; Li, K.; Liu, Y.; Rong, Q.; Zhu, L.; Yuan, L.; Qu, F. L.; Zhang, X. B.; Tan, W. A Mitochondrial-Targeted Prodrug for NIR Imaging Guided and Synergetic NIR Photodynamic-Chemo Cancer Therapy. *Chem. Sci.* **2017**, *8* (11), 7689–7695.

(42) Jung, H. S.; Lee, J. H.; Kim, K.; Koo, S.; Verwilst, P.; Sessler, J. L.; Kang, C.; Kim, J. S. A Mitochondria-Targeted Cryptocyanine-Based Photothermogenic Photosensitizer. *J. Am. Chem. Soc.* **2017**, *139* (29), 9972–9978.

(43) Noh, I.; Lee, D.; Kim, H.; Jeong, C.-U.; Lee, Y.; Ahn, J.-O.; Hyun, H.; Park, J.-H.; Kim, Y.-C. Enhanced Photodynamic Cancer Treatment by Mitochondria-Targeting and Brominated Near-Infrared Fluorophores. *Adv. Sci.* **2018**, *5* (3), 1700481.

(44) Lv, W.; Zhang, Z.; Zhang, K. Y.; Yang, H.; Liu, S.; Xu, A.; Guo, S.; Zhao, Q.; Huang, W. A Mitochondria-Targeted Photosensitizer Showing Improved Photodynamic Therapy Effects Under Hypoxia. *Angew. Chem.* **2016**, *128* (34), 10101–10105.

(45) Handy, D. E.; Loscalzo, J. Redox Regulation of Mitochondrial Function. *Antiox. Redox Sign.* **2012**, *16* (11), 1323–1367.

(46) Giampazolias, E.; Tait, S. W. G. Mitochondria and the Hallmarks of Cancer. *FEBS J.* **2016**, *283* (5), 803–814.

(47) Weinberg, S. E.; Chandel, N. S. Targeting Mitochondria Metabolism for Cancer Therapy. *Nat. Chem. Biol.* **2015**, *11* (1), 9–15.

(48) D'Souza, G. G. M.; Wagle, M. A.; Saxena, V.; Shah, A. Approaches for Targeting Mitochondria in Cancer Therapy. *Biochim. Biophys. Acta Bioenerg.* **2011**, *1807* (6), 689–696.

(49) Zielonka, J.; Joseph, J.; Sikora, A.; Hardy, M.; Ouari, O.; Vasquez-Vivar, J.; Cheng, G.; Lopez, M.; Kalyanaraman, B. Mitochondria-Targeted Triphenylphosphonium-Based Compounds: Syntheses, Mechanisms of Action, and Therapeutic and Diagnostic Applications. *Chem.Rev.* **2017**, *117* (15), 10043–10120.

(50) Tan, X.; Luo, S.; Long, L.; Wang, Y.; Wang, D.; Fang, S.; Ouyang, Q.; Su, Y.; Cheng, T.; Shi, C. Structure-Guided Design and Synthesis of a Mitochondria-Targeting Near-Infrared Fluorophore with Multimodal Therapeutic Activities. *Adv. Mater.* **2017**, *29* (43), 1704196.

(51) Zhao, X.; Yang, Y.; Yu, Y.; Guo, S.; Wang, W.; Zhu, S. A Cyanine-Derivative Photosensitizer with Enhanced Photostability for Mitochondria-Targeted Photodynamic Therapy. *Chem. Commun.* **2019**, *55* (90), 13542–13545.

(52) Karaman, O.; Almammadov, T.; Emre Gedik, M.; Gunaydin, G.; Kolemen, S.; Gunbas, G. Mitochondria-Targeting Selenophene-Modified BODIPY-Based Photosensitizers for the Treatment of Hypoxic Cancer Cells. *ChemMedChem* **2019**, *14* (22), 1879–1886.

(53) Lv, W.; Zhang, Z.; Zhang, K. Y.; Yang, H.; Liu, S.; Xu, A.; Guo, S.; Zhao, Q.; Huang, W. A Mitochondria-Targeted Photosensitizer Showing Improved Photodynamic Therapy Effects Under Hypoxia. *Angew. Chem.* **2016**, *128* (34), 10101–10105.

(54) Simões, J. C. S.; Sarpaki, S.; Papadimitroulas, P.; Therrien, B.; Loudos, G. Conjugated Photosensitizers for Imaging and PDT in Cancer Research. *J. Med. Chem.* **2020**, *63* (23), 14119–14150.

(55) Fan, W.; Huang, P.; Chen, X. Overcoming the Achilles' Heel of Photodynamic Therapy. *Chem. Soc. Rev.* **2016**, *45* (23), 6488–6519.

(56) Kwiatkowski, S.; Knap, B.; Przystupski, D.; Saczko, J.; Kędzierska, E.; Knap-Czop, K.; Kotlińska, J.; Michel, O.; Kotowski, K.; Kulbacka, J. Photodynamic

Therapy – Mechanisms, Photosensitizers and Combinations. *Biomed. Pharmacother.* **2018**, *106*, 1098–1107.

(57) Aubry, J. M.; Pierlot, C.; Rigaudy, J.; Schmidt, R. Reversible Binding of Oxygen to Aromatic Compounds. *Acc. Chem. Res.* **2003**, *36* (9), 668–675.

(58) di Mascio, P.; Martinez, G. R.; Miyamoto, S.; Ronsein, G. E.; Medeiros, M. H. G.; Cadet, J. Singlet Molecular Oxygen Reactions with Nucleic Acids, Lipids, and Proteins. *Chem. Rev.* **2019**, *119* (3), 2043–2086.

(59) Gorman, A.; Killoran, J.; O'Shea, C.; Kenna, T.; Gallagher, W. M.; O'Shea, D. F. In Vitro Demonstration of the Heavy-Atom Effect for Photodynamic Therapy. *J. Am. Chem. Soc.* **2004**, *126* (34), 10619–10631. https://doi.org/10.1021/ja047649e.

(60) Ji, S.; Ge, J.; Escudero, D.; Wang, Z.; Zhao, J.; Jacquemin, D. Molecular Structure-Intersystem Crossing Relationship of Heavy-Atom-Free Bodipy Triplet Photosensitizers. *J. Org. Chem.* **2015**, *80* (11), 5958–5963.

(61) Ji, S.; Ge, J.; Escudero, D.; Wang, Z.; Zhao, J.; Jacquemin, D. Molecular Structure−Intersystem Crossing Relationship of Heavy-Atom-Free BODIPY Triplet Photosensitizers Scheme 1. Compounds Used in This Study. *J. Org. Chem* **2015**, *80*, 5963.

(62) Chou, P. T.; Chi, Y.; Chung, M. W.; Lin, C. C. Harvesting Luminescence via Harnessing the Photophysical Properties of Transition Metal Complexes. *Coord. Chem. Rev.* **2011**, *255* (21–22), 2653–2665.

(63) Gunduz, H.; Bilici, K.; Cetin, S.; Muti, A.; Sennaroglu, A.; Acar, H. Y.; Kolemen, S. Dual Laser Activatable Brominated Hemicyanine as a Highly Efficient and Photostable Multimodal Phototherapy Agent. *J. Photochem. Photobiol. B* **2021**, 112171.

(64) Almammadov, T.; Atakan, G.; Leylek, O.; Ozcan, G.; Gunbas, G.; Kolemen, S. Resorufin Enters the Photodynamic Therapy Arena: A Monoamine Oxidase Activatable Agent for Selective Cytotoxicity. *ACS Med. Chem. Lett.* **2020**, *11*, 2491–2496.

(65) Beharry, A. A. Next-Generation Photodynamic Therapy: New Probes for Cancer Imaging and Treatment. *Biochemistry* **2018**, *57* (2), 173–174.

(66) Lan, M.; Zhao, S.; Liu, W.; Lee, C. S.; Zhang, W.; Wang, P. Photosensitizers for Photodynamic Therapy. *Advanced Healthcare Materials*. Wiley-VCH Verlag July 11, 2019. https://doi.org/10.1002/adhm.201900132.

(67) Abrahamse, H.; Hamblin, M. R. New Photosensitizers for Photodynamic Therapy. *Biochem. J.* **2016**, *473* (4), 347–364.

(68) Celli, J. P.; Spring, B. Q.; Rizvi, I.; Evans, C. L.; Samkoe, K. S.; Verma, S.; Pogue, B. W.; Hasan, T. Imaging and Photodynamic Therapy: Mechanisms, Monitoring, and Optimization. *Chem. Rev.* **2010**, *110* (5), 2795–2838.

(69) Chen, Y. Fluorescent Probes for Detection and Bioimaging of Leucine Aminopeptidase. *Materials Today Chemistry* **2020**, *15*.

(70) Gao, P.; Pan, W.; Li, N.; Tang, B. Fluorescent Probes for Organelle-Targeted Bioactive Species Imaging. *Chem. Sci.* **2019**, *10* (24), 6035–6071.

(71) Yang, K.; Kolanowski, J. L.; New, E. J. Mitochondrially Targeted Fluorescent Redox Sensors. *Interface Focus* **2017**, *7* (2).

(72) Yan, F.; Fan, K.; Bai, Z.; Zhang, R.; Zu, F.; Xu, J.; Li, X. Fluorescein Applications as Fluorescent Probes for the Detection of Analytes. *Trends Anal. Chem.* **2017**, *97*, 15–35.

(73) Yi, X.; Wang, F.; Qin, W.; Yang, X.; Yuan, J. Near-Infrared Fluorescent Probes in Cancer Imaging and Therapy: An Emerging Field. *Int. J. Nanomed.* **2014**.

(74) Lovell, J. F.; Liu, T. W. B.; Chen, J.; Zheng, G. Activatable Photosensitizers for Imaging and Therapy. *Chem. Rev.* **2010**, *110* (5), 2839–2857.

(75) Huang, J.; Pu, K. Activatable Molecular Probes for Second Near-Infrared Fluorescence, Chemiluminescence, and Photoacoustic Imaging. *Angew.Chem. Int. Ed.* **2020**, *59* (29), 11717–11731.

(76) Yuan, B.; Wang, H.; Xu, J. F.; Zhang, X. Activatable Photosensitizer for Smart Photodynamic Therapy Triggered by Reactive Oxygen Species in Tumor Cells. *ACS Appl. Mater. Inter.* **2020**, *12* (24), 26982–26990. https://doi.org/10.1021/acsami.0c07471.

(77) Esfahani, S. A.; Heidari, P.; Kucherlapati, M. H.; Ferrer, J. M.; Kucherlapati, R. S.; Mahmood, U. Optical Imaging with a Novel Cathepsin-Activatable Probe for Enhanced Detection of Colorectal Cancer. *Am J Nucl Med Mol Imaging* **2019**, *9* (5), 230–242.

(78) Luo, Z.; Huang, Z.; Li, K.; Sun, Y.; Lin, J.; Ye, D.; Chen, H. Y. Targeted Delivery of a γ-Glutamyl Transpeptidase Activatable Near-Infrared-Fluorescent Probe for Selective Cancer Imaging. *Anal. Chem.* **2018**, *90* (4), 2875–2883.

(79) Li, H.; Yao, Q.; Sun, W.; Shao, K.; Lu, Y.; Chung, J.; Kim, D.; Fan, J.; Long, S.; Du, J.; Li, Y.; Wang, J.; Yoon, J.; Peng, X. Aminopeptidase N Activatable Fluorescent Probe for Tracking Metastatic Cancer and Image-Guided Surgery via in Situ Spraying. *J. Am. Chem. Soc.* **2020**, *142* (13), 6381–6389.

(80) Luo, Z.; Feng, L.; An, R.; Duan, G.; Yan, R.; Shi, H.; He, J.; Zhou, Z.; Ji, C.; Chen, H.-Y.; Ye, D. Activatable Near-Infrared Probe for Fluorescence Imaging of γ-Glutamyl Transpeptidase in Tumor Cells and In Vivo. *Chem. Eur. J.* **2017**, *23* (59), 14778–14785.

(81) Yoon, J.; Jung, Y. J.; Yoon, J. B.; Damodar, K.; Kim, H.; Shin, M.; Seo, M.; Cho, D. W.; Lee, J. T.; Lee, J. K. The Heavy-Atom Effect on Xanthene Dyes for Photopolymerization by Visible Light. *Polym.Chem.* **2019**, *10* (42), 5737–5742.

(82) Wang, Q.; Xia, B.; Xu, J.; Niu, X.; Cai, J.; Shen, Q.; Wang, W.; Huang, W.; Fan, Q. Biocompatible Small Organic Molecule Phototheranostics for NIR-II Fluorescence/Photoacoustic Imaging and Simultaneous Photodynamic/Photothermal Combination Therapy. *Mater. Chem. Front.* **2019**, *3* (4), 650–655.

(83) Wang, Q.; Dai, Y.; Xu, J.; Cai, J.; Niu, X.; Zhang, L.; Chen, R.; Shen, Q.; Huang, W.; Fan, Q. All-in-One Phototheranostics: Single Laser Triggers NIR-II Fluorescence/Photoacoustic Imaging Guided Photothermal/Photodynamic/Chemo Combination Therapy. *Adv. Funct. Mater.* **2019**, *29* (31).

(84) Cai, Y.; Si, W.; Huang, W.; Chen, P.; Shao, J.; Dong, X. Organic Dye Based Nanoparticles for Cancer Phototheranostics. *Small* **2018**, *14* (25), 1704247.

(85) Gao, D.; Guo, X.; Zhang, X.; Chen, S.; Wang, Y.; Chen, T.; Huang, G.; Gao, Y.; Tian, Z.; Yang, Z. Multifunctional Phototheranostic Nanomedicine for Cancer Imaging and Treatment. *Mater. Today Bio* **2020**, *5*, 100035–100068.

(86) Xu, F.; Li, H.; Yao, Q.; Ge, H.; Fan, J.; Sun, W.; Wang, J.; Peng, X. Hypoxia-Activated NIR Photosensitizer Anchoring in the Mitochondria for Photodynamic Therapy. *Chem. Sci.* **2019**, *10* (45), 10586–10594.

(87) Zhao, X.; Yang, Y.; Yu, Y.; Guo, S.; Wang, W.; Zhu, S. A Cyanine-Derivative Photosensitizer with Enhanced Photostability for Mitochondria-Targeted Photodynamic Therapy. *Chem. Commun.* **2019**, *55* (90), 13542–13545.

(88) Baldes, E. J. The Photodynamic Properties of a Particular Hematoporphyrin Derivative. *Arch. Dermatol.* **1960**, *82* (4), 508–516.

(89) Dougherty, T. J.; Grindey, G. B.; Fiel, R.; Weishaupt, K. R.; Boyle, D. G. Photoradiation Therapy. II. Cure of Animal Tumors with Hematoporphyrin and Light. *J. Natl. Cancer Inst.* **1975**, *55* (1), 115–121.

(90) Kelly, J. F.; Snell, M. E.; Berenbauai, M. C. Photodynamic Destruction of Human Bladder Carcinoma. *Br. J. Cancer* **1975**, *31* (2), 237–244.

(91) Aveline, B. M.; Hasan, T.; Redmond, R. W. The Effects of Aggregation, Protein Binding and Cellular Incorporation on the Photophysical Properties of Benzoporphyrin Derivative Monoacid Ring A (BPDMA). *J. Photochem. Photobiol. B* **1995**, *30* (2–3), 161–169.

(92) Kiesslich, T.; Berlanda, J.; Plaetzer, K.; Krammer, B.; Berr, F. Comparative Characterization of the Efficiency and Cellular Pharmacokinetics of Foscan®- and Foslip®-Based Photodynamic Treatment in Human Biliary Tract Cancer Cell Lines. *Photochem. Photobiol. Sci.* **2007**, *6* (6), 619–627.

(93) Hongying, Y.; Fuyuan, W.; Zhiyi, Z. Photobleaching of Chlorins in Homogeneous and Heterogeneous Media. *Dyes Pigm.* **1999**, *43* (2), 109–117.

(94) Li, X.; Kolemen, S.; Yoon, J.; Akkaya, E. U. Activatable Photosensitizers: Agents for Selective Photodynamic Therapy. *Adv. Funct. Mater.* **2017**, *27* (1604053), 1604053–1604064.

(95) Sehgal, I.; Sibrian-Vazquez, M.; Vicente, M. G. H. Photoinduced Cytotoxicity and Biodistribution of Prostate Cancer Cell-Targeted Porphyrins. *J. Med. Chem.* **2008**, *51* (19), 6014–6020.

(96) Horiuchi, H.; Kuribara, R.; Hirabara, A.; Okutsu, T. PH-Response Optimization of Amino-Substituted Tetraphenylporphyrin Derivatives as PH-Activatable Photosensitizers. *J. Phys. Chem. A* **2016**, *120* (28), 5554–5561.

(97) He, H.; Lo, P. C.; Yeung, S. L.; Fong, W. P.; Ng, D. K. P. Preparation of Unsymmetrical Distyryl BODIPY Derivatives and Effects of the Styryl Substituents on Their in Vitro Photodynamic Properties. *Chem. Commun.* **2011**, *47* (16), 4748–4750.

(98) Lau, J. T. F.; Lo, P. C.; Jiang, X. J.; Wang, Q.; Ng, D. K. P. A Dual Activatable Photosensitizer toward Targeted Photodynamic Therapy. *J. Med. Chem.* **2014**, *57* (10), 4088–4097.

(99) Kamkaew, A.; Lim, S. H.; Lee, H. B.; Kiew, L. V.; Chung, L. Y.; Burgess, K. BODIPY Dyes in Photodynamic Therapy. *Chem. Soc. Rev.* **2013**, *42* (1), 77–88.

(100) Awuah, S. G.; You, Y. Boron Dipyrromethene (BODIPY)-Based Photosensitizers for Photodynamic Therapy. *RSC Adv.* **2012**, *2* (30), 11169–11183. https://doi.org/10.1039/c2ra21404k.

(101) Yogo, T.; Urano, Y.; Ishitsuka, Y.; Maniwa, F.; Nagano, T. Highly Efficient and Photostable Photosensitizer Based on BODIPY Chromophore. *J. Am. Chem. Soc.* **2005**, *127* (35), 12162–12163.

(102) He, H.; Lo, P. C.; Yeung, S. L.; Fong, W. P.; Ng, D. K. P. Preparation of Unsymmetrical Distyryl BODIPY Derivatives and Effects of the Styryl Substituents on Their in Vitro Photodynamic Properties. *Chem. Commun.* **2011**, *47* (16), 4748–4750.

(103) Umezawa, K.; Matsui, A.; Nakamura, Y.; Citterio, D.; Suzuki, K. Bright, Color-Tunable Fluorescent Dyes in the Vis/NIR Region: Establishment of New "Tailor-Made" Multicolor Fluorophores Based on Borondipyrromethene. *Chem. Eur. J.* **2009**, *15* (5), 1096–1106.

(104) Zhao, J.; Wu, W.; Sun, J.; Guo, S. Triplet Photosensitizers: From Molecular Design to Applications. *Chem. Soc. Rev.* **2013**, *42* (12), 5323–5351.

(105) Ramaiah, D.; Eckert, I.; Arun, K. T.; Weidenfeller, L.; Epe, B. Squaraine Dyes for Photodynamic Therapy: Study of Their Cytotoxicity and Genotoxicity in Bacteria and Mammalian Cells¶‡. *Photochem. Photobiol.* **2007**, *76* (6), 672–677.

(106) Ichikawa, Y.; Kamiya, M.; Obata, F.; Miura, M.; Terai, T.; Komatsu, T.; Ueno, T.; Hanaoka, K.; Nagano, T.; Urano, Y. Selective Ablation of β-Galactosidase-Expressing Cells with a Rationally Designed Activatable Photosensitizer. *Angew. Chem. Int. Ed.* **2014**, *53* (26), 6772–6775.

(107) Hellmich, M. R.; Szabo, C. Hydrogen Sulfide and Cancer. *Handb. Exp. Pharmacol.* **2015**, *230*, 233–241.

(108) Lin, V. S.; Chen, W.; Xian, M.; Chang, C. J. Chemical Probes for Molecular Imaging and Detection of Hydrogen Sulfide and Reactive Sulfur Species in Biological Systems. *Chem. Soc. Rev.* **2015**, *44* (14), 4596–4618.

(109) Velusamy, N.; Binoy, A.; Bobba, K. N.; Nedungadi, D.; Mishra, N.; Bhuniya, S. A Bioorthogonal Fluorescent Probe for Mitochondrial Hydrogen Sulfide: New Strategy for Cancer Cell Labeling. *Chem. Commun.* **2017**, *53* (62), 8802–8803.

(110) Hirabayashi, K.; Hanaoka, K.; Takayanagi, T.; Toki, Y.; Egawa, T.; Kamiya, M.; Komatsu, T.; Ueno, T.; Terai, T.; Yoshida, K.; Uchiyama, M.; Nagano, T.; Urano,

Y. Analysis of Chemical Equilibrium of Silicon-Substituted Fluorescein and Its Application to Develop a Scaffold for Red Fluorescent Probes. *Anal. Chem.* **2015**, *87*, 9061–9069.

(111) Cetin, S.; Elmazoglu, Z.; Karaman, O.; Gunduz, H.; Gunbas, G.; Kolemen, S. Balanced Intersystem Crossing in Iodinated Silicon-Fluoresceins Allows New Class of Red Shifted Theranostic Agents. *ACS Med. Chem. Lett.* **2021**. <https://pubs.acs.org/doi/abs/10.1021/acsmedchemlett.1c00018>

(112) Egawa, T.; Koide, Y.; Hanaoka, K.; Komatsu, T.; CooTeraiper, T.; Nagano, T. Development of a Fluorescein Analogue, TokyoMagenta, as a Novel Scaffold for Fluorescence Probes in Red Region. *Chem. Commun.* **2011**, *47* (14), 9971–9974.

(113) Grimm, J. B.; Brown, T. A.; Tkachuk, A. N.; Lavis, L. D. General Synthetic Method for Si-Fluoresceins and Si-Rhodamines. *ACS Cent. Sci.* **2017**, *3* (9), 975–985.

(114) Kushida, Y.; Nagano, T.; Hanaoka, K. Silicon-Substituted Xanthene Dyes and Their Applications in Bioimaging. *Analyst* **2015**, *140* (3), 685–695.

(115) Fernandez, J. M.; Bilgin, M. D.; Grossweiner, L. I. Singlet Oxygen Generation by Photodynamic Agents. *J. Photochem. Photobiol., B* **1997**, *37* (997), 13–140.

(116) Halder, A.; Jethwa, M.; Mukherjee, P.; Ghosh, S.; Das, S.; Helal Uddin, A. B. M.; Mukherjee, A.; Chatterji, U.; Roy, P. Lactoferrin-Tethered Betulinic Acid Nanoparticles Promote Rapid Delivery and Cell Death in Triple Negative Breast and Laryngeal Cancer Cells. *Artif. Cells Nanomed. Biotechnol.* **2020**, *48* (1), 1362–1371.

(117) Khan, K.; Valeri, N.; Dearman, C.; Rao, S.; Watkins, D.; Starling, N.; Chau, I.; Cunningham, D. Targeting EGFR Pathway in Metastatic Colorectal Cancer-Tumour Heterogeniety and Convergent Evolution. *Crit. Rev. Oncol. Hematol.* **2019**, *143*, 153–163.

(118) Yang, K.; Wen, J.; Chao, S.; Liu, J.; Yang, K.; Pei, Y.; Pei, Z. A Supramolecular Photosensitizer System Based on the Host-Guest Complexation between Water-Soluble Pillar[6]Arene and Methylene Blue for Durable Photodynamic Therapy. *Chem. Commun.* **2018**, *54* (46), 5911–5914.

(119) Kuimova, M. K.; Yahioglu, G.; Ogilby, P. R. Singlet Oxygen in a Cell: Spatially Dependent Lifetimes and Quenching Rate Constants. *J. Am. Chem. Soc.* **2009**, *131* (1), 332–340.

(120) Hartle, M. D.; Pluth, M. D. A Practical Guide to Working with H2S at the Interface of Chemistry and Biology. *Chem. Soc. Rev.* **2016**, *45* (22), 6108–6117.

(121) Cooperstein, S. J.; Lazarow, A. Studies on the Mechanism of Janus Green B Staining of Mitochondria. III. Reduction of Janus Green B by Isolated Enzyme Systems. *Exp. Cell. Res.* **1953**, *5* (1), 82–97.

(122) Ahmad, F.; Alamoudi, W.; Haque, S.; Salahuddin, M.; Alsamman, K. Simple, Reliable, and Time-Efficient Colorimetric Method for the Assessment of Mitochondrial Function and Toxicity. *Bosn. J. Basic Med. Sci.* **2018**, *18* (4), 367–374.

Appendix A: ^{1}H-NMR & ^{13}C-NMR SPECTRA

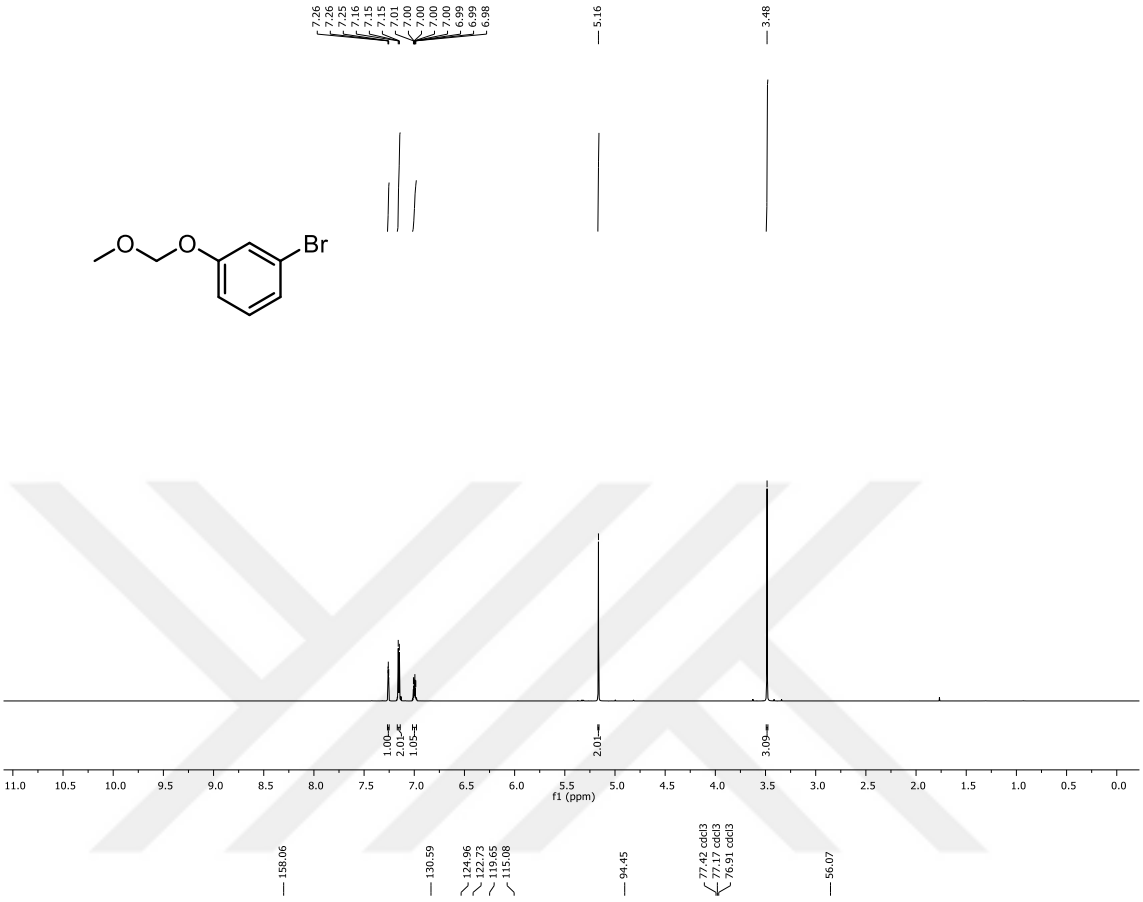

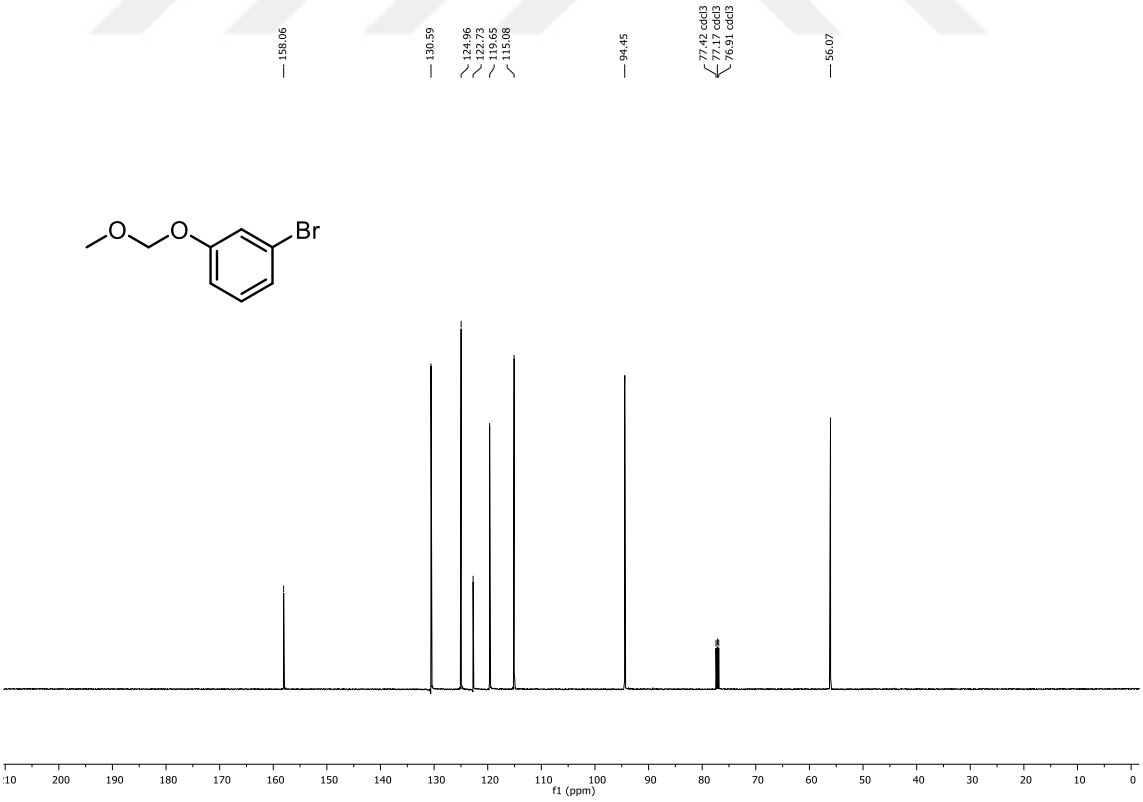

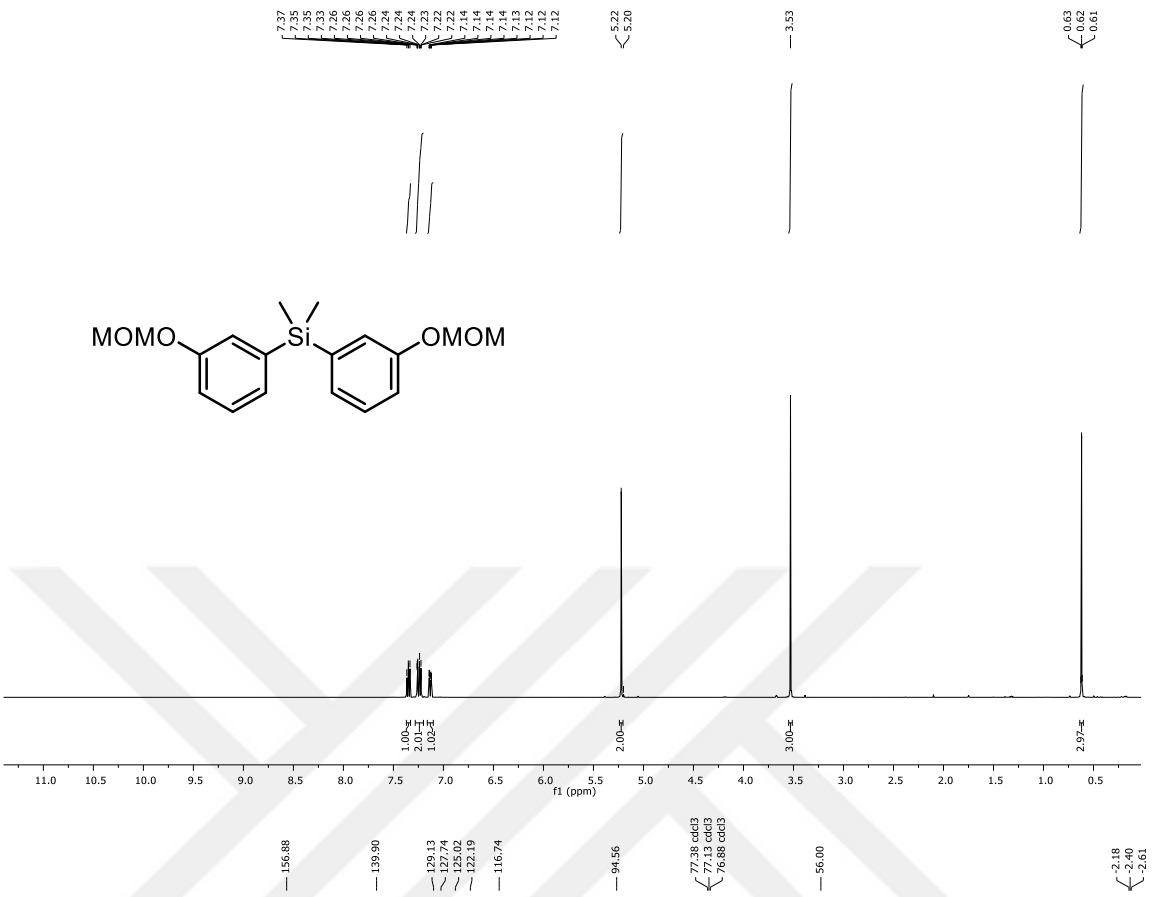
7.37
7.35
7.35
7.33
7.26
7.26
7.26
7.24
7.24
7.24
7.23
7.22
7.22
7.14
7.14
7.14
7.13
7.12
7.12
7.12
5.22
5.20
3.53
0.63
0.62
0.61
MOMO
Si
OMOM
1.00
2.01
1.02
2.00
3.00
2.97
f1 (ppm)

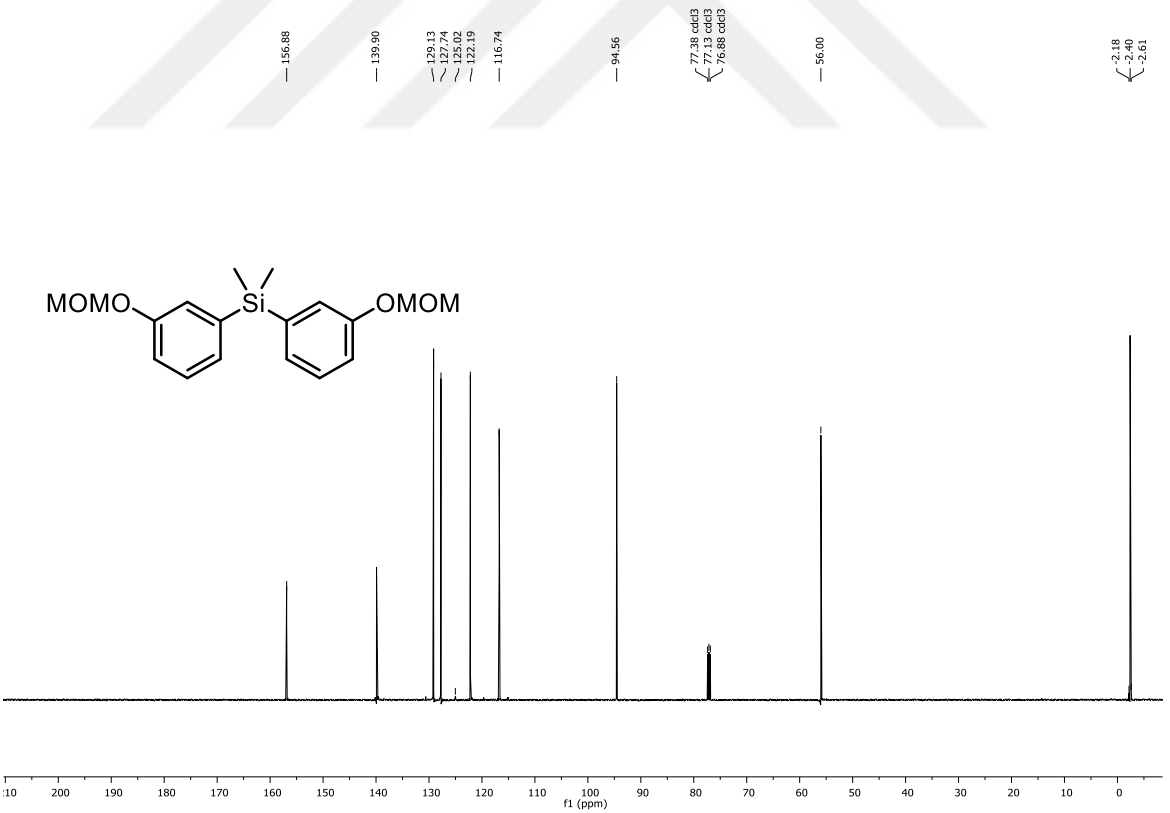
156.88
139.90
129.13
127.74
125.02
122.19
116.74
94.56
77.38 cdcl3
77.13 cdcl3
76.88 cdcl3
56.00
-2.18
-2.40
-2.61
MOMO
Si
OMOM
f1 (ppm)

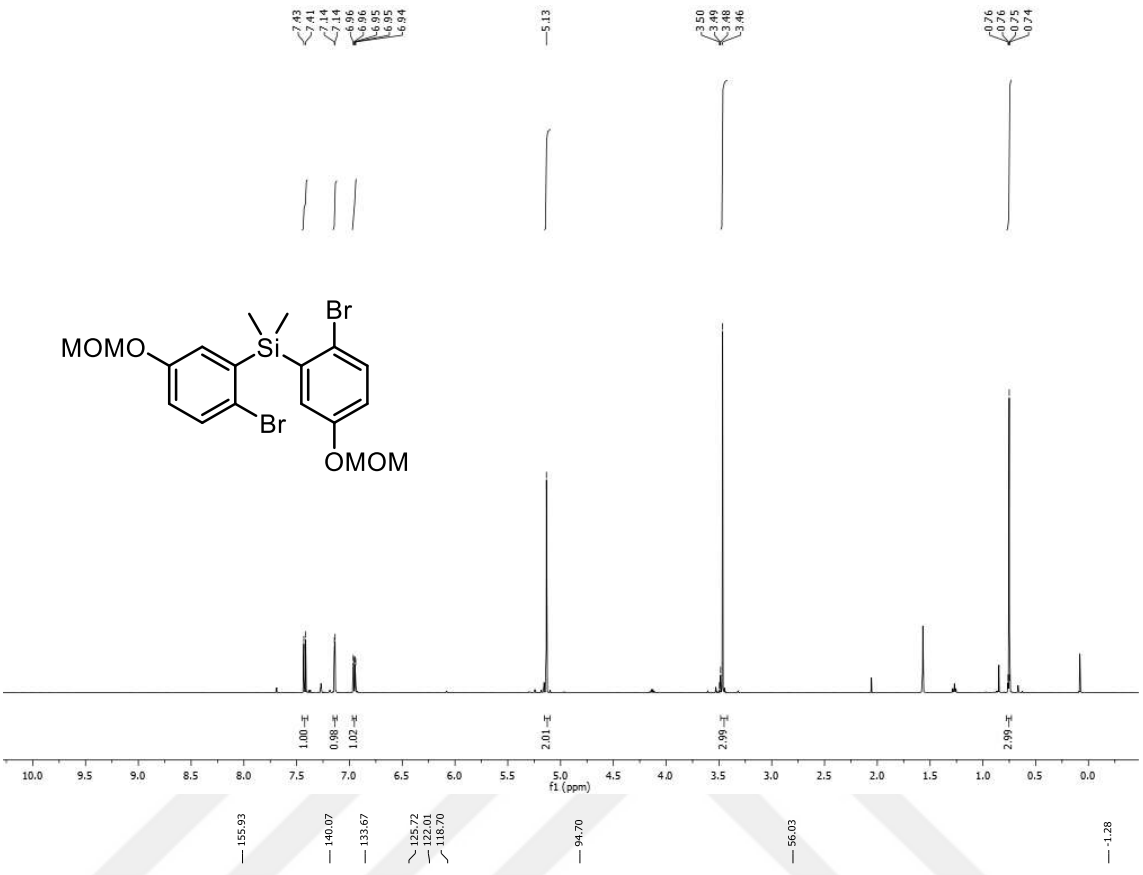
7.43
7.41
7.14
7.14
6.96
6.96
6.95
6.95
6.94
5.13
3.50
3.49
3.48
3.46
0.76
0.76
0.75
0.74
MOMO
Si
Br
Br
OMOM
1.00
0.98
1.02
2.01
2.99
2.99
f1 (ppm)

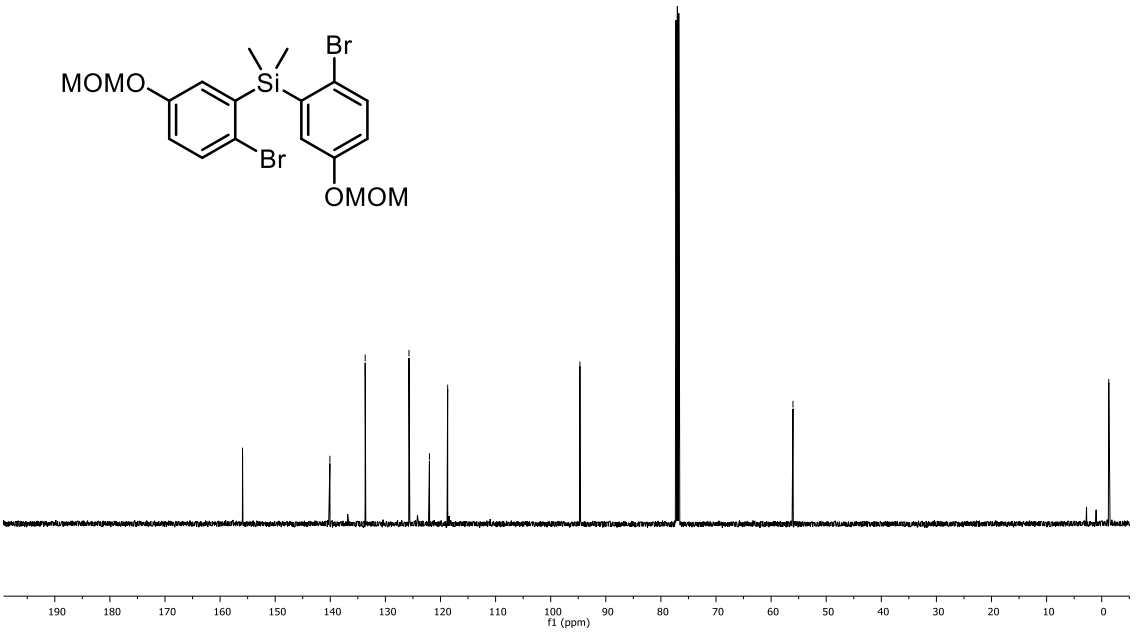
155.93
140.07
133.67
125.72
122.01
118.70
94.70
56.03
-1.28
MOMO
Si
Br
Br
OMOM
f1 (ppm)

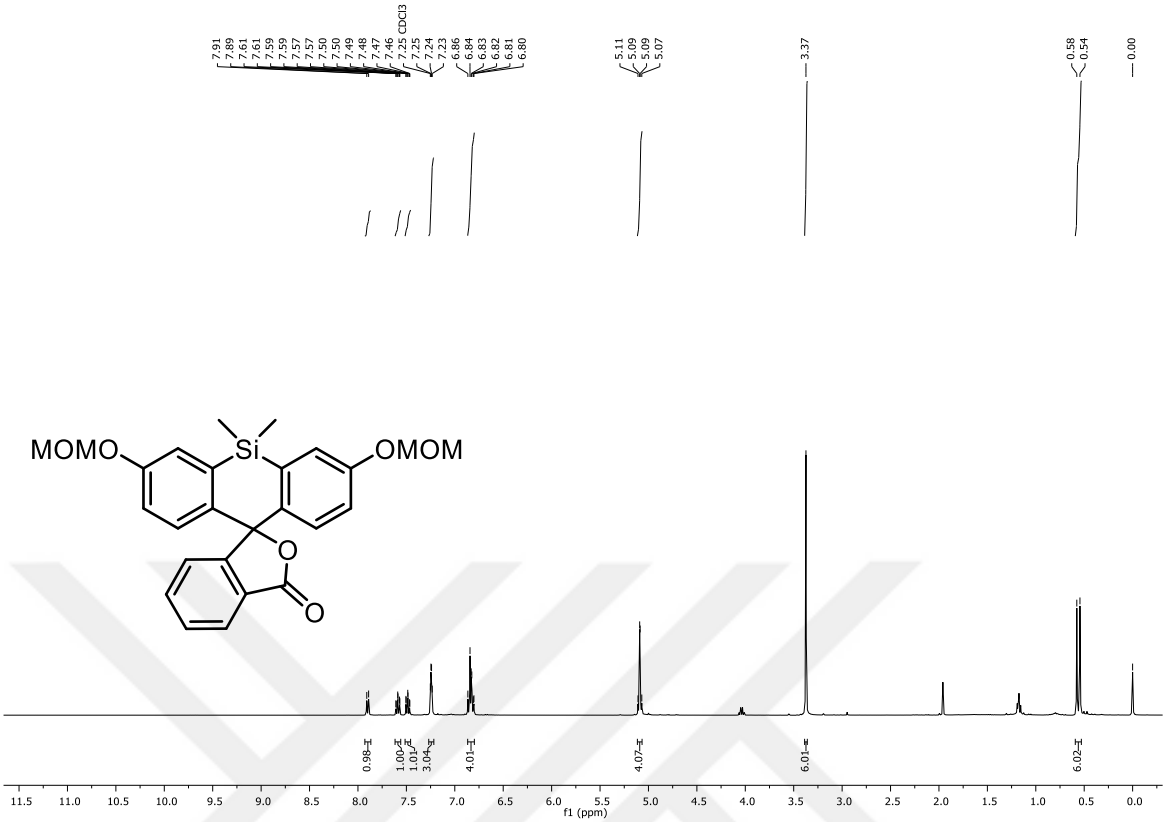
7.91
7.89
7.61
7.61
7.59
7.59
7.57
7.57
7.50
7.50
7.49
7.48
7.47
7.46
7.25 CDCl3
7.25
7.24
7.23
6.86
6.84
6.83
6.82
6.81
6.80
5.11
5.09
5.09
5.07
3.37
0.58
0.54
0.00
MOMO
Si
OMOM
O
O
0.98
1.00
1.01
3.04
4.01
4.07
6.01
6.02
f1 (ppm)

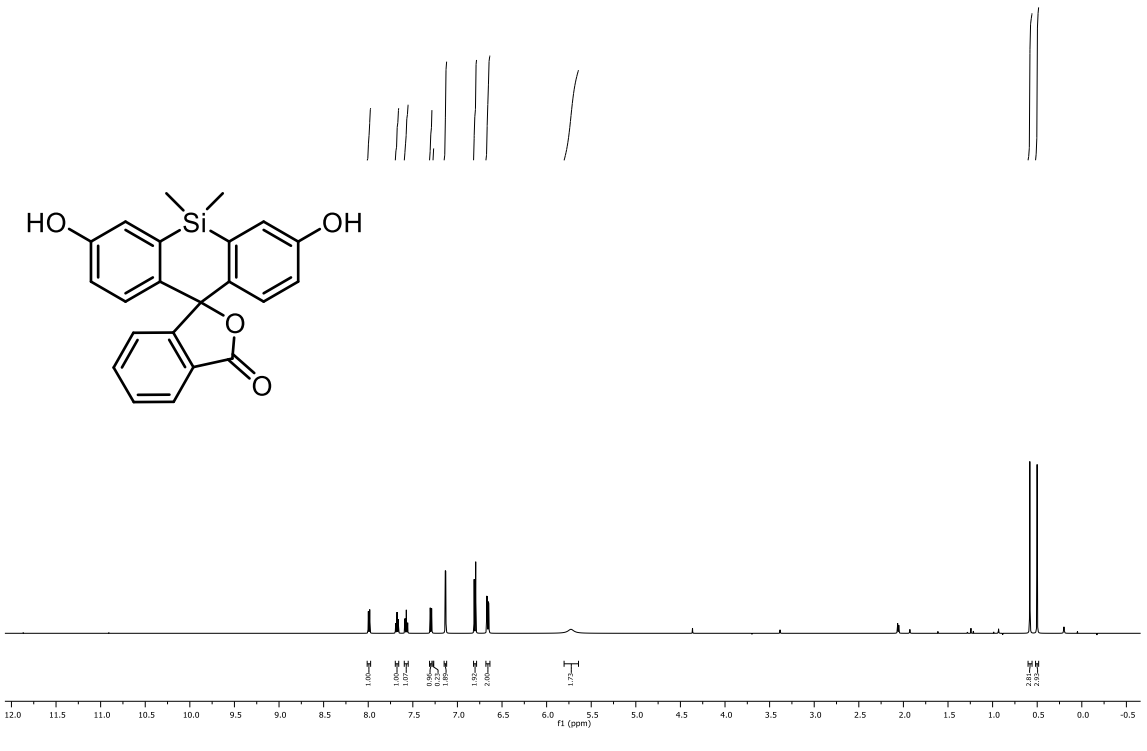
HO
Si
OH
O
O
1.00
1.00
0.96
0.23
1.00
1.93
2.00
1.75
2.81
2.03
f1 (ppm)

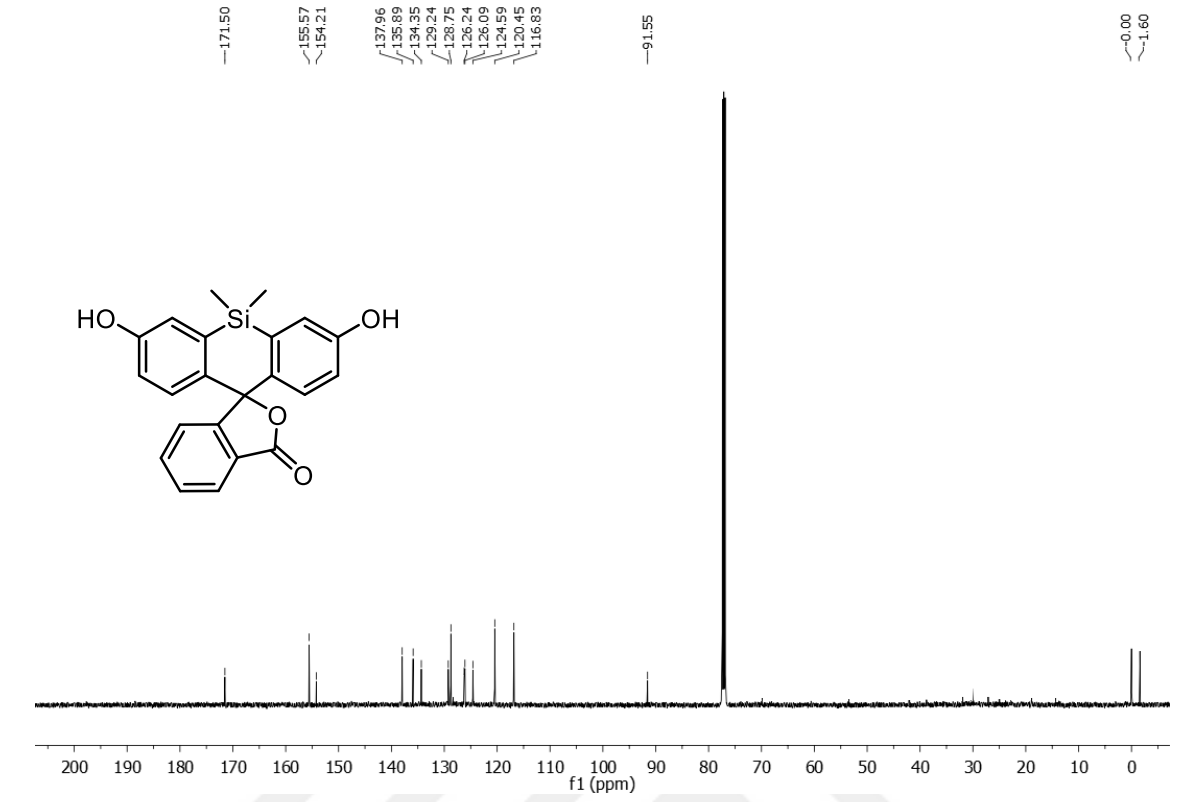
171.50
155.57
154.21
137.96
135.89
134.35
129.24
128.75
126.24
126.09
124.59
120.45
116.83
91.55
0.00
-1.60
HO
Si
OH
O
O
200 190 180 170 160 150 140 130 120 110 100 90 80 70 60 50 40 30 20 10 0
f1 (ppm)

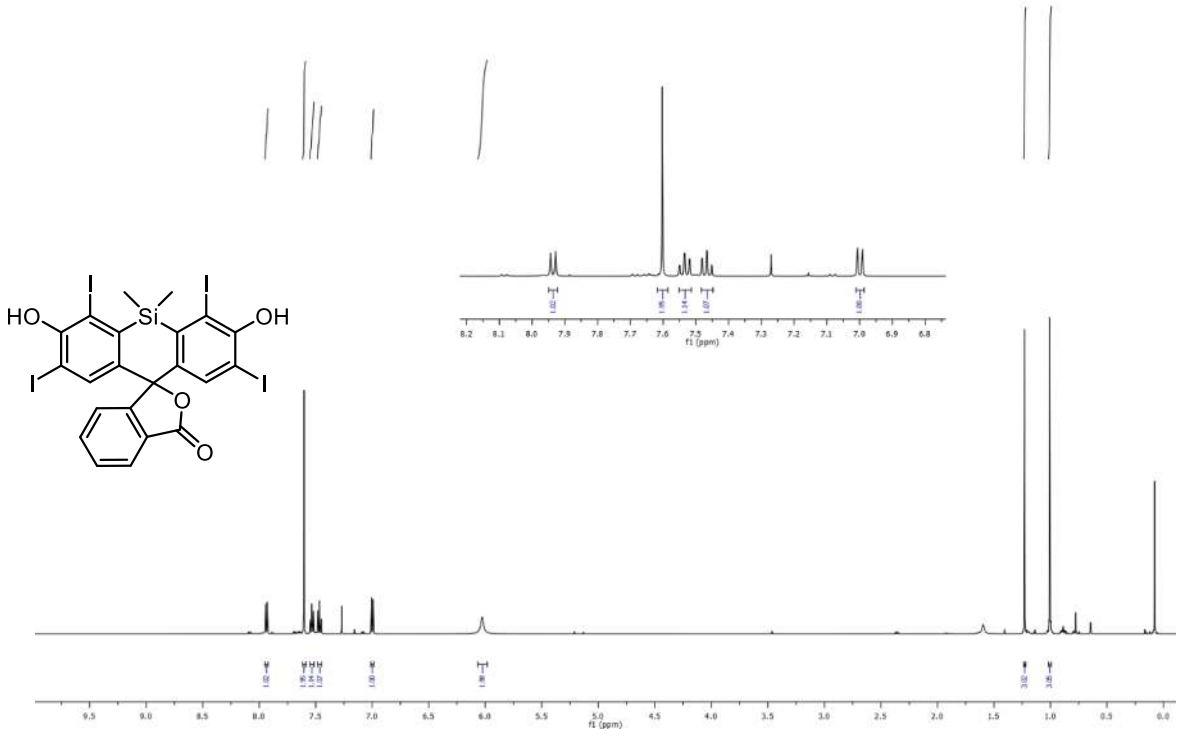
HO
Si
OH
O
O
f1 (ppm)

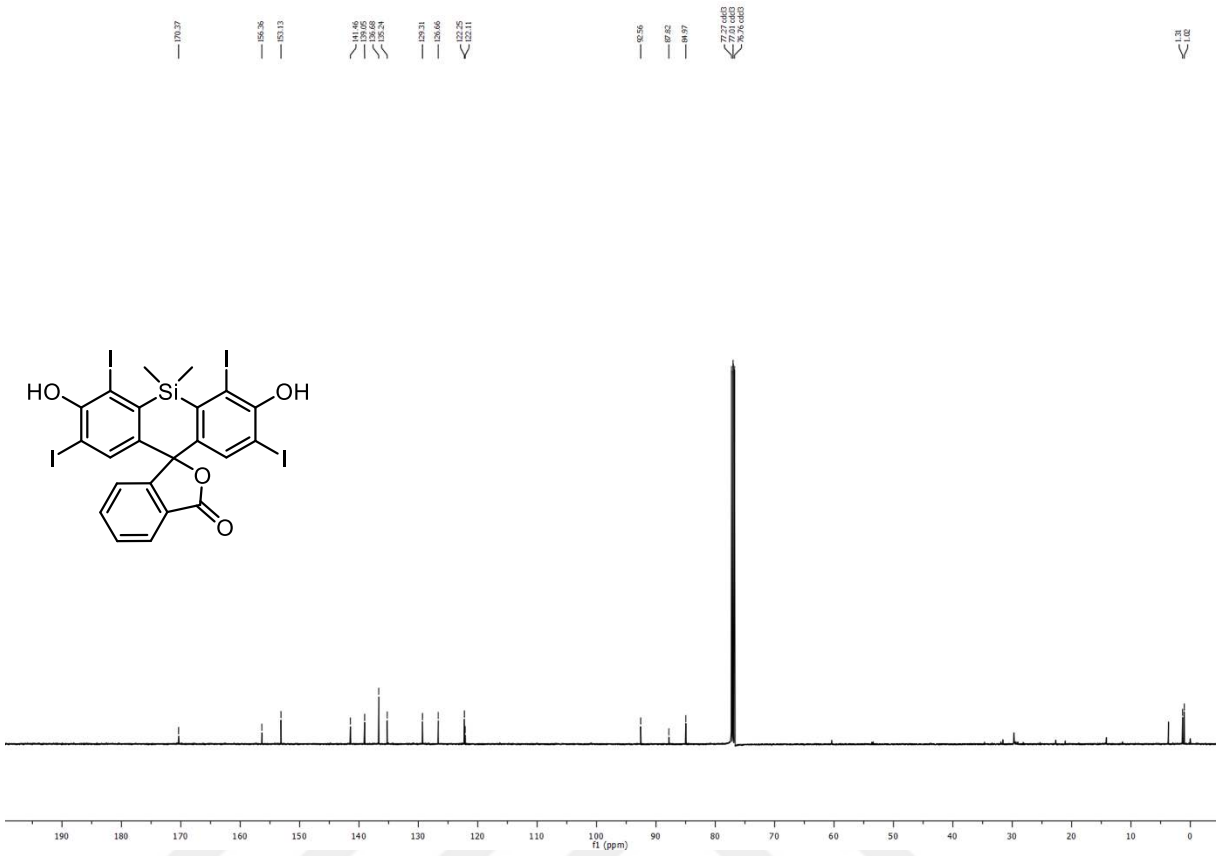
HO
Si
OH
O
O
f1 (ppm)


7.13
7.10
7.08
6.90
6.90
6.89
6.88
6.88
6.86
6.86
6.69
6.69
6.67
6.66
5.95
5.94
5.93
5.92
5.92
5.91
5.91
5.90
5.90
5.89
5.89
5.88
5.87
5.86
5.27
5.27
5.26
5.25
5.24
5.24
5.24
5.23
5.22
5.22
5.22
3.98
3.98
3.97
3.96
3.96

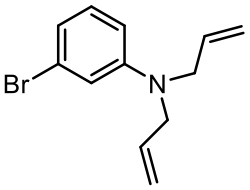
Br
N

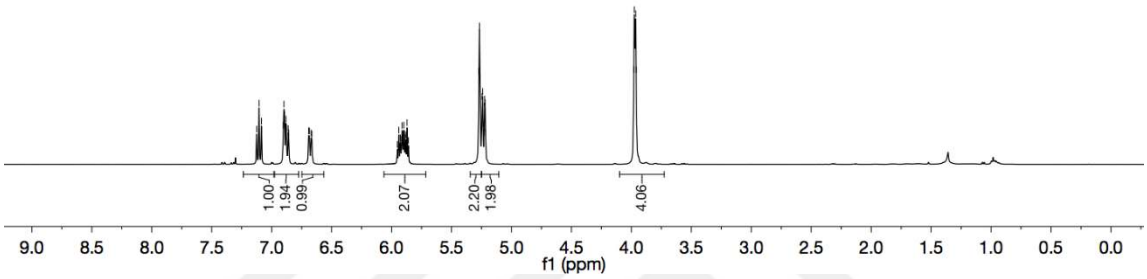
1.00
1.94
0.99
2.07
2.20
1.98
4.06
9.0
8.5
8.0
7.5
7.0
6.5
6.0
5.5
5.0
4.5
4.0
3.5
3.0
2.5
2.0
1.5
1.0
0.5
0.0
f1 (ppm)


149.90
133.23
130.34
123.42
119.12
116.37
115.04
110.92
52.77

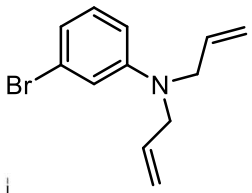
Br
N

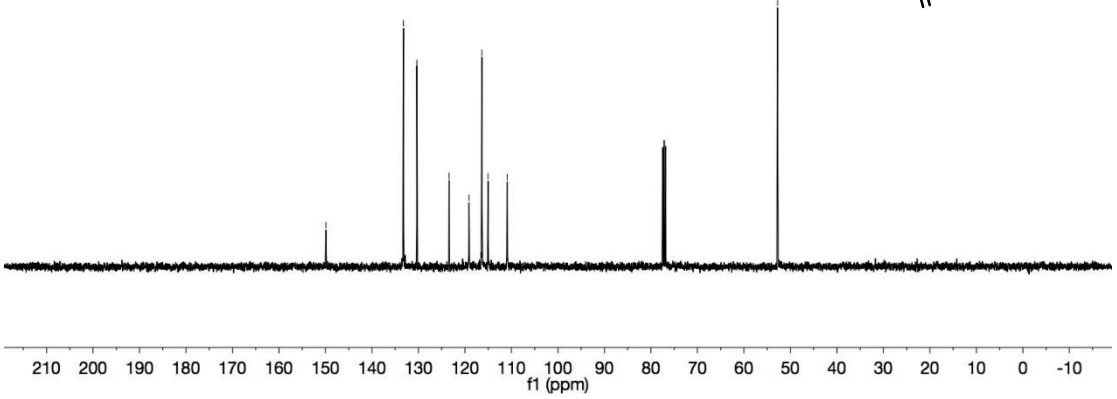
210
200
190
180
170
160
150
140
130
120
110
100
90
80
70
60
50
40
30
20
10
0
-10
f1 (ppm)


6.98
6.97
6.90
6.88
6.63
6.63
6.61
6.60
5.94
5.93
5.91
5.90
5.90
5.89
5.88
5.87
5.86
5.85
5.26
5.25
5.25
5.25
5.24
5.22
5.22
5.21
4.04
3.95
3.95
3.94
3.93
3.93

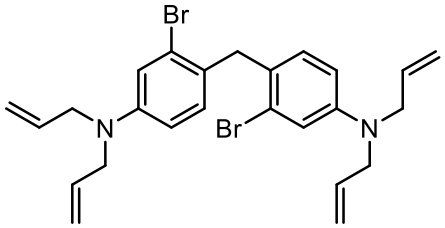
Br
Br
N
N

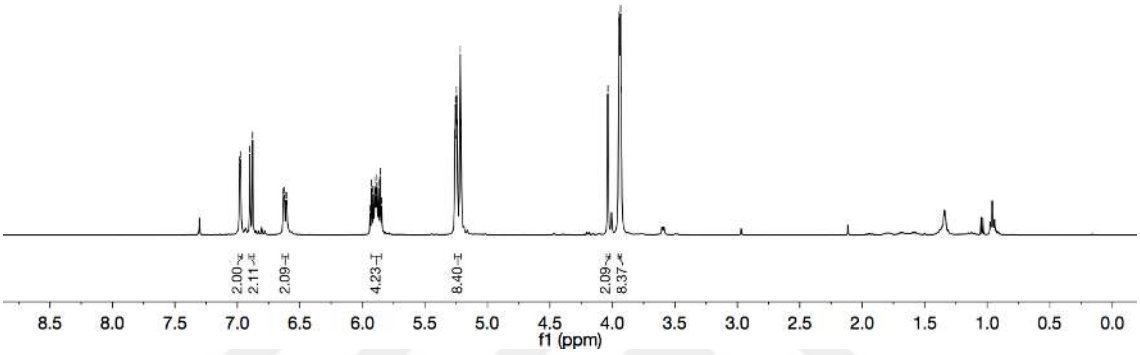
2.00
2.11
2.09
4.23
8.40
2.09
8.37
8.5 8.0 7.5 7.0 6.5 6.0 5.5 5.0 4.5 4.0 3.5 3.0 2.5 2.0 1.5 1.0 0.5 0.0
f1 (ppm)


148.17
133.53
130.85
126.96
125.61
116.35
116.03
111.72
52.82
39.83
31.66
22.73
14.23

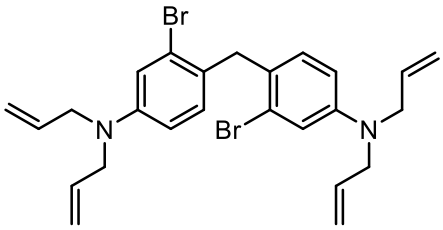
Br
Br
N
N

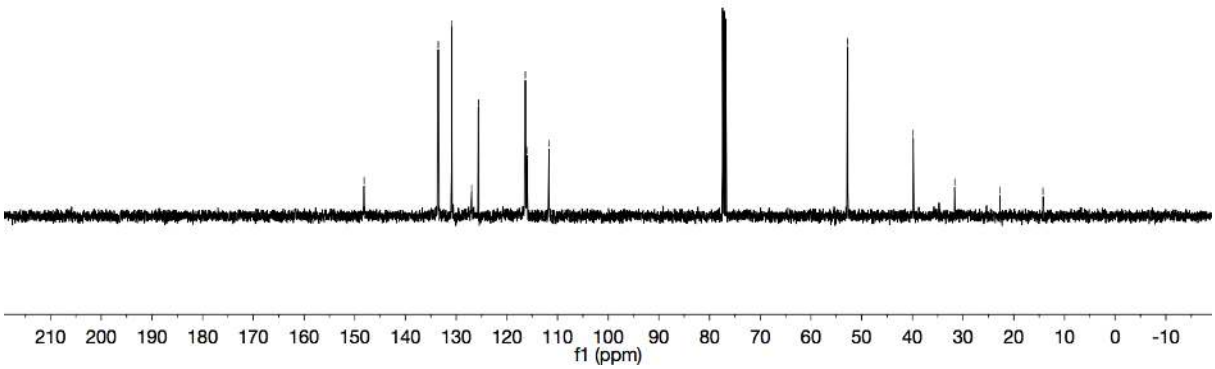
210 200 190 180 170 160 150 140 130 120 110 100 90 80 70 60 50 40 30 20 10 0 -10
f1 (ppm)

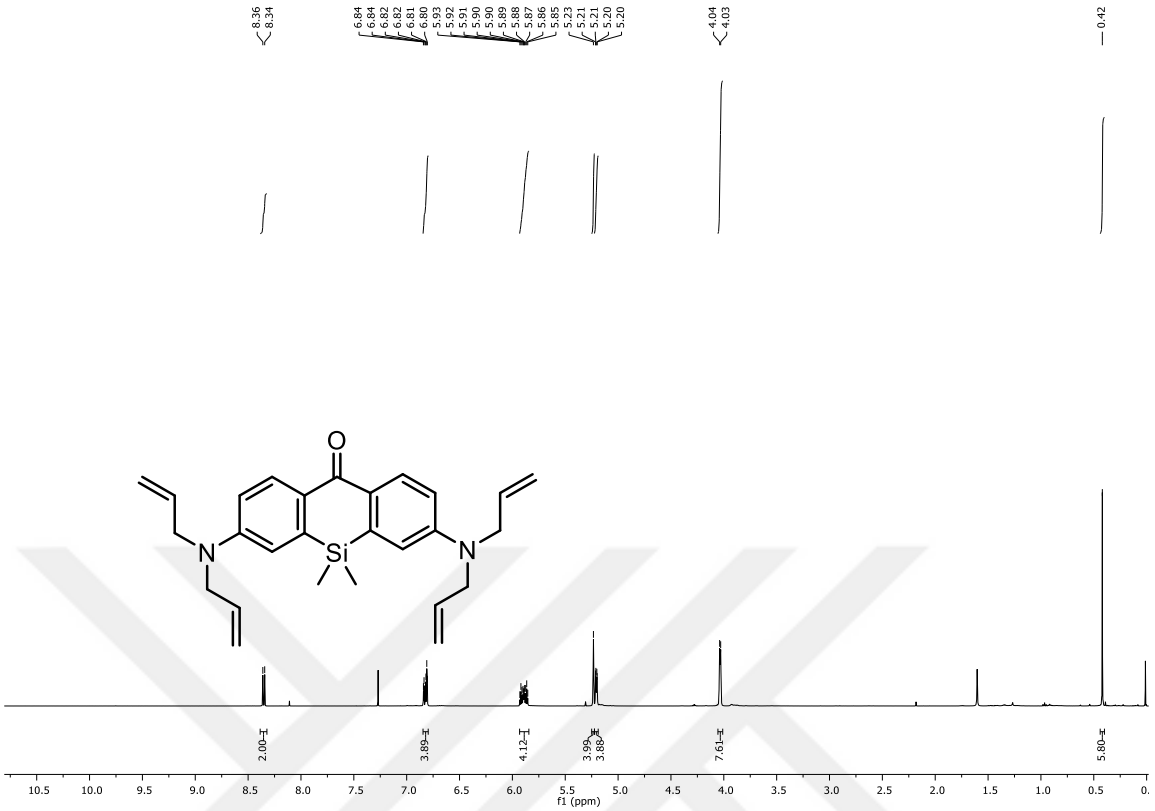
8.36
8.34
6.84
6.84
6.82
6.82
6.81
6.80
5.93
5.92
5.91
5.90
5.90
5.89
5.88
5.87
5.86
5.85
5.23
5.21
5.21
5.20
5.20
4.04
4.03
0.42
O
N
Si
N
2.00
3.89
4.12
3.99
3.80
7.61
5.80
f1 (ppm)

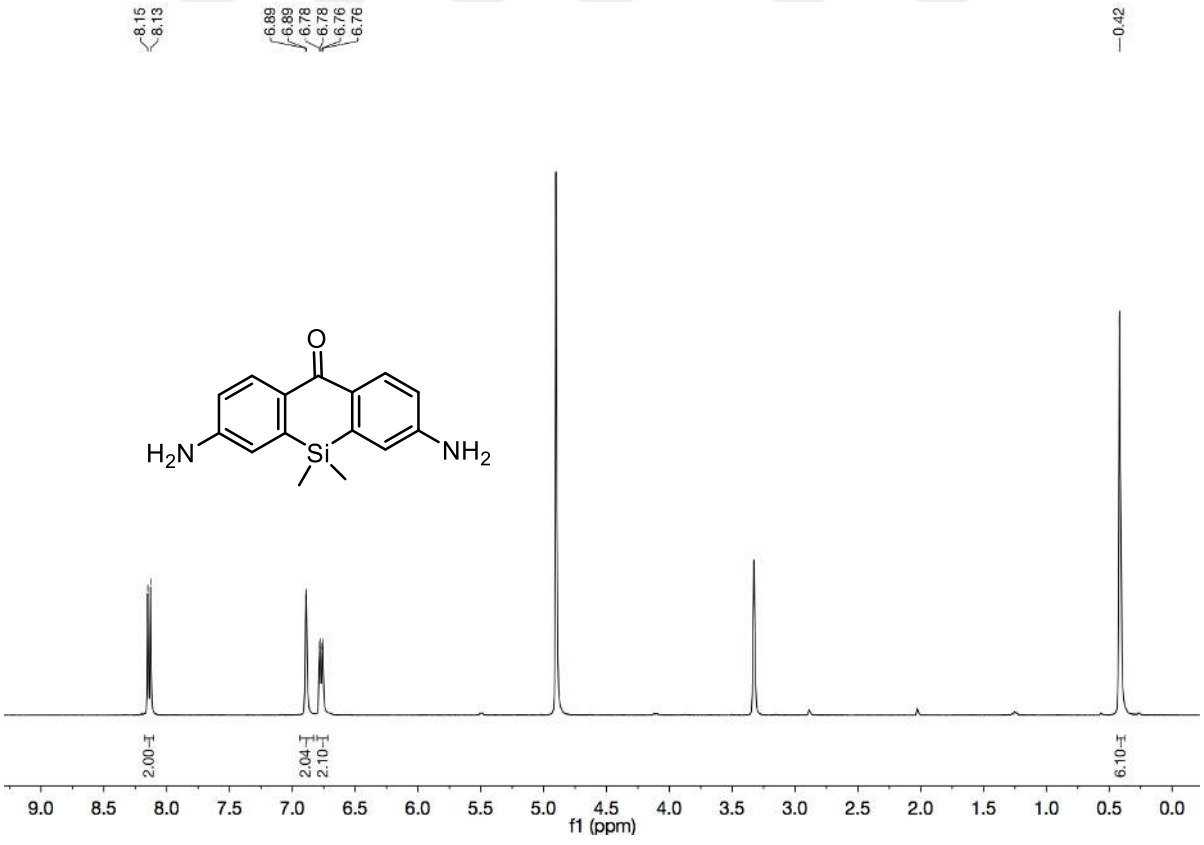
8.15
8.13
6.89
6.89
6.78
6.78
6.76
6.76
0.42
O
H2N
Si
NH2
2.00
2.04
2.10
6.10
f1 (ppm)

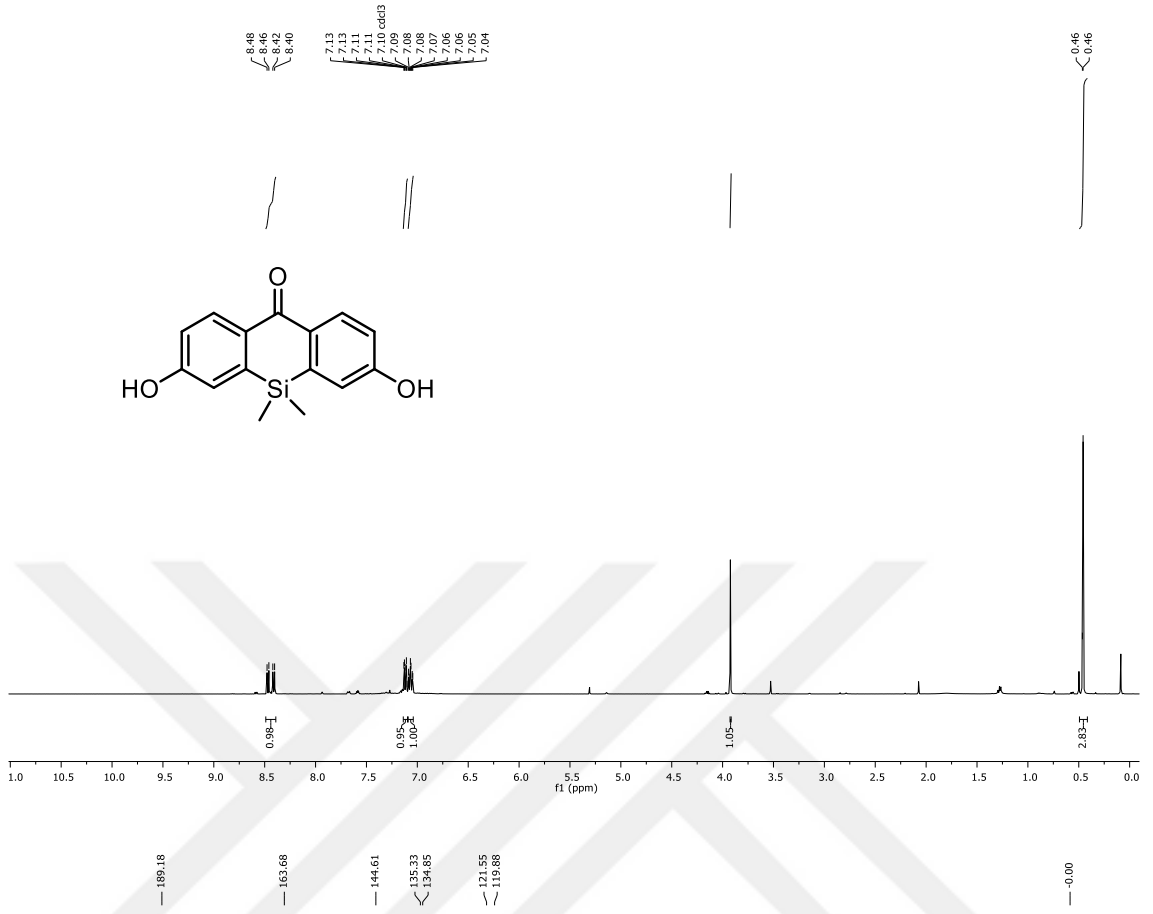
8.48
8.46
8.42
8.40
7.13
7.13
7.11
7.11
7.10 cdcl3
7.09
7.08
7.08
7.07
7.06
7.06
7.05
7.04
0.46
0.46
O
HO
Si
OH
0.98
0.95
1.00
1.05
2.83
f1 (ppm)

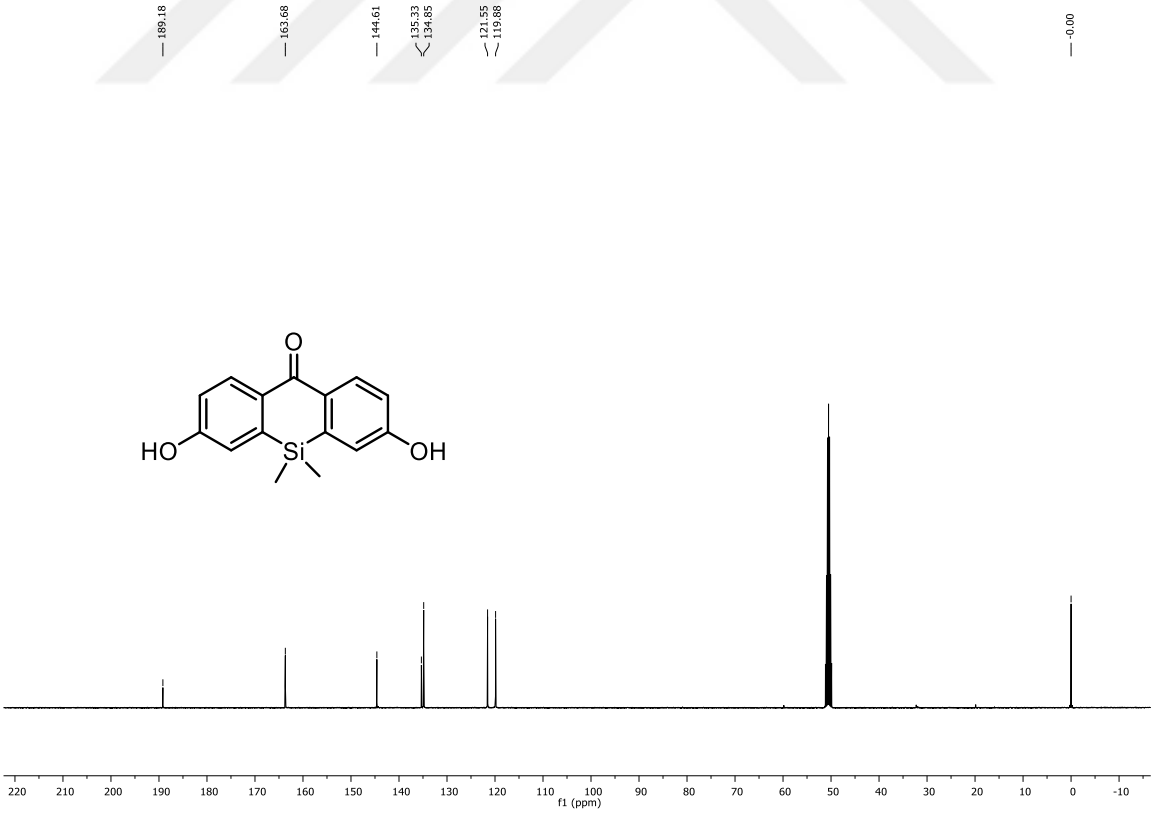
189.18
163.68
144.61
135.33
134.85
121.55
119.88
-0.00
O
HO
Si
OH
f1 (ppm)

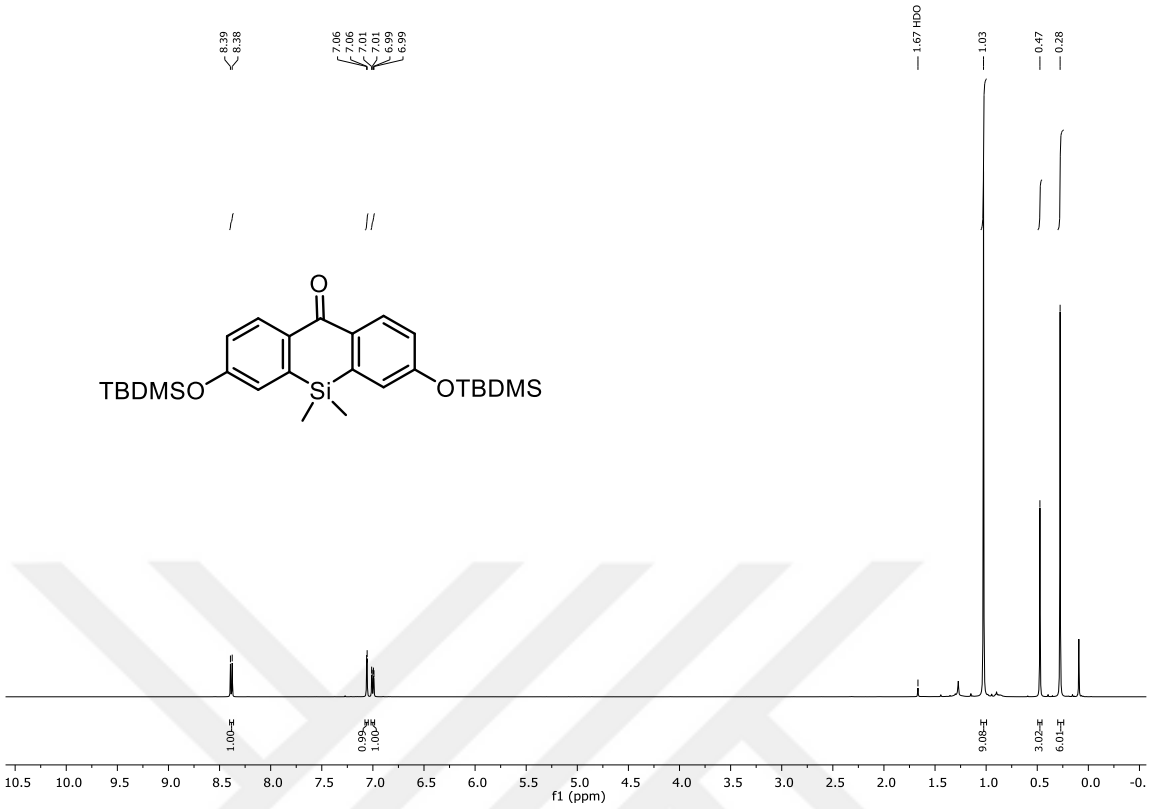
8.39
8.38
7.06
7.06
7.01
7.01
6.99
6.99
1.67 HDO
1.03
0.47
0.28
O
TBDMSO
Si
OTBDMS
1.00
0.99
1.00
9.08
3.02
6.01
f1 (ppm)


185.97
158.74
141.16
134.57
132.28
122.71
121.76
77.22
77.00
76.77
25.66
18.31
-1.54
-4.29

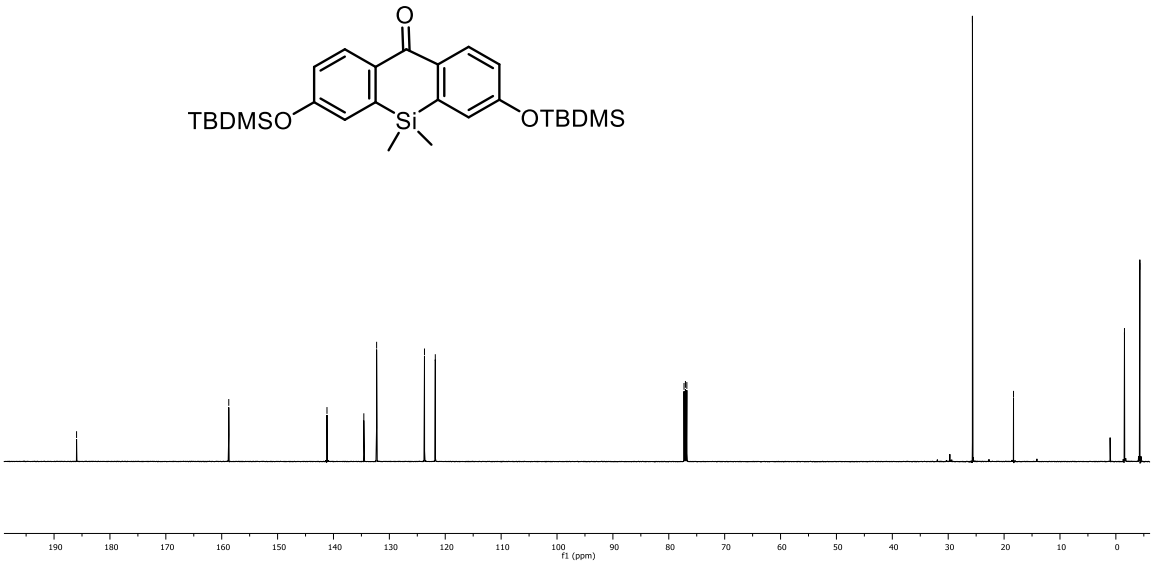
O
TBDMSO
Si
OTBDMS
f1 (ppm)

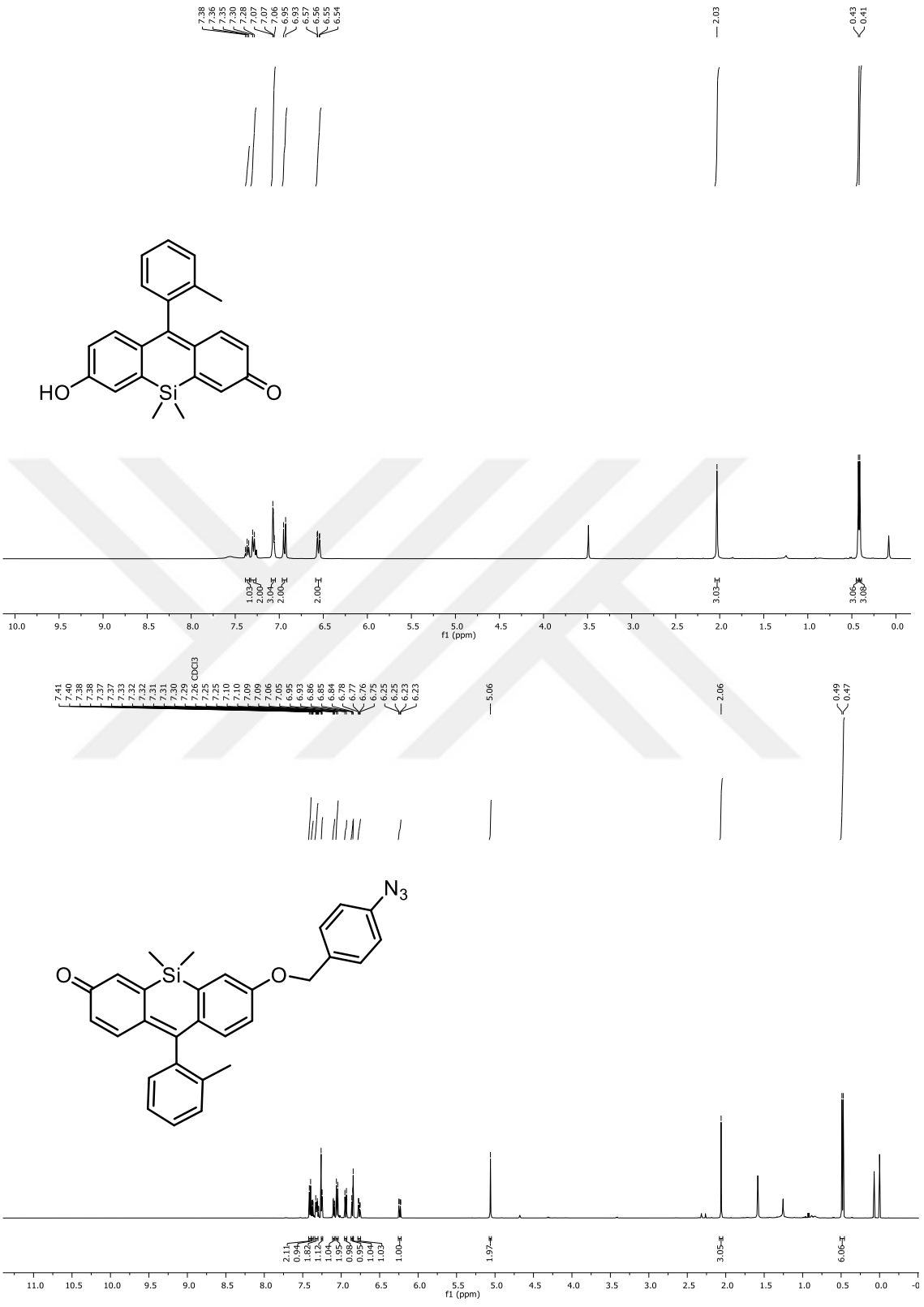
7.38
7.36
7.35
7.30
7.28
7.07
7.07
7.06
6.95
6.93
6.57
6.56
6.55
6.54
2.03
0.43
0.41
HO
Si
O
1.03
2.00
3.04
2.00
2.00
3.03
3.06
3.08
f1 (ppm)
7.41
7.40
7.38
7.38
7.37
7.37
7.33
7.32
7.32
7.31
7.31
7.30
7.30
7.26 CDCl3
7.25
7.25
7.10
7.10
7.09
7.09
7.06
7.05
6.95
6.93
6.86
6.85
6.84
6.78
6.77
6.76
6.75
6.25
6.25
6.23
6.23
5.06
2.06
0.49
0.47
N3
O
Si
O
2.11
0.94
1.82
1.12
1.04
1.95
0.98
0.95
1.04
1.03
1.00
1.97
3.05
6.06
f1 (ppm)

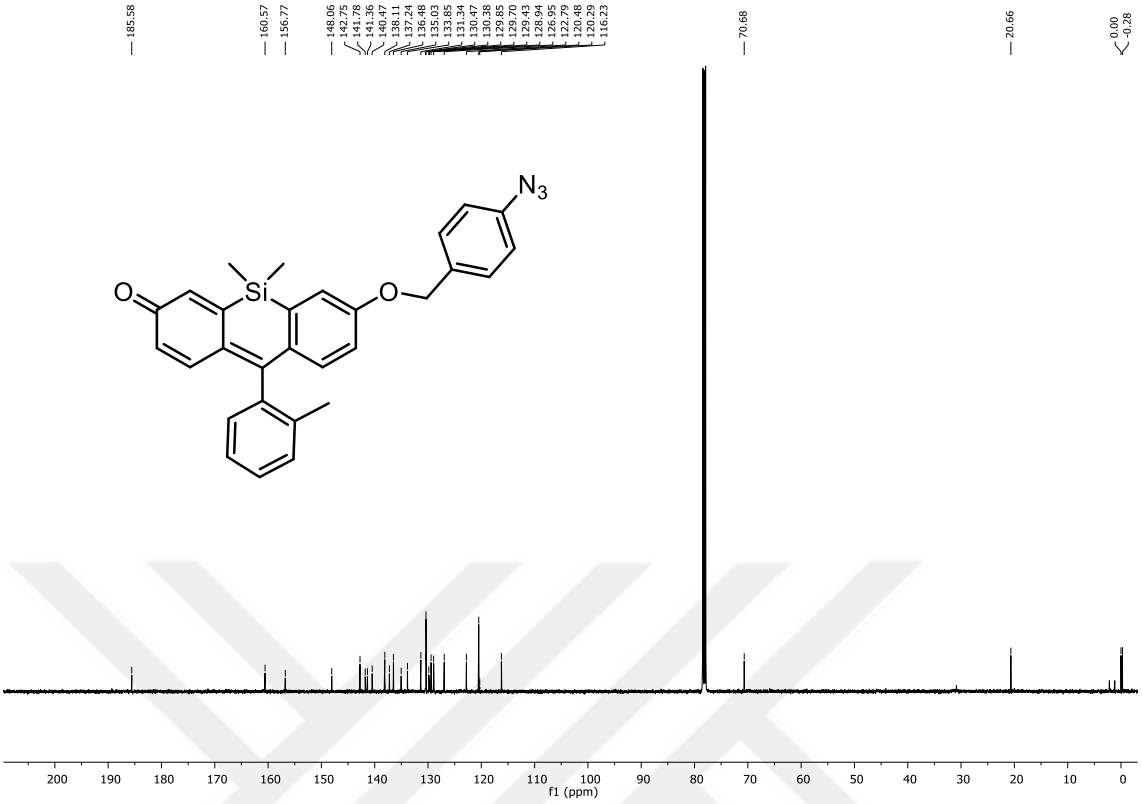
185.58
160.57
156.77
148.06
142.75
141.78
141.36
140.47
137.24
136.48
135.03
133.85
131.34
130.47
130.38
129.85
129.70
129.43
128.94
126.95
122.79
120.48
120.29
116.23
70.68
20.66
0.00
-0.28
N3
O
Si
O
f1 (ppm)


7.35
7.35
7.34
7.33
7.32
7.31
7.30
7.30
7.26 CDCl3
7.25
7.24
7.23
7.23
7.22
7.22
7.19
7.18
7.17
7.02
7.01
7.00
6.99
6.99
6.98
6.98
6.95
6.93
6.74
6.72
6.69
6.69
6.67
6.67
6.30
6.28
5.00
1.98
1.97
0.73
0.72
I
N3
O
Si
O
2.12
0.90
2.01
1.01
0.90
2.18
1.10
0.99
1.00
0.98
2.01
3.16
6.05
f1 (ppm)

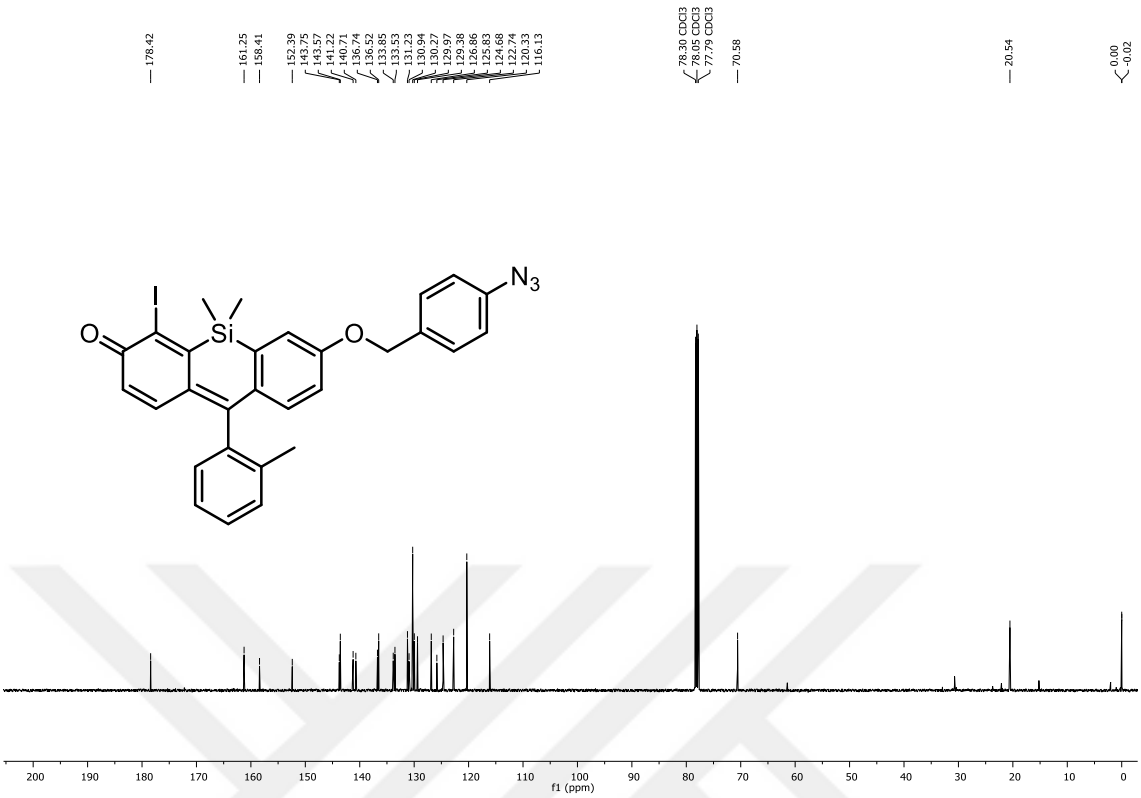

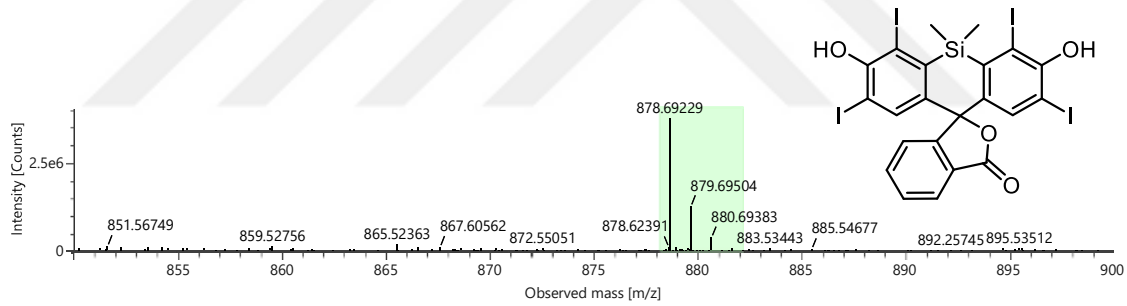

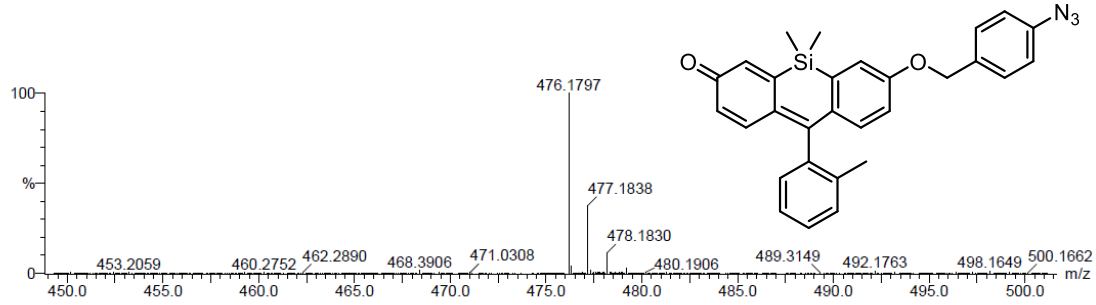

Minimum:				-5.5			
Maximum:		1000.0	1000.0	1000.0			
Mass	Calc. Mass	mDa	PPM	DBE	i-FIT	i-FIT (Norm)	Formula
476.1797	476.1794	0.3	0.6	19.5	644.8	0.0	C29 H26 N3 O2 Si

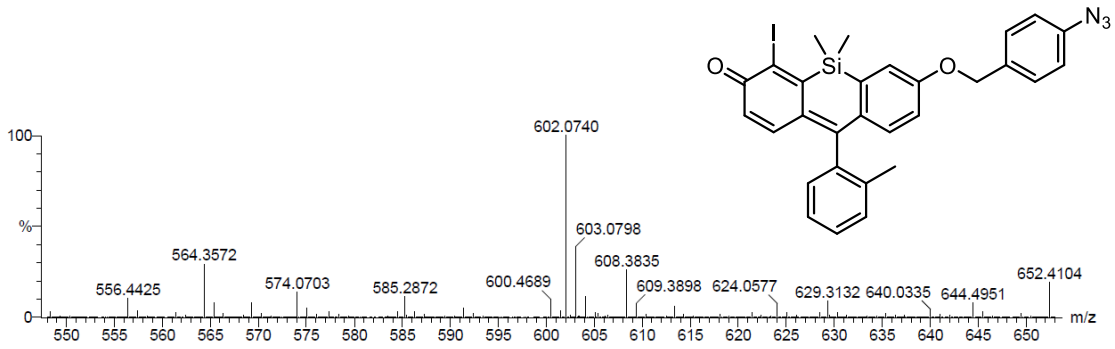

Minimum:				-5.5			
Maximum:		1000.0	1000.0	1000.0			
Mass	Calc. Mass	mDa	PPM	DBE	i-FIT	i-FIT (Norm)	Formula
602.0740	602.0761	-2.1	-3.5	19.5	319.5	0.0	C29 H25 N3 O2 Si I